

University of Dundee

DOCTOR OF PHILOSOPHY

Shear Wave Elastography Based on Optical Coherence Tomography

Song, Shaozhen

Award date:
2014

[Link to publication](#)

General rights

Copyright and moral rights for the publications made accessible in the public portal are retained by the authors and/or other copyright owners and it is a condition of accessing publications that users recognise and abide by the legal requirements associated with these rights.

- Users may download and print one copy of any publication from the public portal for the purpose of private study or research.
- You may not further distribute the material or use it for any profit-making activity or commercial gain
- You may freely distribute the URL identifying the publication in the public portal

Take down policy

If you believe that this document breaches copyright please contact us providing details, and we will remove access to the work immediately and investigate your claim.



Shear Wave Elastography Based On Optical Coherence Tomography

Shaozhen Song

A dissertation

submitted in partial fulfillment of the
requirements for the degree of

Doctor of Philosophy

2014

UNIVERSITY *of* DUNDEE
School of Engineering, Physics and Mathematics
College of Art, Science and Engineering

ABSTRACT

Mechanical properties of biological tissue are involved in a wide range of modern advances of medical science and technology. The mechanical property of biological tissue is directly related to the functionalities of tissue or organ, hence the in-depth knowledge of tissue mechanical property could lead to many benefits in medical research and health care. In clinical practice, accurate estimation of tissue mechanical property may facilitate to predict any possible pathological alterations, or to propose artificial intervention approaches.

With the purpose of a quantitative, directly visualized estimation of biological tissue mechanical property, numerous research works in elastography have been conducted and had been successfully applied to countless clinical applications. Elastography techniques had been always rooted in medical imaging technique, classified into a range of scales, based on their imaging depth and resolution performance. In the scale of tissue micro structure, elastography is still a relatively new field, enabled by the recent advances in high-resolution medical imaging techniques e.g. high-frequency ultrasound imaging and Optical Coherence Tomography (OCT). The quantitative elastography technique based on OCT, known as quantitative optical coherence elastography (OCE) is a new research field, promising high-resolution quantitative elastography information with minimal contact that is not achievable by other imaging

modalities.

The aim of the thesis is to develop a multiple-functional OCT system to image the microstructure of biological tissue, meanwhile quantify localised mechanical property in the region of interest, and further apply it for pre-clinical research applications. Starting from the numerical model of mechanical waves, the behaviours of shear waves and surface waves in biological tissue is studied. Contact mechanical stimulations, as well as non-contact ultrasound and pulsed lasers are utilised to generate transient waves in biological samples. High speed shear wave imaging technique is developed and optimized based on a Phase-sensitive OCT (PhS-OCT) system to capture the transient wave propagation in samples, and the inversion algorithm for mapping localized shear modulus is proposed. The experimental results indicated that the Shear Wave Imaging OCT (SWI-OCT) technique is capable to provide abundant temporal and spatial resolution to capture the shear waves in tissue-mimicking phantoms and in vivo biological samples. Quantitative elastography results were obtained from mouse skin and cornea samples, suggesting potential diagnostic and therapeutic clinical applications.

DECLARATION

I hereby declare that this thesis is my own work and effort and that it has not been submitted anywhere for any award. Where other sources of information have been used, they have been acknowledged.

Shaozhen Song

CERTIFICATE

This is to certify that Shaozhen Song has done this research under my supervision and that he has fulfilled the conditions of Ordinance 39 of the University of Dundee, so that he is qualified to submit for the Degree of Doctor of Philosophy.

Zhihong Huang

COPYRIGHT

Attention is drawn to the fact that copyright of this thesis rests with its author. This copy of the thesis has been supplied on the condition that anyone who consults it is understood to recognize that its copyright rests with the author and that no quotation from this thesis and no information derived from it may be published, without prior writhe consent of the author.

This thesis may not be consulted, photocopies or lent by any library without permission of the author for a period of three years from the date of acceptance of the thesis.

ACKNOWLEDGEMENTS

"Honoured, deeply, to have your company."

I would like to express my sincere gratitude to all the people that supported, inspired, and corrected this work. The greatness of science once made me feel tiny, but I am deeply honoured to have everyone who raise me up to help me realize there is no mountain too high.

Dr. Zhihong Huang, my supervisor, gave me the first lift to the opportunity to involve in this fantastic project, who continuously guided and supported both my work and my life abroad, training me from a vacant boy to a complete researcher. Professor Ruikang K. Wang, my supervisor in University of Washington, has always been an indispensable guide, with his always high, unifying and open point of view in scientific research. Both of my supervisors are like a loving mother and a sterning father, who lighted up my path into research. Professor Matthew O'Donnell has also been a great adviser, with impressive wisdom in a great range of field.

Special thanks goes to Dr. Zhongwei Zhi, who has been a necessary source of corrections, suggestions and ideas. All my workmates in University of Washington, Dr. Peng Li, Dr. Lin An, Miss Jia Qin, Dr. Lei Shi, Dr. Gongpu Lan, Dr. Roberto Reif, Dr. Yin Xin and Dr. Suzan Dziennis had been of great help in many ways of carrying out this study. My senior teammates Dr. Chunhui Li, Mr. Guangying Guan and Mr. Sinan Li introduced me to the subject of this dissertation, with their inspiring approach to the problems. I also thank Dr. Xu Xiao, Dr. Jing Gao, Dr. Yang Kuang, Mr. Han

Wang, Dr. Yongqiang Qiu, Dr. Zhen Qiu, Mr. Cheng Wei, Mr. Xiaowei Zhou, Mr. Lin Gui, Miss Yunwei Xu and Mr Xiaochun Liao, who have long been great group members and splendid friends in Dundee, for all their help and company. Many thanks to Mr. Nhan Minh Le for his wisdom and warm friendship.

Dr. Thu-mai Nguyen and Dr. Bastien Arnal gave me the chance to work with them and shared their experience in different fields, many breakouts of my work are made possible by this enthusiastic and professional couple.

It's also an honour for me to express my gratitude to the Chinese Scholarship Council for the financial support.

Last and most, my deepest thanks goes to my parents for bringing me to this world and their endless love and care. To my wife, Chen, for her incomparable love.

TABLE OF CONTENTS

ABSTRACT	I
DECLARATION.....	III
CERTIFICATE	IV
COPYRIGHT.....	V
ACKNOWLEDGEMENTS	VI
TABLE OF CONTENTS.....	VIII
LIST OF FIGURES	XII
LIST OF TABLES	XVI
GLOSSARY OF TERMS	XVII
 1. INTRODUCTION	 1
1.1. Objectives.....	2
1.2. Thesis Outline	4
1.3. Publication Arising from this Work.....	6
Conference oral presentations	7
 2. TECHNICAL BACKGROUND	 9
2.1. Introduction.....	9
2.2. Tissue Biomechanics	10
2.3. Measurements of tissue biomechanics	12
2.3.1. <i>Biomechanics of skin</i>	12
2.3.2. <i>Biomechanics of cornea</i>	16
In vitro cornea biomechanics measurements.....	17

<i>In vivo</i> methods	18
Corneal elasticity mapping	18
2.4. Elastography	19
2.4.1. <i>Physics of elastography</i>	19
2.4.2. <i>Elastography with medical imaging devices</i>	21
Ultrasound elastography	21
Magnetic Resonance Elastography	23
2.5. Optical coherence tomography	24
2.5.1. <i>Development and theory of OCT</i>	24
2.5.1. <i>Performance parameters of OCT</i>	27
2.5.2. <i>Phase sensitive OCT</i>	29
2.6. Optical coherence elastography	31
2.6.1. <i>Static and quasi-static optical coherence elastography</i>	31
2.6.2. <i>Dynamic optical coherence elastography</i>	32
Compression OCE	33
SAW-OCE	34
Magnetomotive OCE	35
2.7. Conclusions	36
 3. TRANSIENT MECHANICAL WAVES THEORY AND MODELLING.....	 38
3.1. Introduction.....	38
3.2. Propagation of mechanical waves.....	40
3.3. Characterization of transient mechanical waves in biological tissue...	45
3.3.1. <i>Longitudinal wave</i>	45
3.3.2. <i>Shear wave</i>	47
3.3.3. <i>Surface acoustic wave (SAW)</i>	48
3.3.4. <i>Lamb wave</i>	49
3.4. Simulation of transient waves in soft tissue	51
3.4.1. <i>Finite element simulation</i>	51
Problem definition.....	52
Solution.....	52
Post-processing and visualization.....	53
3.4.2. <i>Simulation of mechanically induced waves</i>	53
Model definition.....	53
Results.....	55
3.4.3. <i>Simulation of pulsed laser induced transient waves</i>	58
Model definition.....	58
Results.....	61
3.5. Conclusions	64

4.	SHEAR WAVE IMAGING TECHNIQUE USING PHS-OCT	65
4.1.	Introduction.....	65
4.2.	Phase sensitive OCT.....	67
4.2.1.	<i>System specifications of Spectral Domain OCT system</i>	<i>67</i>
4.2.2.	<i>Hardware design of an SD-OCT system</i>	<i>68</i>
	Laser source.....	69
	Interferometer	70
	Reference arm	71
	Sample arm.....	71
	High-speed spectrometer	73
	Processor.....	74
4.2.3.	<i>Data acquisition in SD-OCT system.....</i>	<i>75</i>
4.2.4.	<i>OCT data processing.....</i>	<i>78</i>
	Dispersion compensation.....	78
	OCT imaging and phase detection.....	81
4.3.	Shear wave imaging technique.....	84
4.3.1.	<i>Shear wave imaging hardware set up</i>	<i>84</i>
4.3.2.	<i>Data acquisition</i>	<i>86</i>
4.4.	Shear wave imaging data processing	89
4.4.1.	<i>Phase unwrapping on wave field data.....</i>	<i>89</i>
4.4.2.	<i>Surface ripple artefact removal</i>	<i>92</i>
	Theoretical analysis of surface ripple artefact	92
	Experimental evidence of artefact	95
	Validation of compensation algorithm	98
	Discussion.....	101
4.4.3.	<i>Pulse compression</i>	<i>102</i>
	Pulse compression algorithm.....	104
4.4.4.	<i>Directional filter.....</i>	<i>105</i>
4.5.	Conclusions	107
5.	SHEAR WAVE OCE AND APPLICATIONS	108
5.1.	Introduction.....	108
5.2.	Elastogram reconstruction	109
5.2.1.	<i>Time-of-flight method</i>	<i>109</i>
5.2.2.	<i>Wave inversion method.....</i>	<i>111</i>
5.3.	Elastography experiment on tissue-mimicking phantoms.....	114
5.3.1.	<i>Mechanically induced shear wave OCE.....</i>	<i>114</i>
	Experimental arrangements.....	114
	Phantom preparations	116
	Results.....	116
	Discussion.....	122

5.3.2.	<i>Ultrasonically induced shear wave OCE</i>	123
	Experimental arrangement.....	123
	Results.....	124
	Discussion.....	127
5.3.3.	<i>Pulse compression optimized SW-OCE</i>	128
	Pulse compression of mechanically induced shear wave	128
	Pulse compression of ultrasonically induced shear wave.....	134
	Discussions.....	140
5.3.4.	<i>Pulsed laser induced shear wave OCE</i>	142
	Wave generation with diode laser.....	142
	High energy pulsed laser	144
	Results and discussions	145
5.4.	Elastography experiments on animal model	147
5.4.1.	<i>OCE experiments on Thiel mouse skin</i>	147
	Experimental arrangements.....	147
	Results.....	147
	Discussions.....	150
5.4.2.	<i>Shear wave OCE on cornea</i>	151
	Experimental setup	151
	Results.....	152
	Discussion and conclusions	155
5.5.	Conclusions	157
6.	CONCLUSIONS AND FUTURE WORK	158
6.1.	Conclusions	159
6.1.1.	<i>Transient mechanical waves in biological tissue</i>	159
6.1.2.	<i>Shear wave imaging technique</i>	160
6.1.3.	<i>SW-OCE towards clinical application</i>	160
6.2.	Recommendations for future work	161
	OCT shear wave imaging.....	161
	Shear modulus inversion.....	162
	REFERENCES	165

LIST OF FIGURES

Figure 2-1 A comparison of stress-strain curve for steel and various biological tissue.....	11
Figure 2-2 Comparison of various medical imaging modalities in terms of resolution and penetration depth	21
Figure 2-3 A basic setup of time-domain OCT system	25
Figure 2-4 Illustration of simulated interferometry signal and image in a low-coherence imaging system.....	26
Figure 2-5 Typical SD-OCT(a) and SS-OCT(b) system setup	27
Figure 2-6 An illustration of loading schemes and elasticity estimation for three OCE techniques: Compression, SAW and magnetomotive[78]	33
Figure 2-7 OCT image of a human forearm skin with a hard nodule and the corresponding SAW-OCE elastogram[104]	35
Figure 3-1 Particle motion patterns of different mechanical waves (a) longitudinal wave (b) shear wave (c) surface wave (d) fundamental modes of Lamb wave	42
Figure 3-2 Numerical simulation results of pulse-stimulated mechanical waves.	46
Figure 3-3 Typical longitudinal waveform and corresponded frequency spectrum of steel (a,b) and tissue mimicking agar phantom (c,d)	47
Figure 3-4 Typical surface waveform and corresponded frequency spectrum of steel (a,b) and tissue mimicking agar phantom (c,d)	49
Figure 3-5 Model geometries and mesh for contact generation of transient waves.....	54
Figure 3-6 Shaker head displacement profile in simulation model	54
Figure 3-7 Simulation results of contact induced shear waves	56
Figure 3-8 Simulated wave snapshots on a phantom with embedded inclusion	58
Figure 3-9 Simulation setup of pulsed laser generated mechanical waves on single layer and two layer medal model	60

Figure 3-10 Simulation setup of pulsed laser generated mechanical waves on an agar phantom with embedded inclusion	61
Figure 3-11 Surface wave results from single layer and two layer FEA models.....	62
Figure 3-12 Phase velocity result of surface waves simulated in single layer and two layer FEA models.	62
Figure 3-13 Surface acoustic wave traces on the surface of agar phantom with embedded inclusion	63
Figure 4-1 Schematic drawing of the SD-OCT system	69
Figure 4-2 Emission spectrum of two separate SLDs in OCT laser source	69
Figure 4-3 Emission spectrum of combined SLD output in OCT laser source.....	70
Figure 4-4 Reference arm assembly	71
Figure 4-5 A ZEMAX model of spectrometer for SD-OCT system.....	74
Figure 4-6 OCT data acquisition program flowchart.....	76
Figure 4-7 Trigger file example for an 3-D OCT scanning	78
Figure 4-8 SD-OCT dispersion compensation procedure flowchart. Dashed path shows the dispersion compensation	79
Figure 4-9 Raw spectrum from camera and the dispersion compensation, (a1,a2) un-compensated spectrum of the interferogram produced by two reflectors (b1,b2) compensated	80
Figure 4-10 OCT intensity signal from compensated spectrum	81
Figure 4-11 hardware set up of shear wave imaging technique with a contact mechanical stimulation	85
Figure 4-12 Synchronization setup schematic of ARFI-SWI (a) and pulse laser SWI (b)	86
Figure 4-13 Timing schematic of shear wave imaging scanning protocol	87
Figure 4-14 Illustration of shear wave imaging scanning protocol	88
Figure 4-15 Comparison of phase unwrapping methods	90
Figure 4-16 Illustration of a situation when OCT phase is influenced by both sample surface motion and scatterer motion	93
Figure 4-17 Illustration of phantom configuration in surface ripple artefact experiment.....	96
Figure 4-18 Shear wave imaging results for demonstrating the presence of surface ripple artefactes	96
Figure 4-19 Displacement waveforms at three depths of the layered phantom	98
Figure 4-20 A snapshot of displacement field from the numerical simulation of shear waves in homogenous phantom. (a) A snapshot of displacement field from the numerical simulation, and (b) measured displacement field by PhS-OCT. The images are displayed at the same scale and time point.	99
Figure 4-21 (a1-a4) Wave propagating pattern detected with PhS-OCT in a homogenous tissue phantom; (b1-b4) wave pattern after phase compensation; and (c1-c4) wave pattern in homogeneous phantom with a layer of oil above.	101
Figure 4-22 Chirp compression of a simulated signal	103

Figure 4-23 An example of a compressed pulse on a 0.5%-agar phantom.....	105
Figure 4-24 Directional filter process on one slice of SWI data	106
Figure 4-25 Directional filter processing workflow.	106
Figure 5-1 Shear wave speed estimation with time-of-flight cross correlation	110
Figure 5-2 Flowchart of the speed estimation algorithm for a single pixel in 2-D shear wave velocity mapping.	111
Figure 5-3 Schematic of system for SWI-OCT for mechanically induced shear waves.....	115
Figure 5-4 Displacement field overlaid onto structural image of a homogenous phantom	117
Figure 5-5 (a-d) Wave propagation pattern in agar phantoms with agar concentration: (a) 0.5%, (b) 0.75, (c) 1% and (d) 2%, respectively. (e) Wave traces along the specified wave propagation path shown in Figure 5-4 as 'Px'. (f) Linear fitting of the phase delays vs. position offsets from the first point.	118
Figure 5-6 Shear modulus map of a 0.5% agar phantom reconstructed using SW-OCE.....	119
Figure 5-7 Measurement results of shear wave velocity in agar phantom.....	119
Figure 5-8 B-mode structural image of agar phantom with inclusion	120
Figure 5-9 Displacement field snapshots at a evenly sampled time points.....	121
Figure 5-10 (a) Linear fitting of phase delays vs. position offsets for two selected wave propagation paths. (b) Quantitative map of shear modulus (μ) computed from dynamic shear wave visualization	122
Figure 5-11 Experimental setup for shear wave elastography combining a PhS-OCT system with US radiation force	124
Figure 5-12 Shear wave imaging results of ultrasonically induced shear waves.....	125
Figure 5-13 Shear wave speed estimation and elastogram reconstruction on SWI result	126
Figure 5-14 Results obtained on a bi-layered phantom in ARF-SW-OCE.....	126
Figure 5-15 Displacement field in a 1% agar phantom resulting from a chirp excitation.	129
Figure 5-16 Displacement field in a 1%-agar phantom after compression	130
Figure 5-17 (a) Spatio-temporal representation of the normalized axial displacement field at a given depth of a 0.5%-agar phantom. The x-axis represents the time whereas the y-axis represents the lateral position. (b) Reconstructed shear modulus map (color scale) superimposed on the B-mode image (gray scale).	131
Figure 5-18 B-mode image of a heterogeneous phantom made from a 1%-agar background and 2%-agar inclusion. The white dash line delineates the inclusion.	132
Figure 5-19 Results using a 3 kHz, 8-ms long, excitation on a 0.5%-agar phantom containing a 1%-agar inclusion.	132
Figure 5-20 Heterogeneous phantom consisting of a 1%-agar background and a 2%-agar inclusion.	134
Figure 5-21 Axial displacements in a 10% gelatin phantom	135
Figure 5-22 Snapshots of shear wave propagation induced in a 10%-gelatin phantom using a coded excitation at an US peak pressure of 3 MPa.	136
Figure 5-23 Temporal profile (top row) and spectrum (bottom row) of the displacements obtained	

in a gelatin phantom for an US peak pressure of 3 MPa	137
Figure 5-24 Temporal profile (top row) and spectrum (bottom row) of the displacements obtained in a gelatin phantom for an US peak pressure of 1.5 MPa	138
Figure 5-25 Reconstruction of stiffness maps in a heterogeneous phantom.....	139
Figure 5-26 Box plot of the shear wave speed values in respectively the left part (left) and right part (right) of the phantom.....	140
Figure 5-27 Optical path for confocal diode laser excitation	143
Figure 5-28 Shear wave imaging results with diode laser induced shear waves	143
Figure 5-29 (a) spatial-temporal wave plot on selected wave path and (b) phase delay fitting for calculating wave velocity	144
Figure 5-30 Epi-illumination setup for pulsed laser generation of shear waves.....	145
Figure 5-31 High energy pulsed laser induced shear waves captured by SWI-OCT in a skin-mimicking phantom.....	146
Figure 5-32 Typical shear wave imaging results on Thiel mouse cadaver	148
Figure 5-33 SW-OCE results on Thiel mouse skin, shear modulus map overlapped on structural image	149
Figure 5-34 Averaged shear modulus results from 5 Thiel mouse cadaver, F1-F3 and M1-M3 are the female and male mouse, respectively	149
Figure 5-35 SW-OCE results on fresh mouse skin, shear modulus map overlapped on structural image. (a1,a2) female mouse (a3,a4) male mouse.....	150
Figure 5-36 Averaged shear modulus from repeated measurements on fresh mouse cadaver	150
Figure 5-37 Experimental setup for shear wave OCE on mouse cornea	151
Figure 5-38 Snapshots of shear wave propagation in an in vivo mouse cornea sampled at different time points. Axial displacement amplitude is colour coded: red indicates the motion away from the OCT imaging probe.....	153
Figure 5-39 Shear wave speed map on mice cornea (a) knock-out mouse (b) wild-type, colour scale represents the shear wave speed and is superimposed on B-mode OCT image.	153
Figure 5-40 Quantitative comparison of the shear wave speed between a group of knock-out (N=4) and a group of wild-type (N=3) mice.	154
Figure 5-41 Results of frequency-modulated excitation on an excised human cornea (31 years old female donor). Temporal profile (top row) and spectrum (bottom row) of the displacements at one location respectively before (a) and after (b) pulse compression.	155
Figure 5-42 Effect of the IOP of the corneal shear wave speed assessed on an excised human cornea (31 years old female donor).	155

LIST OF TABLES

Table 2-1 Measurement of skin mechanical properties, including skin elastography results from published literature	15
Table 3-1 Input parameters of pulsed laser induced mechanical wave model.....	60
Table 4-1 Specifications of the SD-OCT system (f – Objective lens focal length).....	68

GLOSSARY OF TERMS

CCD	Charge Coupled Device
CW	Continuous Wave
CRF	Corneal Resistance Factor
CH	Corneal Hysteresis
CWT	Continuous wavelet transform
C_L	Velocity of longitudinal wave
C_R	Velocity of Rayleigh wave
C_S	Velocity of shear wave
d	Diameter
DAC	Digital Analogue Converter
DFT	Discrete Fourier Transform
DP	Dermal papillae
E	Young's Modulus
EMD	Empirical mode decomposition
f	Frequency
F	Nuclei folds
FWHM	full width at half maximum
FD-OCT	Frequency domain optical coherence tomography
FE	Finite Element
FEM/FEA	Finite Element Model/Finite Element Analysis
FFT	Fast Fourier Transform
GUI	Graphic User Interface

I_0	Irradiation of laser pulse
ICRS	Intrastromal Corneal Ring Segments
IMAQ	(National Instruments) Imaging Acquisition System
IMF	Intrinsic mode functions
IOP	Intraocular pressures
k	Wave vectors
LCI	Low Coherence Interferometry
LASIK	Laser-Assisted in situ Keratomileusis
MM	Malignant melanoma
MRE	Magnetic resonance elastography
MRI	Magnetic Resonance Imaging
NDE	Non-Destructive Evaluation
NDT	Non-Destructive Testing
Nd:YAG	Neodymium-doped yttrium aluminium garnet
OCT	Optical Coherence Tomography
OCDR	optical coherence-domain reflectometry
OTDR	optical time-domain reflectometry
OCE	Optical coherence elastography
ORA	Ocular Response Analyzer
OPD	Optical path delay
OPL	Optical path length
P-wave	Longitudinal wave
PA	Photo acoustic
PAM	Photoacoustic imaging
PD	Papillary dermis
PhS-OCT	Phase sensitive optical coherence tomography
PRDOCT	Phase-resolved Doppler OCT
PRK	Photorefractive keratectomy
t	Time
r	Radius
s	Strain
S-wave	Shear wave
SASW	Spectral analysis of SAW
SAW	Surface Acoustic Wave
SC	Stratum Corneum
SD-OCT	Spectral Domain Optical Coherence Tomography
SLD	Superluminescent Diode

SSI	Supersonic Shear wave Imaging
SAW-OCE	Surface Acoustic Wave OCE
SW-OCE	Shear Wave OCE
SWI	Shear Wave Imaging
SNR	Signal to noise ratio
STFT	Short time discrete Fourier transform
TD-OCT	Time domain optical coherence tomography
TR	Time of repetition
US	Ultrasound
λ	Wave length
μ_a	Absorption coefficient
ν	Poisson's ratio
ρ	Density
σ	Stress
φ	Phase change

1.INTRODUCTION

Mechanical force and biological tissue mechanical properties play a significant role in many vital activities[1]. Mechanical properties are involved in all scales of biological development, organisation and function, starting from cellular level, to organ level and whole body level. Furthermore, pathological changes in the tissue micro-structure such as tumour invasion will lead to different biomechanical properties in tissue. A comprehensive and accurate estimation of tissue mechanical property could assist clinical diagnosis and even help in the planning of surgical procedures[2].

For the purpose of measuring biomechanics in different scale levels, many methods have been developed, to detect biomechanical properties as indicators of tissue status and disease. For centuries, physicians have routinely used palpation as a qualitative method to detect pathological changes. Combined with all forms of medical imaging devices, elastography techniques were developed to investigate and quantitatively measure the mechanical properties in biological tissue. Elastography technologies experienced intense developments during the last several decades, especially tomographic ones such as Computed Tomography (CT), Magnetic Resonance Imaging (MRI), and ultrasound imaging due to their abilities of generating direct visualisation of sectional or volumetric images. In recent years, dynamic elastography has gained remarkable research interest, with its benefits of quantitative nature.

However, current elastography techniques are still far from ideal. The resolution of all the aforementioned elastography techniques is still insufficient to provide elasticity mapping images of tissue micro-structure level. In many diagnostic applications such as scleroderma and keratoconus, a quantitative mapping of tissue elasticity with high spatial resolution would be capable of providing lateral comparison, for a more subjective diagnosis. It is crucial to develop an imaging technique that can provide high-resolution quantitative elastography information with minimal contact.

For measurement of biomechanical properties at tissue and cellular levels, optical coherence tomography (OCT) and microscopic based elastography techniques are most promising because of their micron to nanometer imaging resolution, and up to millimeter-scale penetration depth, among all the biomedical imaging modalities. While OCT has many successful applications in structural imaging in ophthalmology, cardiology and dermatology etc., the report of using OCT as an elastography tool, especially as quantitative elastography technique, is very limited. The major difficulty of using OCT for dynamic elastography is that the imaging speed is not sufficient to track the transient mechanical response inside specimen. Microscopic based elastography is analogue to traditional mechanical test approach, which is not discussed in this study.

The goal of this thesis is to overcome the performance limitations, to establish dynamic elastography techniques based on optical coherence tomography, and to investigate their applications on measuring biomechanical properties at micro tissue structure level.

1.1. Objectives

The overall aim of this research is to design and develop a pre-clinical prototype Optical Coherence Elastography (OCE) device, based on PhS-OCT and shear wave elastography, capable to allow rapid functional characterization of soft tissue mimicking phantom, *ex vivo* and *in vivo* cornea and skin tissue. Within the framework of this research, several objectives are defined and corresponding research conducted:

- I. To design and fabricate the PhS-OCT system to meet the requirements of high-speed shear wave imaging (SWI).

Using the Doppler effect of laser interference, PhS-OCT is able to provide high-sensitivity, depth-resolved motion detection. Based on the precise synchronization between OCT and mechanical wave source, repeated acquisition can replace the necessity of parallel system, to achieve adequate equivalent frame rate performance. The hardware and software of OCT system needs to be modified and the scanning protocol needs to be tested.

- II. Investigate the quality and robustness of OCT-SWI data, and carry out a study on the optimization of wave field data.

Similar to all other imaging modalities, certain imaging noise, aberration and artefacts could contaminate the OCT-SWI data, and consequently degrade the elastography results. Investigations are required to suppress these error and improve the SWI data quality.

- III. Consider and test the wave launching technique according to the requirements for different applications.

Both the applicability of SW-OCE for specific applications and the wave propagation data quality is dependent on the mechanical wave launching technique. A range of wave generation techniques of both contact and non-contact scheme are proposed and tested, and the feasibility of each type of wave launching technique is demonstrated.

- IV. Develop and optimise an elastic modulus recovery algorithm.

To develop a proper methodology for OCT-SWI data to quantify localized elastic modulus and generate 2D mapping, which is, in nature a method for recovering shear wave velocity from wave propagation data. The method needs to be applied to the conditions as close to clinical application as possible to examine the quantitative reliability.

- V. Perform pre-clinical studies to assess the feasibility of the proposed device such that the concept and design of this technique can be confirmed.

Taking a further step from phantom experiments, *in vivo* tissues are measured for SW-OCE to reconstruct elastic modulus map, and provide a micron-level OCT structural image simultaneously to show the ability of the proposed system for evaluating the elasticity of heterogeneous tissue in pre-clinical applications.

1.2. Thesis Outline

Chapter 2, Technical Background serves as the background overview of the thesis. An introductory overview of tissue biomechanics and measurement of tissue biomechanics is necessary to understand the motivations of dynamic elastography study. More specifically, the biomechanics measurement of cornea and skin tissue are considered under the scope of the first phase of dynamic OCE development, hence the previous work on accessing the mechanical properties of these two type of tissue have been reviewed, and the results were discussed, meanwhile deriving the motivation of developing dynamic OCE.

An introduction of two relevant techniques in this study is also given in this chapter: Elastography and OCT, including the background theory, implementation method and relevant clinical applications. Starting from the existing elastography techniques and instruments, the benefits of dynamic elastography are depicted, and the superior imaging and motion detection performance of OCT are compared, leading to the proposal of dynamic OCE.

Chapter 3, Transient Mechanical Waves Theory and Modelling presents an overview of the theoretical analysis of transient wave motion in soft tissue. The different wave modes and their superposition are introduced, including longitudinal wave, shear wave, surface waves and Lamb waves, as well as a review of their applications in the field of biomedical engineering. The comprehensive understanding of different wave behaviours is aimed at providing the fundamental principles of dynamic elastography: the inversion solution of elastic modulus from wave velocity. Finite element method

(FEM) is utilized to simulate the generation and propagation of transient mechanical waves in biological tissue, as the feasibility study of dynamic OCE. Results of the contact induced wave and pulsed laser generated waves are given, working as a prediction and guidelines for the upcoming instrument designing and experimental procedures.

Chapter 4, Shear Wave Imaging Technique Using PhS-OCT presents the design and construction of a PhS-OCT system, according to the requirements for OCT shear wave imaging, along with the essential techniques developed for producing and optimizing the wave field images. This chapter provides a novel solution to capture the propagation of transient waves inside target OCT samples, with both high spatial resolution and high imaging frame rate, which is a necessary route for obtaining the elastography result with dynamic OCE. A significant contribution in this chapter is the analysis of the source of imaging artefact and the algorithm for compensating the artefact. A technique for improving the signal-to-noise ratio in SWI results using coded wave excitation is also proposed. The outcome of this chapter is a technique to obtain high quality SWI images for OCE reconstruction as described in the subsequent chapter.

Chapter 5, Shear Wave OCE and Applications presents the OCE experiments carried on tissue-mimicking phantoms and then tissue in *ex vivo*, or *in vivo* conditions. The shear wave velocity recovery algorithm was firstly introduced, and then applied to the SWI results from the above experiments. Different techniques of wave generation have been tested, including the contact mechanical stimulation, acoustic radiation force impulse, and pulsed laser. Each experimental setup was described, and the shear wave imaging results in these experiments were presented, followed by wave velocity map reconstruction. Direct visualization of the tissue shear modulus is provided and compared from these experiments. The effectiveness of the proposed dynamic OCE method has been demonstrated.

A summary of the findings and recommendations for future work conclude the thesis in *Chapter 6*. Further information related to this work, such as data processing codes, datasheets and technical drawings, can be found in the appendices.

1.3. Publication Arising from this Work

Peer-reviewed journal papers

- J-1. Shaozhen Song, Zhihong Huang, and Ruikang K. Wang. ‘Tracking mechanical wave propagation within tissue using phase-sensitive optical coherence tomography: Motion artefact and its compensation.’ *Journal of biomedical optics* **18**.12 (2013): 121505-121505

- J-2. Shaozhen Song, Zhihong Huang, Thu-Mai Nguyen, Emily Y Wong, Bastien Arnal, Matthew O’Donnell, and Ruikang K Wang, ‘Shear Modulus Imaging by Direct Visualization of Propagating Shear Waves with Phase-Sensitive Optical Coherence Tomography’, *Journal of biomedical optics*, **18** (2013), 121509-09.

- J-3. Thu-Mai Nguyen*, Shaozhen Song*, Bastien Arnal, Zhihong Huang, Matthew O’Donnell, and Ruikang K Wang, 'Visualizing Ultrasonically-Induced Shear Wave Propagation Using Phase-Sensitive Optical Coherence Tomography for Dynamic Elastography', *Optics Letters*, **39** (2014), 838-41.

- J-4. Thu-Mai Nguyen*, Shaozhen Song*, Bastien Arnal, Emily Y Wong, Zhihong Huang, Ruikang K Wang, and Matthew O’Donnell, 'Shear Wave Pulse Compression for Dynamic Elastography Using Phase-Sensitive Optical Coherence Tomography', *Journal of biomedical optics*, **19** (2014), 016013-13.

- J-5. Chunhui Li, Shaozhen Song, Guangying Guan, Ruikang K. Wang, Zhihong Huang, ‘Frequency dependence of laser ultrasonic SAW phase velocities measurements.’ *Ultrasonics* **53**.1 (2013): 191-195.

- J-6. Chunhui Li, Guangying Guan, Fan Zhang, Shaozhen Song, Ruikang K. Wang, Zhihong Huang, Ghulam Nabi, ‘Quantitative elasticity measurement of urinary bladder wall using laser-induced surface acoustic waves’, *Biomedical Optics*

Express, 5.12 (2014) 4329-4337.

- J-7. Thu-Mai Nguyen, Bastien Arnal, Shaozhen Song, Zhihong Huang, Ruikang K. Wang, Matthew O'Donnell, 'Shear wave elastography using amplitude-modulated acoustic radiation force and phase-sensitive optical coherence tomography', *Journal of Biomedical Optics*, in review.
- J-8. Chunhui Li, Guangying Guan, Yuting Ling, Ying-Ting Hsu, Shaozhen Song, Jeffrey T.-J. Huang, Stephen Lang, Ruikang K. Wang, Zhihong Huang and Ghulam Nabi1, 'Detection and characterisation of biopsy tissue using quantitative optical coherence elastography (OCE) in men with suspected prostate cancer.', *Cancer Letters*, in publish.

Authors marked with asterisk contributed equally. In all of the published work, the author is responsible for OCT system modification and operation, experiment planning, data processing and analysis. In articles [J-3] and [J-4] the ultrasound stimulation planning and ultrasound data processing are performed by collaborator, Dr. Nguyen. Projects described in [J-5],[J-6] and [J-8] are carried out at University of Dundee.

Conference oral presentations

- C-1. Shaozhen Song, Zhihong Huang, Thu-Mai Nguyen, Emily Y Wong, Bastien Arnal, Matthew O'Donnell, and Ruikang K Wang, 'Shear Wave Elastography Using Phase Sensitive Optical Coherence Tomography', in SPIE BiOS (International Society for Optics and Photonics, 2014), pp. 89340U-40U-6.
- C-2. Shaozhen Song, Zhihong Huang, and Ruikang K Wang, 'Assessing Cross-Sectional Elasticity Map by Dynamic Imaging Acoustic Waves with Phase Sensitive Optical Coherence Tomography', in Ultrasonics Symposium (IUS), 2013 IEEE International (IEEE, 2013), pp. 1166-69.
- C-3. Shaozhen Song; Zhihong Huang; Thu-Mai Nguyen; Emily Y. Wong; Bastien

Arnal; Matthew O'Donnell; Ruikang K. Wang, 'Shear wave elastography using phase sensitive optical coherence tomography', Proc. SPIE Vol.8934, 10.1117/12.2040033

- C-4. Shaozhen Song, Nhan Minh Le, Zhihong Huang, Ruikang K. Wang, 'High speed imaging of remotely induced shear waves using phase-sensitive optical coherence tomography' SPIE BiOS (International Society for Optics and Photonics, 2015) 9312-51
- C-5. Shaozhen Song, Nhan Minh Le, Zhihong Huang, Ruikang K. Wang, 'Quantitative shear wave optical coherence elastography(SW-OCE) with acoustic radiation force impulses(ARFI) induced by phase array transducer' SPIE BiOS (International Society for Optics and Photonics, 2015) 9327-29
- C-6. Thu-Mai Nguyen, Shaozhen Song, Bastien Arnal, Zhihong Huang, Matthew O'Donnell, and Ruikang K. Wang 'Amplitude-modulated ultrasound radiation force combined with phase-sensitive optical coherence tomography for shear wave elastography', SPIE BiOS (International Society for Optics and Photonics, 2015) 9327-4

Conference poster presentations

- P-1. Shaozhen Song, Joyce Joy, Zhihong Huang, Ruikang K. Wang, 'Mapping tissue shear modulus on Thiel soft-embalmed mouse skin with shear wave optical coherence elastography' SPIE BiOS (International Society for Optics and Photonics, 2015) 9327-33

2. TECHNICAL BACKGROUND

2.1. Introduction

This chapter is an introduction to the basic concepts, principles and existing elastography techniques.

In this chapter:

- * Cornea and skin tissue biomechanics introduction

The previous work on accessing the mechanical properties of these two types of tissue have been reviewed, and the results were discussed, meanwhile deriving the motivation of developing dynamic OCE.

- * Technical background of relevant techniques:

Elastography and OCT, including the background theory, implementation method and relevant clinical applications are reviewed. Starting from existing elastography techniques and instruments, the benefits of dynamic elastography are depicted, and the superior imaging and motion detection performance of OCT are presented, leading to the proposal of dynamic OCE.

2.2. Tissue Biomechanics

Biomechanics is mechanics applied to biology, or the study of motion or equilibrium of biological materials and forces that cause such motion or equilibrium [1]. Biomechanics has been a historical research topic since the Greek classic *On the Parts of Animals* by Aristotle (384-322 B.C.), which provided a comprehensive description of the anatomic mechanism of internal organs. Modern biomechanics is rapidly developing by receiving impetus from engineering, enabling measurements and analysis of biomechanics on atoms, molecules, cells, tissues, organs and individual organisms.

Biomechanics has participated in a broad range of modern advance of medical science and technology. For an organism, biomechanics helps us to understand the functionalities of tissue or organ, to predict some possible changes with specific alterations, and to propose artificial intervention approaches. Modern medical science including diagnosis, surgery, and prosthesis are closely associated with biomechanics. For instance, biomechanics has helped in solving clinical problems in the cardiovascular system with the invention and analysis of prosthetic heart valves, heart assist devices, extracorporeal circulation, the heart-lung machines and the hemodialysis machines. It plays a major role in advancing the art of heart transplantation and artificial heart replacement. In the long term, the methodology of biomechanics will be adopted to deal with many complex problems of health science and technology.

The topic of this dissertation, the measurement of tissue mechanical properties is a fundamental subject of biomechanics. A comprehensive mechanical model relies on the correct understanding of mechanical properties, which helps us to understand many biological processes, for example the development of engineered smooth muscle tissue can be regulated by the cyclic mechanical strain[3].

Furthermore, the alteration of mechanical properties with the change of tissue

condition is commonly observed in tissue pathologies, such as in skin disorders and tumours. Thus, assessing tissue mechanical properties is useful in improving our understanding of tissue patio-physiology, which will aid medical diagnosis and treatment of a range of disease including cancer.

In bio-solid mechanics, we adopt the methodology and standards of classical mechanics to study the function of biological tissues and organs while attempting to account for their biological nature wherever possible. In the human body, there are many soft (artery, skin, muscle, etc.) and hard tissues (bone, trachea etc.), each associated with distinct mechanical behaviour. There are many facets to mechanical “behaviour”, since biological tissue acts very different for each tissue type. Figure 2-1 compares the elastic curves between a common engineering material, steel and some biological tissues. In soft tissues, important parameters of mechanical properties include elasticity (Young’s modulus), Poisson ratio and density. The Poisson’s ratio and density do not vary much, as it is usually in the range of 0.490 to 0.499 as biological soft tissues are usually hardly compressible, and the corresponding values of density are 920 to 1060 kg/m³ [4].

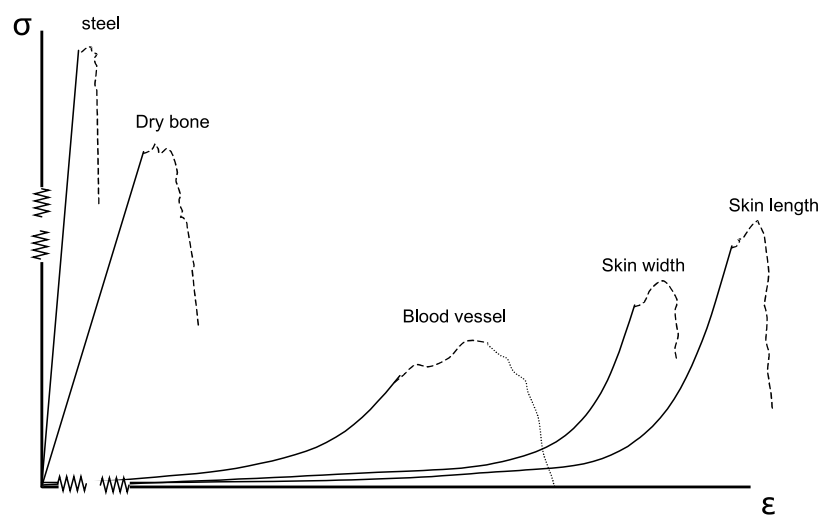


Figure 2-1 A comparison of stress-strain curve for steel and various biological tissue

Young’s modulus describes the strain response to a stress, as the ratio of stress and strain. As shown in Figure 2-1, as a typical soft tissue, when a piece of tissue is

subjected to a force, the strain increases rapidly, and linearly below a proportional limit. In this small strain situation, the tissue is in relaxed state, where the Young's Modulus represents the elasticity of tissue. Once the strain rises above the proportional limit, more and more collagen and fibre structure becomes tighten, and starts to contribute to the elastic modulus. Hence the stress-strain response becomes non-linear. Due to the anisotropic nature of fibre distribution in soft tissue, the Poisson's ratio is not accepted to describe the directional response of anisotropic tissue, e.g. cornea. In this study, the Poisson's ratio is approximated as 0.49, it is useful to notice that this value should not be used for deriving Young's Modulus in in vivo experimental results.

The effectively linear region of stress-strain curve is usually used to get the estimation of tissue elasticity when tissue is relaxed, with no mechanical load. However, in the case of cornea and skin, the tissue is substantially under mechanical load, either from the intraocular pressure, or the skin tension. A more accurate mechanical properties estimation should be based on the given beyond the proportional limit in the stress-strain curve. Tangent modulus is the slope of the stress-strain curve at any specified stress or strain. In this study, the aim of the development to shear wave optical coherence elastography (SW-OCE) technique is to provide Young's Modulus values or shear modulus values. However, more strictly, the in vivo experiments with SW-OCE approach can only provide the tangent modulus under the specific load.

2.3. Measurements of tissue biomechanics

As an imaging modality that is designed for imaging superficial tissue structures, OCT has the most successful application in ocular tissue and skin. In this dissertation, two tissue types are the main objects for the optical imaging techniques, namely skin and cornea.

In the past two decades, the mechanical properties of the soft tissue, in particular the aforementioned two types of tissue have been studied extensively.

2.3.1. Biomechanics of skin

Skin, as the largest organ of human body, is an important subject for measurements of biomechanics. Many complex physiological activities is dependent on skin functionalities: fluid homeostasis, immune surveillance, sensory detection, and thermoregulation. Much of the research on human skin has mainly focused on reconstruction, wound healing, transplantation, and manipulation. The study of skin functionalities is also extended to assess pharmacologic functions of a variety of toxins, prescription drugs, and cosmetic treatments[5].

Biomechanical properties of skin are of great significance as they are directly responsible for the skin pathological status, structural integrity, cosmetics and aging. The active and passive functions of skin are regulated by cells and structures located within the layered architecture. With pathological changes or aging effect in human skin, the biomechanical properties will be altered for different layers or specific regions. The quantitative estimation or visualization of these changes are consequentially more important than subjective observations for diagnosis of skin conditions or for monitoring of therapeutic effects.

A number of techniques have been used for measuring skin mechanical properties. Owing to the physiological relevance of direct mechanical testing, it is the most commonly employed method that directly measures the overall mechanical properties of skin in vitro. Single-axis tensile test method has long been used to observe the stress-relaxation of mouse and human skin samples for exploring the role of elastin in the skin mechanical properties[6], as well as tangential traction method is used to determine the biomechanics of finger pad skin[7]. As skin tissue is easy accessible by medical devices, in vivo estimations are also carried out with various techniques. For example, ultrasound was used to determine skin thickness and mechanical properties in vivo [8]. A tangential traction method was used to determine the biomechanics of finger pad tissue in vivo [7]. Young's modulus, initial stress, and index of non-elasticity of skin were characterized using a mechanical model under suction [9].

However, among the large amount of studies in skin mechanical properties, there are limited references that provided quantitative skin elastic modulus results. The

visualized elastogram results in the investigations of skin elastic properties are further limited. A review of the literature published on the topic of skin mechanical properties is given in Table 2-1. In this table, the big variation of Young's Modulus values are not only from the conditions when then measurements are performed, but also due to the quantitative measurement parameters variations.

Table 2-1 Measurement of skin mechanical properties, including skin elastography results from published literature

References	Skin Layer/Tissue	Approach	Quantitative value provided	Value	Density (kg/m ³)	Poisson's ratio	Mapping provided	Resolution
Sanders <i>et al.</i> [6]	Skin in general (various anatomical sites)	<i>Ex vivo</i> axial mechanical load	Young's Modulus (E)	24-107 kPa	NA	0.5	No	N/A
Wang <i>et al.</i> [7]	Finger, palm	Traction	Young's Modulus (E) Compression/shear test	1.54-3.61 MPa	NA	N/a	No	N/A
Diridollou <i>et al.</i> [9, 10]	Skin in general (forearm)	Suction response	Young's Modulus (E)	153 kPa	NA	0.5	No	N/A
Barel <i>et al.</i> [11]	Skin in general (various anatomical sites)	Suction response	Young's Modulus (E)	130-260 kPa	NA	0.5	No	N/A
Childers <i>et al.</i> [12]	Epidermis Dermis(forearm)	Suction response	Young's Modulus (E)	2 MPa 500 kPa	1116 1110	0.3 0.33	No	N/A
Zhang <i>et al.</i> [13]	Skin in general (back)	Surface wave velocity	Young's Modulus (E)	526 kPa	1000	N/A	No	N/A
Gennisson <i>et al.</i> [14]	Dermis, Subcutaneous Fat (forearm)	Lamb wave velocity	Young's Modulus (E)	1.5 MPa 5.0 kPa	1100 1100	N/A N/A	Ultrasound image only	N/A
Liang <i>et al.</i> [15]	Epidermis, Dermis(forearm, palm)	Surface wave velocity	Young's Modulus (E)	300 kPa 150 kPa	1020 1020	0.5 0.5	OCT image only	N/A
Kennedy <i>et al.</i> [16]	Epidermis, Dermis (fingertip)	Dynamic vibration	No	N/A	N/A	N/A	Yes	40 um

The quantitative measurement from published literatures varies in the measured parameter, and for the Young's modulus measurements, the values are also scattered due to the nature and condition of the measured skin, such as: (a) Dermal collagen and elastic fibers network; (b) Extracellular matrix contents (c) External factors such as individuals' age, gender, race, health and nutritional status, or even skin temperature.

There are also a few studies using wave propagation methods to obtain localized mechanical property measurements[13]. Among those methods, transient wave elastography is the only method that provide both quantitative values and mapping results, nevertheless, transient elastography, especially the optical elastography technique is still under continuing development to achieve satisfactory performance for clinical applications.

2.3.2. Biomechanics of cornea

The cornea is the most important optical structure in the eye and responsible for 60% of its refractive power. Small alteration from its physiological state, such as irregularities in its shape and surface, induce aberrations and reduce the visual performance. Thereby the corneal shape is determined by its microstructure and biomechanical properties. Recent studies has also reported the effects of corneal mechanical properties on tonometry[17], given the fact that stiffness of cornea is a major parameter in maintaining the intraocular pressure (IOP). A better understanding of cornea stiffness benefits many ophthalmological procedures such as the determination of IOP, pathological diagnosis, and planning of surgical interventions.

In the physiologic condition the stress-strain distribution in the cornea is equilibrated. However this equilibrium gets disturbed when corneal tissue is removed (LASIK, PRK) or material is added within the cornea (ICRS). Therefore corneal reshaping and hence the outcome of refractive surgeries depends to a large extend on the immediate biomechanical response of the cornea, but also on later ongoing wound healing

effects[18, 19]. The structural equilibrium of the cornea gets also disturbed in certain pathologies, such as keratoconus, where the cornea suddenly becomes unstable and starts deforming non-uniformly[20]. This induces a high amount of aberrations resulting in a continuously degrading vision. What makes the estimation of corneal biomechanical property a promising assisting technique is that, the measurement results would provide valuable information for new treatments, such as femtosecond laser based transplant of cornea[21]. Furthermore, accurate estimation of corneal mechanical properties will also lead to a better control of the risks of abnormalities after refractive surgeries, or improve the accuracy in detecting corneal deformation disease[22].

In vitro cornea biomechanics measurements

Most of the assessment of the cornea stress-strain response experiments are done *in vitro*, since it is the most direct measurement of the Young's modulus.

Strip extensionmetry is the most commonly performed assessment of corneal mechanical properties. In these measurements the enucleated eye is normally eviscerated and the central cornea were cut into small strips. The strips are subsequently placed in stress-strain extensometer with the help of appropriate clamping[23]. With this technique, the general mechanical property of cornea were studied, including the viscoelastic behaviour[24] and non-linearity at high stresses [25]. A few limitation of uni-axial stress strain tests in corneal tissue are that 1) the cutting of cornea samples changed the stress distribution along the tissue compared to natural condition[18]; 2) Flattening of originally curved specimen induces tensile strain and compressive strains on opposite sides of cornea, and 3) approximations of uniform cornea thickness[26].

Whole eye inflation is another *in vitro* method for studying biomechanical properties of cornea. In this technique, the corneal expansion can be studied in its natural environment, which is in the surrounding with limbus and sclera. The inflation is normally achieved using a needle into the anterior chamber allowing to control the intraocular pressure (IOP)[27, 28]. The limitation of this estimation method is that the

expansion behaviour is a combination of cornea and sclera deformation, hence only approximations for the overall mechanical property is obtained.

***In vivo* methods**

In vivo measurements are even more challenging. Due to the requirement for being non-invasive or minimally invasive, *in vivo* techniques typically assess the corneal mechanical property even more indirectly than *in vitro* techniques do. *In vivo* Eye inflation were performed by Pallikaris et al [29] in eye-surgery and measured the relation between infused volume and intraocular pressure.

For non-invasive *in vivo* test, the Ocular Response Analyzer (ORA) has been the first FDA approved device to measure corneal biomechanics, which is based on air-puff stimulation and deviation sensor of corneal deformation. A few parameters can be estimated, such as corneal resistance factor (CRF)[30], corneal hysteresis (CH), and Corneal compensated IOP[31], etc. A systematic study of corneal thickness and age-related mechanical property was carried out with ORA[32]. However, none of these results gives a localized visualization of corneal mechanical property distribution, nor is the quantitative modulus obtained.

Corneal elasticity mapping

Since a quantitative, accurate spatial assessment of the cornea mechanical property is crucial to a variety of ophthalmology procedures, the quantitative 3-D mapping of cornea elasticity, or its Young's modulus, has attracted more and more research interests in the past few years.

Similar to the elastography techniques in other human organs, the most widely adopted elasticity mapping technique is ultrasound. An elastography system was proposed by Hollman et al. to image the strain in porcine cornea[33]. The device proposed in this work measures the static compressional strain induced by a plate attached to cornea, hence the inversion of Young's modulus would be a complex problem, which remains to be solved properly in order to achieve an accurate quantitative measurement for

clinical requirements.

In comparison with static/quasi-static elastography, which only provide relative estimation of stiffness given the limited information of stress distribution, transient elastography is more promising to provide elastic modulus measurements. Surface wave method is one of the transient methods proposed to access the mechanical property in cornea[34]. The surface wave propagation velocity can be measured by the OCT at two fixed-distances on sample surface, and the wave dispersion behaviour is studied. The results of wave velocity were repeatable and convincing, and relative stiffness changes were observed at given locations.

Recently, the technique of supersonic shear wave imaging (SSI) were introduced for corneal stiffness estimation. The first 2-D sectional image of cornea elasticity was given in [35]. In contrast to the Ocular Response Analyser (ORA), SSI scheme only applies very small motion amplitude to the cornea, using linear ultrasound array focused beam. The SSI technique captures the cornea transient response with very high frame rate, and the 2-dimensional wave propagation movie was analysed to extract the cornea stiffness map. Later in a follow up study[36], SSI was performed both ex vivo and in vivo on porcine cornea, and the results of cornea stiffness map was given in 2-dimensional and 3-dimensional. The Young's modulus increase of collagen cross-linking treated area was concluded, with a spatial resolution of 200 microns.

There are some unavoidable drawbacks and limitations of the existing ultrasound based corneal elasticity mapping techniques. Firstly, the coupling media that is required by ultrasound imaging is technically difficult to achieve, especially in clinical conditions. Secondly the ultrasound imaging ability is limited in resolution, which decreases the practicability for preoperative planning of ocular tissue refractive surgery.

2.4. Elastography

2.4.1. Physics of elastography

Biopsy is the standard invasive method for diagnosing and prognosing cancers. For instance, histo-pathological examination of a prostate specimen obtained by core needle biopsy has traditionally been considered the gold standard for prostate cancer evaluation. However, biopsy is a painful procedure with sampling errors and intra- and inter-observer variability results in over or under-estimation and its application is inefficient for serially repeated assessment of disease progression.

As an assisting tool for diagnosis, cross-sectional imaging-based elastography techniques have become popular because of their added abilities for high-speed, high-resolution measurements, morphological changes in disease, and assessment of biomechanical properties. It is feasible to distinguish between benign and malignant tissues by comparing their elasticity moduli. Elastography has been found to be helpful in detecting breast[37, 38], thyroid[39], prostate[40], and liver abnormalities[41].

Elastography techniques can be classified as static methods and dynamic methods, based on their temporal characteristics of excitation[42]. In static methods, mechanical excitations are considered to be slow and tissue displacements are usually considered as indications of tissue biomechanical properties[43]. Dynamic methods rely on solving wave equations, which in their differential form are local in character[44]. Elastography techniques can also be classified as external and internal methods, based on their spatial characteristics of excitation. External excitation elastography methods often apply a stress to deform tissue from outside when imaging[43], while internal excitation elastography methods apply mechanical excitation directly into the region of interest in tissue. The radiation force of ultrasound is usually used as an internal excitation in elastography techniques[45].

Resolution and penetration of elastography techniques depend on their imaging modalities. For instance, the typical resolution of ultrasound elastography is between 125 and 200 μm [46], while resolution in MRI elastography is usually of millimetre scale[47]. The resolution and penetration of some imaging modalities are shown in Figure 2-2.

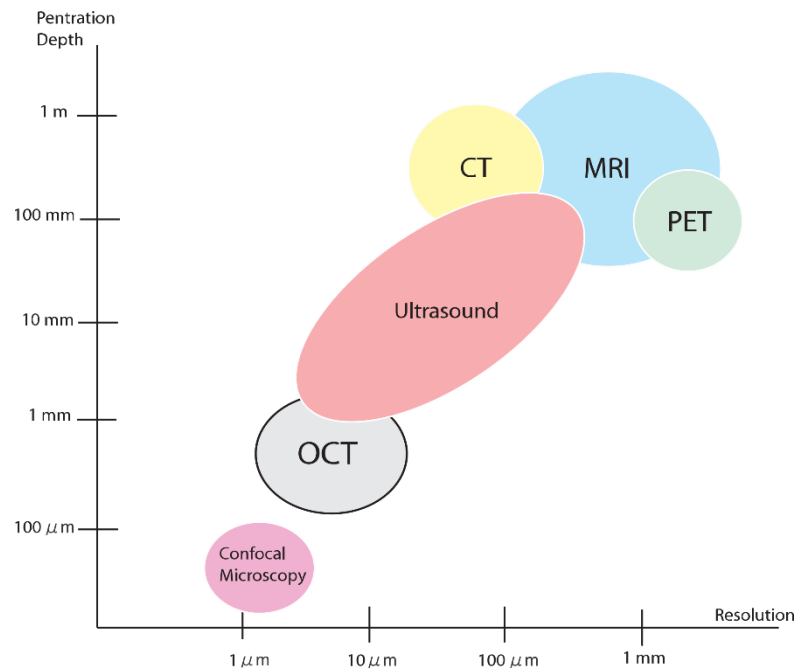


Figure 2-2 Comparison of various medical imaging modalities in terms of resolution and penetration depth

2.4.2. Elastography with medical imaging devices

Ultrasound elastography

In quasi-static compression elastography, ultrasound signals are recorded before and after a controlled mechanical compression is applied to the tissue. Displacement between the two data sets is estimated by cross-correlation. Strain is then computed by measuring the spatial derivative of the displacement. Traditionally only axial strains are estimated and lateral and elevational motions are ignored.

Compared to other elastography techniques, traditional ultrasound elastography generates displacement by hand rather than with the aid of additional hardware. Thus it has the advantage of easy implementation and low cost. However, the quality of the processed strain image is highly dependent on the accuracy of the displacement estimation. The factors degrading displacement estimation include electronic and quantization noise and lateral and elevational motions. Another major limiting factor is the non-stationary characteristic of compression, which makes the signal before and

after compression jointly non-stationary. In other words, the post-compression signal is not exactly the delayed version of the pre-compression signal due to the distortion of compression. Only when a small enough displacement is introduced to the tissue can the two signals be assumed jointly stationary, so that the distortion can be compensated. The traditional way of cross correlation is to fraction signals by window and then fit the pre- and post-compression signals locally. Both additional stretching of the pre-compressed signal[48] and adaptive stretching approach[49] improve the correlation results. Nevertheless, this quasi-static compression method for measuring a relative tissue stiffness have proven effective in many studies [2, 42, 50].

Acoustic radiation force is a phenomenon associated with the propagation of acoustic waves through a dissipative medium. ARFI imaging, first introduced by Nightingale et al.,[51] uses a series of high-intensity short-duration (0.03-0.4 ms)[52] ultrasound pushing beams to generate localized displacements (between 1 and 20 microns in soft tissue)[53] and these displacements are tracked by standard diagnostic ultrasound pulses of low pulse repetition frequencies (PRF) (3 to 12 kHz) using ultrasonic correlation-based methods. The tissue response to these forces is monitored both spatially and temporally. Images are taken of maximum tissue displacement through time, the time it takes for tissue to reach its peak displacement, and tissue recovery time to depict the tissue's stiffness and shear modulus[45]. Sarvazyan et al. introduced Shear wave elasticity imaging (SWEI)[54] The modality uses radiation force to displace tissue and the speed of shear waves generated after force removal is monitored to characterize variations in tissue shear modulus.

A single transducer on a diagnostic scanner is used both to generate the radiation force and to track the resulting displacements. The ARFI images are co-registered with B-mode and colour Doppler images. Thus ARFI elastography has the advantages of portability and low operating costs compared with CT and MRI modalities.

ARFI has been applied to artery characterization[45], colorectal tumour imaging[55], breast lesion detection[56], diagnosis of liver fibrosis, and guidance of radiofrequency (RF) ablation procedures for heart[57] and liver[58].

Magnetic Resonance Elastography

MRE is a phase-contrast based MRI technique for direct visualization and quantitative measurement of propagating mechanical shear waves in biologic tissue. The technique is used to obtain spatial maps and measurements of shear wave displacement patterns. Dynamic shear waves ranging from 50 to 1000 Hz are selected to generate displacement in tissue for the model in consideration of attenuation and resolution. The MRI provides an ability to detect the displacement, and resulting images with spin displacement information are processed to generate elasticity maps, which show local quantitative values of the shear modulus of tissues[59].

In addition to MRE, there are other investigations using MRI for tissue elasticity evaluation. One method is to employ a motion-encoded phase-contrast imaging sequence for spatial strain distribution estimation, based on which elastic modulus is calculated[60]. The vibration is introduced by a small quasi-static longitudinal stress occurring once every time that the imaging sequence is generated. Another technique is to apply saturation tags to tissue before static stress is introduced. The deformation information from the tags is then used for strain estimation, which in turn gives the elasticity modulus[61].

2.5. Optical coherence tomography

2.5.1. Development and theory of OCT

The first report of OCT application on biological tissue was introduced in 1988 by Fercher et al.[62], where low-coherence technique was first used for measuring the geometries of human eye. Before that, similar methods had been used in the related technologies of low-coherence interferometry (LCI)[63], optical coherence-domain reflectometry (OCDR)[64], and optical time-domain reflectometry (OTDR)[65]. LCI was used as an interferometric thickness gauge to measure variations in moving transparent films while OCDR and OTDR were used as 1-D optical evaluation tools to determine positions and magnitudes of reflection sites in fiber optic cables. OCT combined these interferometric techniques with broad-band near-infrared laser sources and a transverse scanning mechanism through a focusing lens to achieve two-dimensional (2-D) cross-sectional or three-dimensional (3-D) imaging. High resolution, non-invasive and real-time processing are the main beneficial features of OCT.

The principle of OCT is to depth-resolve optical scattering variations within a sample using optical interferometric techniques, in which the axial resolution is determined by the coherence length of the laser source while the transverse resolution is determined by the spot size of the incident beam. OCT is a non-invasive biomedical imaging modality and has been successfully applied in ophthalmology to image morphological changes in the retina[66]. This technology has also been investigated in other medical fields such as oncology, dermatology, cardiology, gastroenterology, neurosurgery, and developmental biology [67-71].

The early OCT studies mainly used time-domain OCT (TD-OCT) systems. A typical simplified interferometric setup is given in Figure 2-3.

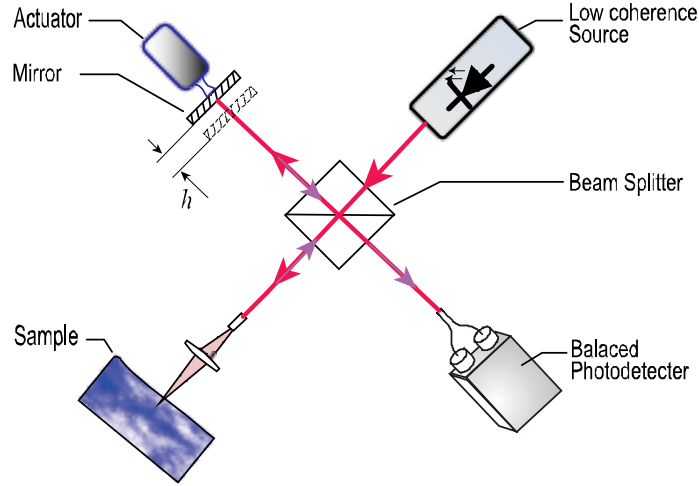


Figure 2-3 A basic setup of time-domain OCT system

A low-coherence near-infrared light source is split into two arms, namely reference and sample arms, using a beam splitter. The beams that return from the reference and sample arms are combined to produce an interference signal which is detected using a photoelectric detector. Let U_R be the optical field backscattered from the reference arm and U_S be the field from the sample arm. Then the intensity detected by the detector will be

$$I_d = \langle |U_d|^2 \rangle = \langle |U_R(t + \tau) + U_S(t)|^2 \rangle = I_R + I_S + 2 \operatorname{Re} \left\{ \langle U_R(t + \tau) U_S^*(t) \rangle \right\} \quad [2.1]$$

where τ is the time delay between the two arms. The last term can be expressed as

$$\operatorname{Re} \left\{ \langle U_R(t + \tau) \cdot U_S^*(t) \rangle \right\} = \operatorname{Re} \{ G(\tau) \} = |G(\tau)| \cos(2\omega_0 \tau) \quad [2.2]$$

$G(\tau)$ is the temporal coherence function and can be written as:

$$G(\tau) = \langle U_R(t + \tau) \cdot U_S^*(t) \rangle = \exp \left[\left(\frac{\Delta\omega\tau}{4\sqrt{\ln 2}} \right)^2 \right] \exp(-i\omega_0 \tau) \quad [2.3]$$

where ω_0 is the central wavelength and $\Delta\omega$ is the wavelength deviation. When a perfect reflector is placed at the sample, $\operatorname{Re} \{ G(\tau) \}$ can be recognized as the point spread

function (PSF) or impulse response of the system, which is illustrated in Figure 2-4(b1), and the detected signal is the envelope of the convolution of the PSF and the reflector structure function (a 1-D Dirac delta function), as shown in Figure 2-4(b2).

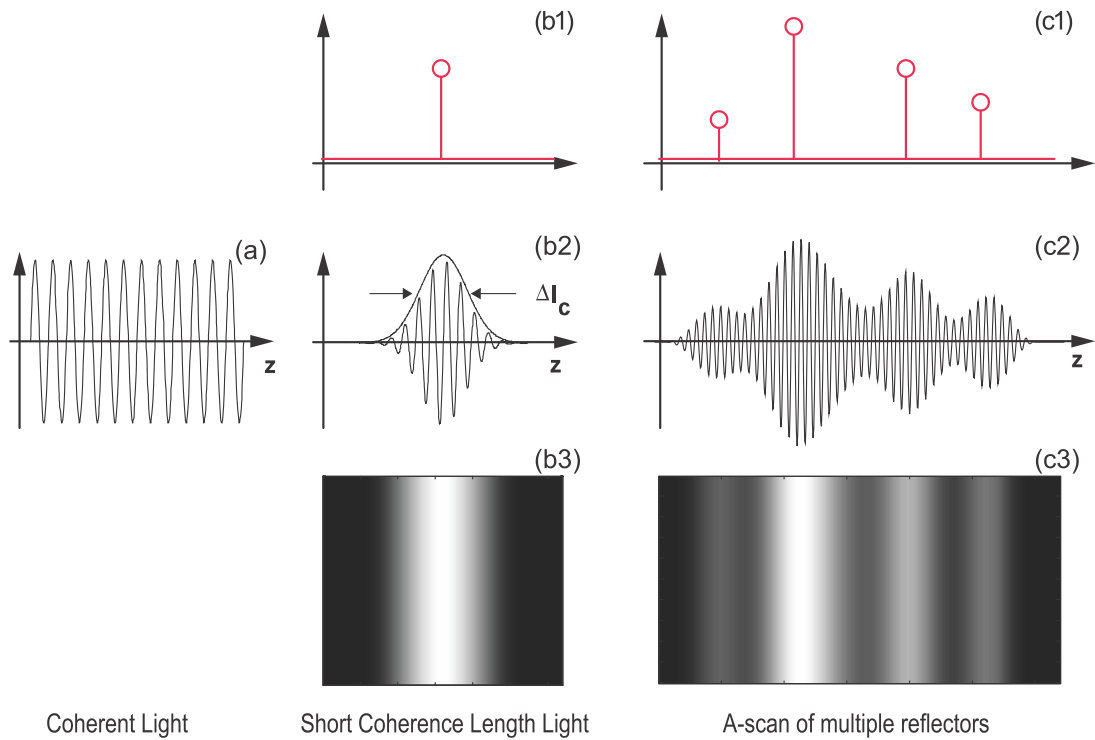


Figure 2-4 Illustration of simulated interferometry signal and image in a low-coherence imaging system

In time-domain OCT, as the reference arm mirror is moved, the path length h between the two arms is changed and hence the delay τ is changed. When there are multiple scatterers in the sample instead of a perfect reflector, the axial scan (A-scan) signal detected will resemble that in Figure 2-4. This signal can be seen as a convolution of the point spread function and the structural function in the sample. By scanning the sample beam transversely, a 2-D image can be formed.

Fourier-domain OCT (SD-OCT) is an extension of time-domain OCT[72]. A typical type of SD-OCT is spectral-domain OCT (SD-OCT), as shown in Figure 2-5. Instead of the moving mirror, SD-OCT has a fixed mirror in the reference arm and a spectrometer as a detector. The structural information of the sample is obtained in the spatially encoded frequency components of the detected OCT signal and then

reconstructed by the fast Fourier transform.

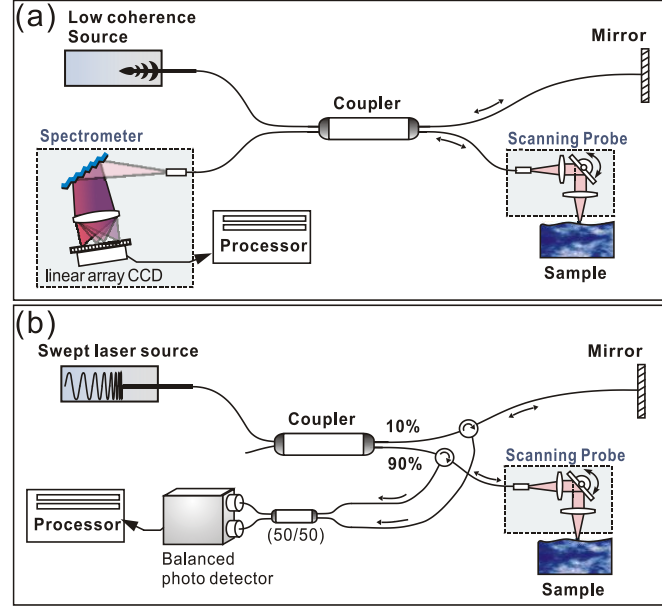


Figure 2-5 Typical SD-OCT(a) and SS-OCT(b) system setup

Since there are no physically moving parts, an SD-OCT system has a much higher stability and acquisition speed than a TD-OCT system. Another type of SD-OCT is swept-source OCT (SS-OCT). In this technique, the spectral components are not encoded by spatial separation, but are encoded in time. The light source spectrum is either filtered or generated in single successive frequency steps[73, 74]. Due to the unique sweeping method, SS-OCT can achieve much faster acquisition speed than its counterparts, which can be as high as 370,000 A-scans per second[75].

2.5.1. Performance parameters of OCT

Axial resolution is a very important specification for OCT imaging since high axial resolution is critical to differentiate structural features of cells and tissues. Axial resolution of an OCT system is determined by the central wavelength and wavelength bandwidth of the laser source. The coherence length of the source can be written as

$$l_c = \frac{2c \ln 2}{\pi} \cdot \frac{1}{\Delta \nu} = \frac{2 \ln 2}{n\pi} \cdot \frac{\lambda_0^2}{\Delta \lambda} \approx 0.88 \frac{\lambda_0^2}{\Delta \lambda} \quad [2.4]$$

where n is the refractive index of the sample, and λ_0 and $\Delta\lambda$ are the central wavelength and full width at half maximum (FWHM) bandwidth of Gaussian source spectrum, respectively. Normally the axial resolution is defined as half of the coherence length:

$$R_a = \frac{l_c}{2} = 0.44 \frac{\lambda_0^2}{\Delta\lambda} \quad [2.5]$$

Thus, for example, if an OCT system has a Ti-Sapphire laser source with central wavelength of 800 nm and FWHM bandwidth of 100 nm, theoretically, this system has an axial resolution of about 2.8 μm in air.

The transverse resolution of OCT is determined by the objective lens in the sample arm and can be defined as the spot size of the sample beam, which can be written as

$$R_T = 2w_0 = \frac{4f\lambda_0}{\pi D} \approx 1.22 \frac{\lambda_0}{2NA_{obj}} \quad [2.6]$$

where $2w_0$ is the spot size diameter of the beam, f is the focal length of the sample arm objective lens, and D is the beam diameter incident onto the lens, and NA_{obj} is the numerical aperture of the objective lens. However, there is a trade-off between the transverse resolution and depth of field b , since b can be written as

$$b = 2z_0 = \frac{2\pi w_0^2}{\lambda_0} \quad [2.7]$$

From equation 2.6, one can observe that if the transverse resolution is improved, the actual depth of field of the beam is decreased, which blurs the area outside the focusing depth in the image. This trade-off is intrinsic in OCT and microscopy in general, but may be improved by applying synthetic apertures[76].

Signal to noise ratio (SNR) is another important specification for OCT images. SNR of an OCT system can be defined as the ratio of the signal power generated by a perfectly reflecting mirror to the noise of the system. The dominating noise sources

are shot noise, excess intensity noise, and receiver noise. Shot noise comes from the sampling of the discrete ‘packets’ of photons, and is determined by the sensor. The excess intensity noise can be avoided by controlling the receiver sensitivity and laser source output energy. Receiver noise can either be calculated from manufacturer specifications or modelled as thermal noise. In the case of broad bandwidth light, the photocurrent noise has two terms: shot noise due to photocurrent variance and excess noise due to self-beating of broad-band light waves[77].

The axial imaging depth of an OCT system is an essential measure of imaging performance. In scattering tissue and other turbid media, the depth scan is limited primarily by optical scattering, and hence maximum reported imaging depths are between 1 and 3mm for a variety of tissues. Within this range, the maximum imaging depth of OCT systems depends on centre wavelength of light source utilized. The light source popularly used for current OCT systems are centred at 820 nm, 1060 nm or 1310 nm. The first two are mostly used for human posterior eye imaging, because the absorption of water is relatively low which allows enough power to reach the retina. Whereas 1310 nm centre wavelength are used for imaging other tissues, including skin, brain tissue, coronary artery, etc. 1310 nm can provide deeper penetration depth into tissue as compared to 820 nm light source. We can choose different centre wavelength light sources based on specific applications. In this thesis, both 820 nm and 1310 nm OCT system have been developed and utilized.

2.5.2. Phase sensitive OCT

Motion detection has been of remarkable research interest in the development and application of OCT[78]. By analysing the Doppler effect of a moving particle on light frequency, Doppler OCT allows the quantification of optical scatterer speed and direction. The most frequently used Doppler OCT technique is blood flow speed measurement[79, 80]. Vasculature can be visualized and quantified by OCT using the effect of motion caused by blood flow on the backscattered light. Zhao et al. proposed the phase-resolved Doppler OCT (PRDOCT) method[81], in which by evaluating the phase difference between adjacent axial OCT scans (A-scan), PRDOCT greatly

improves the detection sensitivity for imaging the blood flow velocity by decoupling the spatial resolution and velocity sensitivity. The initial implementation of PRDOCT was based on Hilbert transform[81], in which the phase of the Doppler signal is determined through the analytic continuation of the measured interference signals by Hilbert transform. By this implementation, a minimum velocity sensitivity as low as $100\text{ }\mu\text{m/s}$ with a resolution of $100\text{ }\mu\text{m/s}$ could be achieved. Moreover, by comparing the sequential A-scans at the same locations, the speckle modulations in the fringe signal cancel each other and will not affect the phase difference calculation. Doppler-OCT has been used for more than a decade to provide contrast based on blood flow.

Based on PRDOCT working principle, the function of OCT system can be extended to sensitive motion detection. In this thesis, PhS-OCT is utilized for capturing shear wave displacement field, and this technique is presented in detail in Chapter 4.

2.6. Optical coherence elastography

Optical elastography methods are based on optical imaging techniques. Optical elastography is capable of providing biomechanical properties from tissue structure level, down to sub-cellular level[78]. This dissertation focuses on the development of optical coherence elastography, based on the *in vivo* imaging modality, and unique in the excitation method. A review of the existing optical coherence elastography techniques is given below.

2.6.1. Static and quasi-static optical coherence elastography

In compression OCE, a static or step-wise external mechanical load is applied between OCT acquisitions. A local axial strain ε_l is estimated by measuring the change in displacement, Δu_z , over an axial depth range, Δz :

$$\varepsilon_l = \frac{\Delta u_z}{\Delta z} \quad [2.8]$$

The elastogram can thus be reconstructed according to this local strain, as a relative measure of the inverse of elastic modulus, since the corresponding local stress is unknown.

The first elastography technique based on OCT was reported in 1998[82]. The hardware and theory of operation of OCE were described and internal displacements indicating biomechanical properties of gelatine phantoms, pork meat and *in vivo* skin were shown by using 2-D cross-correlation speckle tracking algorithm. Since then, slow external mechanical excitation and static elastography based on speckle tracking methods (or cross-correlation algorithms in OCE) have been established for this technology[42]. The displacement sensitivity for this method was proportional to the axial resolution of the OCT system, which was usually several microns in tissues. The cross-correlation algorithms for OCE were then improved based on the scale of tissue

displacements.

Similar to ultrasound elastography, a major factor that determines the strain measurement accuracy in quasi-static OCE is the displacement estimation technique[83]. Compared to speckle tracking method, phase-sensitive OCT features higher displacement sensitivity and spatial resolution[78]. A phase-sensitive optical coherence elastography method was introduced later in 2007 when SD-OCT systems were widely used, from which phases of complex OCT data were more stable than TD-OCT systems[84]. Deformations, strain rates, and strains of soft tissue were measured by this method in real time with a sensitivity at the nanometre scale.

Analogously to ultrasound elastography, quasi-static compression is the most straightforward loading technique to implement, and also the most mature. Apart from the above mentioned early developments of quasi-static OCE, traditional OCE was used in many early studies [85-89]. In these studies, the elastogram quality was low due to the disadvantage of low resolution speckle tracking based on OCT intensity signal, which was employed to measure displacement. The adoption of phase-sensitive OCT detection methods in OCE has since improved elastogram quality [83, 90, 91].

2.6.2. Dynamic optical coherence elastography

In the past two decades, dynamic elastography and transient elastography are attracting many applications, especially in biomedical optics field, with the advantage of feasible internal excitation, and revealing the absolute moduli values of tissue dynamic properties. The transient methods of MRI elastography[92, 93], ultrasound elastography[94] and OCE, has been proved efficient in reconstructing elastic modulus maps for a variety of tissue types. Based on the stimulation methods of dynamic OCE, the dynamic OCE methods can be classified into a few categories: Compression OCE, Surface Acoustic Wave OCE (SAW-OCE), Magnetomotive OCE (MM-OCE) and Shear wave OCE(SW-OCE). An illustration of the loading schemes and elasticity estimation methods of these dynamic OCE techniques is shown in Figure 2-6.

Compression OCE

Adopting the same idea of quasi-static OCE, the dynamic compression OCE measures the vibration amplitude resulting from a sinusoidal external load, with a frequency range of 20-800 Hz. Also analogously to ultrasound elastography, a dynamic strain is calculated from the change in vibration amplitude gradient along the depth direction.

A dynamic OCE method was reported in [95] extracting Young's moduli from phase-resolved displacement that was excited by piezoelectric rod actuator operating at 100 Hz to kilohertz frequency. Adie et al.[96] proposed the OCE technique based on determining vibration amplitude from the analysis of dynamic interferometry caused by audio frequency tissue motion. This method provided relative stiffness map of in vivo tissue with a proper sample arm[97].

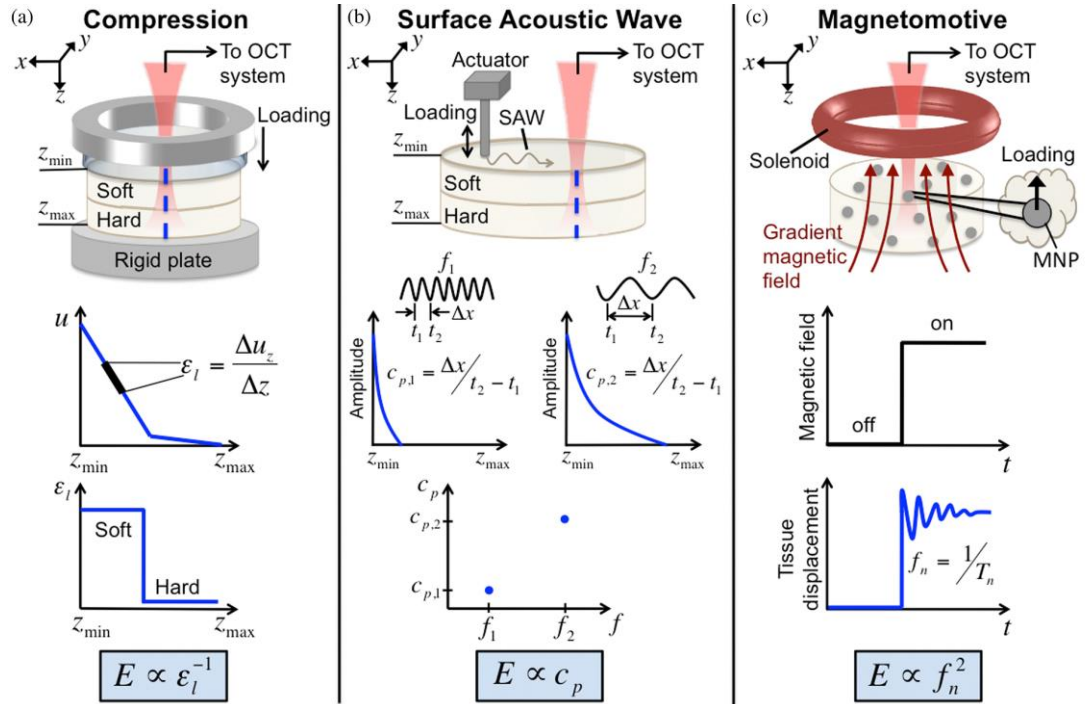


Figure 2-6 An illustration of loading schemes and elasticity estimation for three OCE techniques: Compression, SAW and magnetomotive[78]

Although promising, dynamic OCE relies on the vibration amplitude measurement, the calculation of elastic moduli maps must be based on the assumption of uniformly applied stress. The validity of this assumption throughout a heterogeneous sample has

recently been examined in some detail, along with the fidelity of elastograms in representing the true elastic properties [91]. For the samples with heterogeneous mechanical properties, for example containing inclusions, the stress distribution is no longer uniform, and the artifact in the strain elastogram caused by stress non-uniformity will significantly decrease the reliability of the quantitative estimation of elastic properties, or the detection of inclusion boundary. In compressional ultrasound elastography and magnetic resonance elastography, it has been proposed to overcome the issue of non-uniformly distribution of stress load by posing elastography as an inverse problem[98]. Related inverse methods have also been proposed in OCE[99, 100], but remain in the early stages of development.

Amongst all the OCE techniques, compression OCE has demonstrated highest resolution in the produced elastograms. But the innate absence of a measurement of local stress precludes the direct measurement of absolute values of elastic modulus has limited its suitability for certain applications, especially for those involving longitudinal studies. Furthermore, the feasibility of accurately detecting vibration amplitude in presence of lateral scatterer motion needs to be investigated further[101].

SAW-OCE

Transient OCE, on the other hand, lays emphasis on the propagation of dynamic mechanical waves. The surface wave methods can be classified as transient OCE methods. The common theoretical aspect of transient OCE is the mechanical wave propagation model, from which the inverse solution is derived, thus providing the physical parameters of the target specimen. As illustrated in Figure 2-6(b), a pulsed or burst load generates surface acoustic waves, which was then captured by OCT. The phase velocity of surface waves is analysed to inversely estimate the Young's modulus of different layers [102-104].

The main attractions of SAW OCE are: the potential to measure tissue mechanical properties at depths beyond the OCT imaging limit[104]; its suitability for non-contact (air-pressure or photo-thermal) loading on delicate tissues such as the cornea[105, 106] and its potential to directly quantify the Young's modulus in homogeneous tissues,

albeit with relatively low spatial resolution. An example of depth-resolved Young's modulus was plotted in the subcutaneous fat below human dermis is shown in Figure 2-7. The mechanical contrast was detected to the depth of 4mm, beyond the corresponding OCT image.

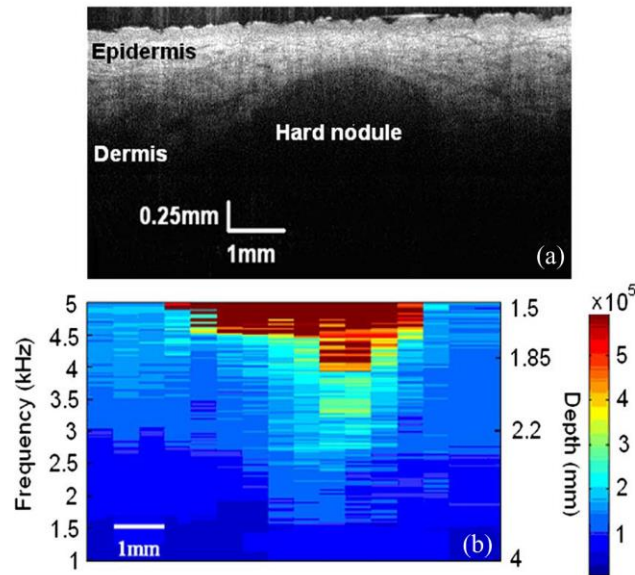


Figure 2-7 OCT image of a human forearm skin with a hard nodule and the corresponding SAW-OCE elastogram[104]

SAW OCE may ultimately be most useful for those applications requiring an absolute measurement of Young's modulus when tissue heterogeneity is not an issue. One of the most promising applications may be to the cornea[105], however, many of the potential difficulties and key assumptions mentioned above have yet to be investigated.

A drawback of SAW OCE is the order of magnitude lower lateral resolution ($\sim 500 \mu\text{m}$) in comparison to several techniques that achieve the OCT lateral resolution ($\sim 10 \mu\text{m}$). This limitation is imposed by the relatively long wavelength ($>10 \text{ mm}$), which sets the minimum propagation distance necessary to detect the time delay and dispersion of the surface acoustic waves. A further limitation is that the minimum depth probed is determined by the maximum detectable frequency.

Magnetomotive OCE

Magnetomotive OCE (MM-OCE) employs magnetic nanoparticles (MNPs) distributed in the tissue and actuated using an external magnetic field to produce localized, nanometre-scale tissue displacements. To determine the Young's modulus, the tissue can be modelled as an under-damped harmonic oscillator and its dynamic response, induced by oscillating MNPs, detected with phase-sensitive OCT[107]. As the MNPs contribute negligible inertia compared with the tissue, the measured frequency response can be related directly to the Young's modulus. The schematic drawing of an MM-OCE system is shown in Figure 2-6(c).

An advantage of MM-OCE over other techniques is the ability to perform measurements in small samples, as the localized tissue loading avoids the geometrical constraints of external loading. Additionally, the low force applied in MM-OCE makes it suited to the measurement of very soft tissues that are unsuited to measurement by other OCE techniques. This is partially offset by the very small displacements that can be induced and the challenge of measuring them with high dynamic range. In addition, the requirements to disperse MNPs at relatively high concentrations throughout the tissue and to achieve a high magnetic field gradient in the tissue present challenges, particularly to *in vivo* applications. As alluded to above, it remains to be seen if MM-OCE can provide image contrast between different tissues and disease states. To date, only point measurements have been presented, but MM-OCE imaging should be feasible.

2.7. Conclusions

Although different imaging and elastography techniques are available now, very limited research have been taken place in dermatology and ophthalmology applications to study the microstructure with mechanical property contrast *in vivo*. The most direct reason is a lack of ideal technique to provide high resolution depth-resolved quantitative elasticity mapping of the layered structure of tissue. It would be of great significance to have the ability to monitor changes of mechanical properties in skin or cornea, providing clinicians with relevant data about the pathological alterations.

Compared with other imaging techniques, OCT has great advantages of high resolution structural imaging, with low cost, portable nature and a relatively acceptable imaging depth. It is also a non-contact method applicable in various clinical environments. Based on OCT technique, OCE has become a hot topic in the past decade, while dynamic OCE is considered to be the most promising technique to provide quantitative elastography results.

Taking the advantages of SW-OCE, this dissertation is devoted to develop an imaging tool to study the biomechanics with high resolution of corneal or skin structural image combined with quantitative elastography mapping of shear modulus. The developed methodology enabled the quantification of biomechanical properties of the soft tissue and holds promise to become a much used clinical tool in the future.

3. TRANSIENT MECHANICAL WAVES THEORY AND MODELLING

3.1. Introduction

Mechanical waves have been successfully used in a wide variety of seismology and industrial applications for geological prospecting[108, 109] or measuring the mechanical property of engineering structures[110]. In modern medical developments, transient mechanical waves have attracted increasing attention including quantitative elastography[111], mechanical properties estimation[112], and angiography status diagnosis[113].

The mechanical wave propagation is a problem of high complexity. The behaviour of mechanical waves highly depends on the carrier, e.g. the mechanical properties, the geometry and boundary conditions. Mechanical waves in biomedical application are much more complex than industrial applications, given that the tissue is a visco-elastic media with complicated boundary conditions e.g. blood vessels, muscle and inner tissue. It is an essential work to recognize the wave mode and further explore the corresponding physical theory which to be used in the application.

In this chapter:

- * Mechanical wave propagation behaviour in biological tissue is reviewed.

With this theoretical basis, the characteristics of common transient waves used in biomedical tissue were studied, including longitudinal wave, shear wave, surface acoustic wave and Lamb wave. The comprehensive understanding of the characterizations including velocity, energy distribution, geometric spreading and dispersion serves as a theoretical basis and optimization guideline for developing a transient wave elastography system.

- * Finite element method (FEM) is utilized to simulate the generation and propagation of transient mechanical waves in biological tissue

Based on the numerical models and finite element methods, the generation and propagation of transient mechanical waves are simulated for a variety of stimulation methods, including contact mechanical stimulation, ultrasonically induced pulse waves, and pulsed laser stimulation. The simulation results works as a feasibility test for transient wave elastography in micro-scale tissue, and provide a better understanding of transient mechanical waves, in order to facilitate the work in subsequent chapters.

3.2. Propagation of mechanical waves

To obtain wave equations of mechanical waves in solid material, it is useful to suppose a particle in isotropic material and analyse the stress-strain relationship. In three dimensional Cartesian coordinate system, the equations of motion of this particle are given according to Newton second law and Hooke's law can be derived into the form below, using ξ , η and ζ to denote displacements of particle along x , y (lateral) and z (depth), respectively:

$$\left. \begin{aligned} \rho \frac{\partial^2 \xi}{\partial t^2} &= (\lambda + \mu) \frac{\partial \Delta}{\partial x} + \mu \nabla^2 \xi \\ \rho \frac{\partial^2 \eta}{\partial t^2} &= (\lambda + \mu) \frac{\partial \Delta}{\partial y} + \mu \nabla^2 \eta \\ \rho \frac{\partial^2 \zeta}{\partial t^2} &= (\lambda + \mu) \frac{\partial \Delta}{\partial z} + \mu \nabla^2 \zeta \end{aligned} \right\} \quad [3.1]$$

Where ∇^2 and Δ are the Laplacian and gradient form $\nabla^2 = \frac{\partial^2}{\partial x^2} + \frac{\partial^2}{\partial y^2} + \frac{\partial^2}{\partial z^2}$,

$\Delta = \frac{\partial \xi}{\partial x} + \frac{\partial \eta}{\partial y} + \frac{\partial \zeta}{\partial z}$. Medium material parameters are ρ - the mass density of the body,

λ and μ - Lamé constants.

We use $\mathbf{s} = \xi \mathbf{i} + \eta \mathbf{j} + \zeta \mathbf{k}$ as the particle displacement vector, and $\mathbf{v} = v_x \mathbf{i} + v_y \mathbf{j} + v_z \mathbf{k}$ as the particle velocity vector, Eq.[3.1] can be expressed in terms of particle displacement:

$$\rho \frac{\partial^2 \mathbf{s}}{\partial t^2} = (\lambda + 2\mu) \nabla (\nabla \cdot \mathbf{s}) - \mu \nabla \times (\nabla \times \mathbf{s}) \quad [3.2]$$

Since the velocity $\mathbf{v} = d\mathbf{s}/dt$, wave equation can also be given in terms of particle velocity:

$$\rho \frac{\partial^2 \mathbf{v}}{\partial t^2} = (\lambda + 2\mu) \nabla(\nabla \cdot \mathbf{v}) - \mu \nabla \times (\nabla \times \mathbf{v}) \quad [3.3]$$

Based on Helmholtz theorem, a vector field can be decomposed into the gradient of a scalar field and the curl of vector field with zero divergence, thus, \mathbf{v} in Eq.[3.3] can be substituted by $\mathbf{v} = \nabla \Phi + \nabla \times \Psi$ and $\nabla \cdot \Psi = 0$, where Φ is scalar potential and $\Psi = \Psi_x i + \Psi_y j + \Psi_z k$ is vector potential. Then separating scalar potential Φ from vector potential Ψ , two equations can be obtained from Eq.[3.3]:

$$\left. \begin{aligned} \rho \frac{\partial^2 \Phi}{\partial t^2} &= (\lambda + 2\mu) \nabla^2 \Phi \\ \rho \frac{\partial^2 \Psi}{\partial t^2} &= \mu \nabla^2 \Psi \end{aligned} \right\} \quad [3.4]$$

The two equations describe plane waves that propagate in a specific direction with Φ describing longitudinal waves while Ψ describing shear wave. Eq.[3.3] can also be expressed as:

$$\left. \begin{aligned} \nabla^2 \Phi &= \frac{1}{C_L^2} \frac{\partial^2 \Phi}{\partial t^2} \\ \nabla^2 \Psi &= \frac{1}{C_s^2} \frac{\partial^2 \Psi}{\partial t^2} \end{aligned} \right\} \quad [3.5]$$

By solving Eq.[3.4] and Eq.[3.5], the phase velocities of longitude wave (C_L) and shear wave (C_s) are given by:

$$C_L = \sqrt{(\lambda + 2\mu) / \rho} \quad , \quad C_s = \sqrt{\mu / \rho} \quad [3.6]$$

The particle motion and wave propagation pattern of longitudinal wave and shear wave are shown in [Figure 3-1](#)

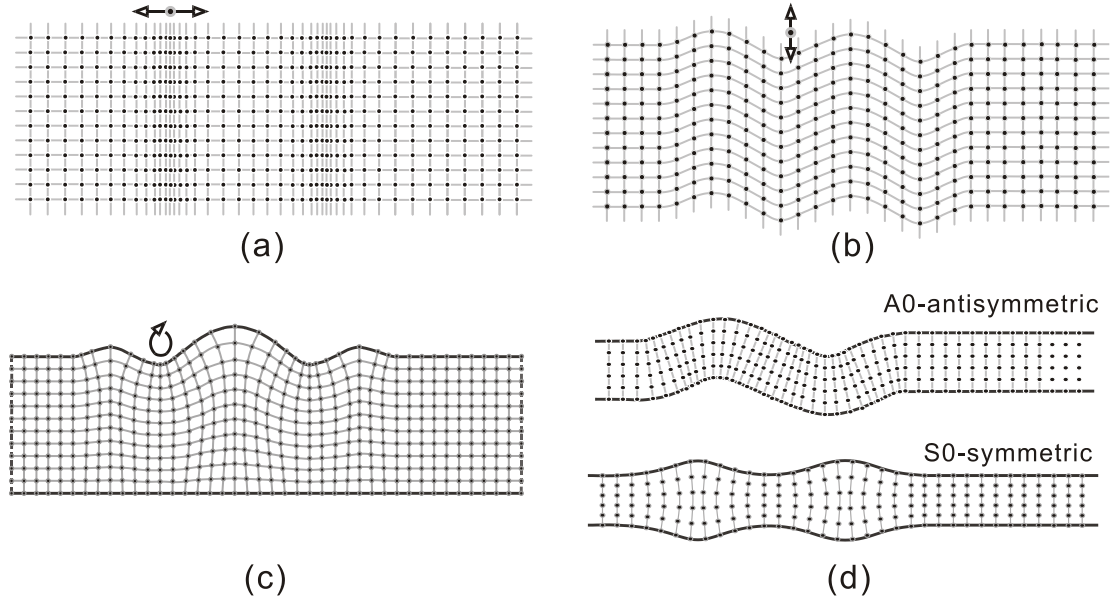


Figure 3-1 Particle motion patterns of different mechanical waves (a) longitudinal wave (b) shear wave (c) surface wave (d) fundamental modes of Lamb wave

Apart from longitudinal waves and shear waves known as bulk waves, there is another kind of wave that travels along the solid-vacuum interface (free surface). It is surface acoustic wave (SAW), which is also well known as Rayleigh wave. To obtain the potential function of SAW, a two dimensional plane containing x axis and z axis is taken into consideration for simplicity. Assuming the solution to equation set by:

$$\left. \begin{aligned} \Phi &= \Phi_a e^{-\alpha x} e^{j(\omega t - k_s z)} \\ \Psi &= \Psi_a e^{-\beta x} e^{j(\omega t - k_s z)} \end{aligned} \right\} \quad [3.7]$$

It has the same phase term as that of longitudinal wave and shear wave. However, an additional real exponential term accounts for the rapid attenuation of SAW along x axis (depth of the body), which is a main characterization of SAW. In addition, SAW can be viewed as the combination of shear energy and longitudinal energy that propagate on the material surface, which makes the particle move in an elliptical trajectory. Substituting Eq.[3.7] into Eq.[3.5], the relationship between attenuation coefficient and wave vector can be obtained:

$$\alpha^2 = k_R^2 - k_L^2, \quad \beta^2 = k_R^2 - k_S^2 \quad [3.8]$$

Where k_L , k_S , k_R are wave numbers of longitudinal wave, shear wave and SAW, respectively. With boundary conditions of zero stress at solid-vacuum interface, we can have that:

$$\left\{ \begin{array}{l} \left[\frac{\partial^2 \Phi}{\partial t^2} + 2C_s \left(\frac{\partial^2 \Psi}{\partial x \partial z} - \frac{\partial^2 \Phi}{\partial z^2} \right) \right]_{x=0} = 0 \\ \left[\frac{\partial^2 \Psi}{\partial z^2} - \frac{\partial^2 \Psi}{\partial x^2} + 2 \frac{\partial^2 \Phi}{\partial x \partial z} \right]_{x=0} = 0 \end{array} \right\} \quad [3.9]$$

Then we can get:

$$\left\{ \begin{array}{l} \omega^2 \left[1 - 2 \left(\frac{C_s}{C_R} \right)^2 \right] \Phi_A + 2j\beta\omega \frac{C_s^2}{C_R} \Psi_A = 0 \\ 2\omega \frac{\alpha}{C_R} \Phi_A - j \left(\beta^2 + \frac{\omega^2}{C_R^2} \right) \Psi_A = 0 \end{array} \right\} \quad [3.10]$$

The solution to the above Eq.[3.10] gives the Rayleigh equation:

$$\left[1 - 2 \left(\frac{C_s}{C_R} \right)^2 \right] \left(\beta^2 + \frac{\omega^2}{C_R^2} \right) + 4\alpha\beta \left(\frac{C_s}{C_R} \right)^2 = 0 \quad [3.11]$$

By defining the conventional forms of $g = C_R/C_S = k_S/k_R$, $q = C_S/C_L = k_L/k_S$ and combining Eq.[3.8], the above Rayleigh equation could be written as the following sextet equation:

$$g^6 - 8g^4 + 8(3 - 2q^2)g^2 + 16(q^2 - 1) = 0 \quad [3.12]$$

Given Poisson's ratio ν , Eq.[3.12] can be numerically solved to get

$$C_R = \sqrt{g} C_S \quad [3.13]$$

where g has an approximate expression of $g \approx (0.87 + 1.12\nu)/(1 + \nu)$. Over the allowed range of ν ($0 < \nu < 0.5$), the Rayleigh velocity C_R thus varies from $0.87C_S$ to $0.96C_S$, i.e. surface wave velocity is always slower than shear wave velocity.

Again, dealing with a boundary guided wave problem, Lamb wave is another case of sagittal wave that is usually considered to present in many biomedical applications. Lamb waves[114] are defined as the waves propagate along a thin plate, or similar structures like a thin wall pipe, and blood vessels. Mathematically, the problem for Lamb waves is rather more complicated than Rayleigh waves, the mathematical development is not stressed here, and rather we look at the simplest behaviour.

A fundamental difference between Rayleigh waves on a free surface and Lamb waves in a plate is that in the latter case the plate thickness b acts as a finite length scale. Since Lamb wavelength λ is of the order of the plate thickness b , the Lamb wave are dispersive in nature, and lamb waves of different modes and orders usually coexist. As shown in [Figure 3-1\(d\)](#), fundamental symmetric mode (S0) and anti-symmetric mode (A0) are illustrated, which are the most basic Lamb wave modes. In many areas of physics, for example, ultrasound non-destructive test (NDT), it is normal to describe the dispersion by the phase velocity (C_{ph}) curves as a function of $f \cdot b$ (product of frequency and medium thickness). Dispersion curves are measured over a frequency range and are compared with theoretical curves for carrying out mode identification in order to link the measurement to physical quantities.

3.3. Characterization of transient mechanical waves in biological tissue

3.3.1. Longitudinal wave

In longitudinal waves, the individual particles oscillate in a direction to the longitudinal axis of the solid, i.e. parallel to the direction of propagation of the acoustic wave as shown in Figure 3-1(a). As a kind of bulk wave, longitudinal wave travels within the body. Figure 3-2 shows a simulation result of the pulse stimulator generated longitudinal waves in a steel block. Longitudinal waves can be induced in solids, gas as well as liquids since the energy travels through the atomic structure by a series of compressions and expansion movements. The velocity of longitudinal waves (C_L) is given by the expression, which is widely used in industry [115]:

$$C_L = \sqrt{\frac{(\lambda + 2\mu)}{\rho}} \approx \sqrt{\frac{E(1-\nu)}{\rho(1+\nu)(1-2\nu)}} \quad [3.14]$$

where ρ is the density of the material and ν is the Poisson's ratio of the material.

Compare to shear wave and surface acoustic wave typical longitudinal waves have relatively higher speed (~5950m/s in steel, ~1480m/s in water and ~1550m/s in most of biological tissues [116]) and much broader frequency bandwidth (up to GHz in hard solid material and >100MHz in biological tissues [117]). The typical waveforms of longitudinal wave in steel and tissue mimicking agar phantom can be found in Figure 3-3(a,c), respectively. Their corresponded frequency spectrums are shown in Figure 3-3(b,d).

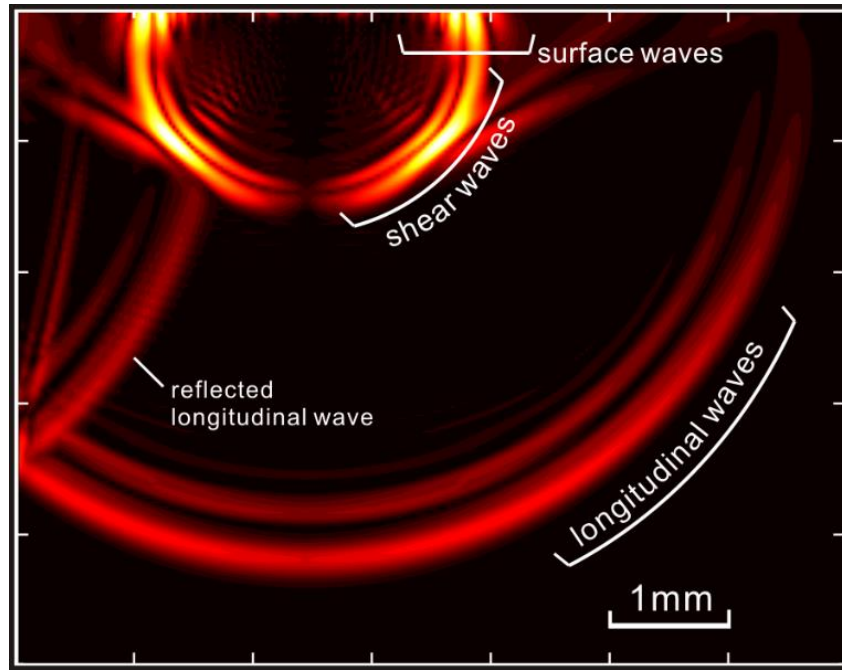


Figure 3-2 Numerical simulation results of pulse-stimulated mechanical waves.

Colour brightness indicates the displacement amplitude. Model based on a finite difference method with the second-order temporal and fourth-order spatial approximations[118]. Material of the simulated media is a steel block with longitudinal wave velocity 5940 m/s, shear wave velocity 3220 m/s, density 7800kg/m³. A pulse of 0.625μs is applied to the surface on 2.5mm from left edge. The time position of this wave field snapshot is 5μs after the pulse stimulation.

In Figure 3-3, the waveforms of typical longitudinal wave are displayed. Longitudinal waves in both metal material and tissue mimicking material are fast-travelling waves. As shown in this figure, the recorded waves contains a broad-band ultrasound frequency, and the localized wave velocity is also difficult to estimate.

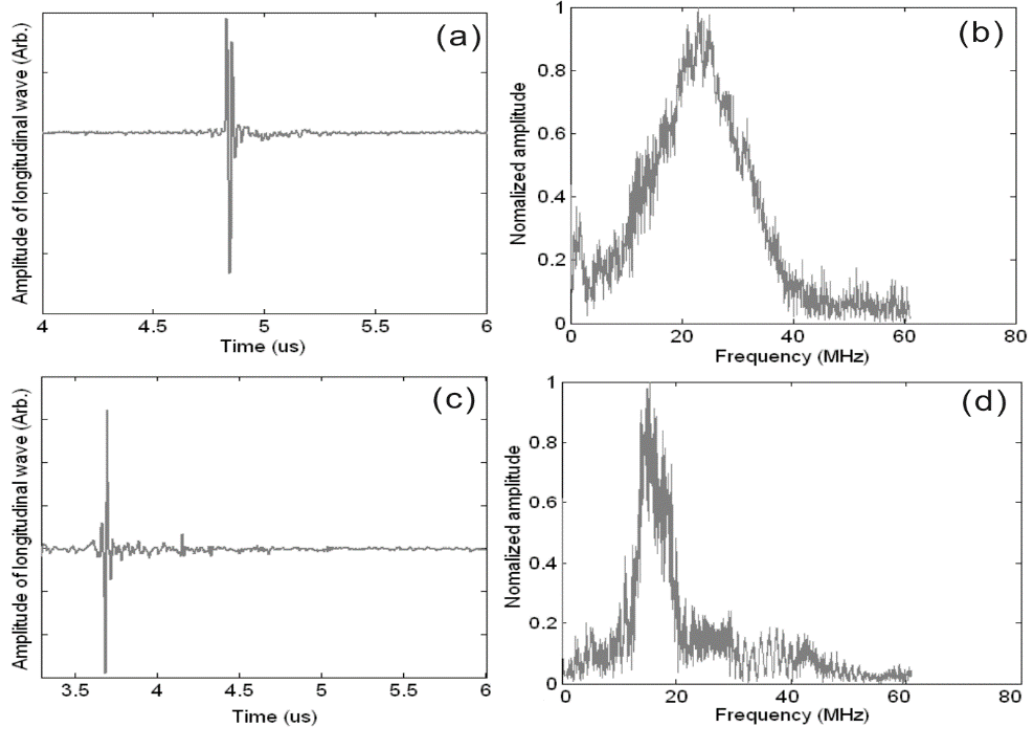


Figure 3-3 Typical longitudinal waveform and corresponded frequency spectrum of steel (a, b) and tissue mimicking agar phantom (c, d)

3.3.2. Shear wave

In elastic solids the other form of body wave is known as the shear wave, where particles oscillate in a direction perpendicular to the direction of propagation of the acoustic wave (Figure 3-1(b)). The shear wave is named because particles moves in a periodic manner as a consequence of a shear force, as shown in Figure 3-1(b). The numerical simulation of shear waves in a steel block can be found in Figure 3-2. Shear waves can only propagate effectively in solid materials and not in liquids or gases. The velocity of shear waves, C_s within a solid material and is roughly half the longitudinal wave velocity and is given by the expression [119, 120]:

$$C_s = \sqrt{\frac{\mu}{\rho}} = \sqrt{\frac{E}{2\rho(1+\nu)}} \quad [3.15]$$

Here ν stands for Poisson's ratio. The shear wave speed is slower than longitudinal waves (~2 times slower in hard solids and hundreds times slower in biological tissue)

and a little faster than surface waves (~ 1.1 times of surface wave speed), e.g. the shear wave speed in steel as $\sim 3240\text{m/s}$ in steel, $\sim 20\text{m/s}$ in muscle and $\sim 2\text{m/s}$ in liver. Shear waves generated by vibration has narrow frequency bandwidth, while the ones generated by pulse have wider frequency bandwidth (up to $\sim 6\text{MHz}$ in metal and $\sim 5\text{-}20\text{ kHz}$ in biology tissues [121]).

The shear wave is usually generated with a continuous wave (CW) stimulation, thus the frequency bandwidth would be very narrow which mainly represents the frequency of vibration source. On the other hand, if stimulated by a pulse source, the shear wave always couple with surface acoustic waves and have relatively broader frequency bandwidth.

3.3.3. Surface acoustic wave (SAW)

Most commonly used SAW is excited by impulse stimulation. An impulse SAW is normally bipolar, strong in amplitude, broadband in frequency, and propagates in the interface between a half-space and a rarefied medium. The best-known surface wave is called Rayleigh wave. On ideal homogeneous flat elastic solid the SAWs show no dispersion and travel at a constant velocity as described by Eq.[3.13]. SAW become dispersive if the material under test has elasticity properties that varies with depth. Thus, low frequency of SAW has a relatively long wavelength which can propagate deeper into the material, then represents the elasticity in substrate layer, while higher frequency waves have a much shorter wavelength represents the elasticity of upper layer. It is this characteristic which allows the use of Rayleigh waves for material characterization of thin layered materials as waves of different frequencies can be used for the characterization of different length scales [122, 123].

$$C_R = \sqrt{g} C_s \approx \frac{0.87 + 1.12\nu}{1 + \nu} \sqrt{\frac{E}{2\rho(1 + \nu)}} \quad [3.16]$$

Similar to shear wave, the speed of SAW is much slower than longitudinal waves and ~ 0.9 times of shear wave, e.g. the shear wave speed in steel as $\sim 3000\text{m/s}$ in steel.

SAWs have broad bandwidth of frequency (up to ~6MHz in metal and ~5-20 kHz in biology tissues) and different frequency components indicate the corresponding depth propagated into the sample surface.

The typical impulse response SAW waveforms in steel, and agar phantom, can be observed in Figure 3-4 (a and c). Figure 3-4 (b and d) shows the corresponding frequency response. SAW signals have strong amplitude and can propagate very far from the stimulator. However, SAWs attenuate rapidly along depth of the body. The depth that Rayleigh waves are propagating is approximated to around one wavelength of SAW. In addition, there is research reported about the CW source generated SAW [124, 125]. However, CW generated SAW have no dispersion behaviour and have very limited frequency response. It is not commonly used and has limited applications.

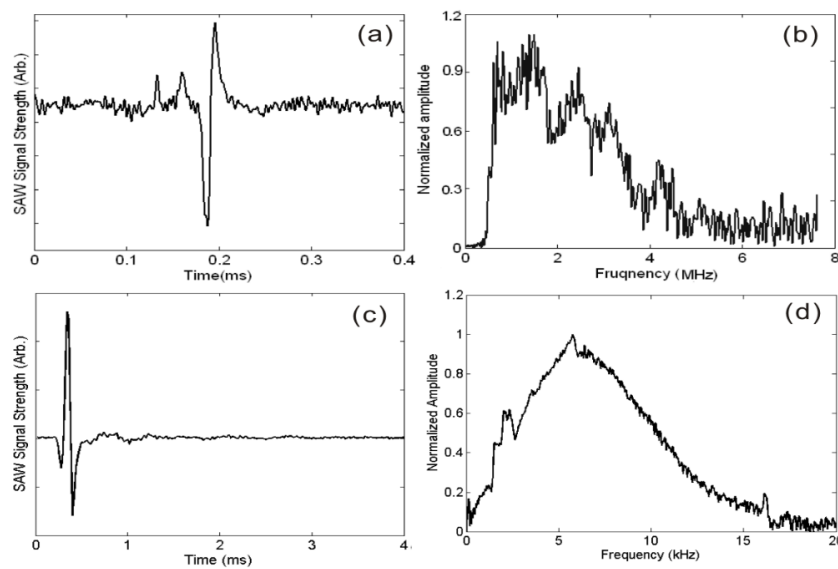


Figure 3-4 Typical surface waveform and corresponded frequency spectrum of steel (a, b) and tissue mimicking agar phantom (c, d)

3.3.4. Lamb wave

In biomedical application of Lamb waves, the waves are usually considered as low frequency (<2 kHz), and mainly contains A0 mode, because the Lamb waves are provided by acoustic radiation force in the thickness direction. Meaning that the approximation of only considering the fundamental A0 dispersion is effective[126].

The A0 mode dispersion equation of a thin elastic plate in vacuum can be approximated as an analytical formulation of phase velocity as a function of the angular frequency ω , thickness b , and transverse wave (shear wave) velocity of plate [127]:

$$C_{\text{ph(A0)}}(\omega) = \sqrt{\frac{\omega b C_s}{\sqrt{3}}} \quad [3.17]$$

The A0 mode Lamb wave dispersion equation is also approximated for plates immersed in liquid, with a correctional factor of $1/\sqrt{2}$ [126]:

$$C_{\text{ph(A0)}}(\omega) = \sqrt{\frac{\omega b C_s}{2\sqrt{3}}} \quad [3.18]$$

This fluid-loaded case of leaky Lamb wave is applied in many organs, e.g. cornea, skin layers, or arterial walls. This analytical dispersion equation is also validated by finite-difference simulations and in vitro experiments [128].

3.4. Simulation of transient waves in soft tissue

In this section the computational steps for the simulation of the transient wave elastography are described, and the main properties of the shear wave and surface wave propagation in heterogeneous media are discussed. Since the longitudinal waves velocity is not applicable for estimating elastic properties, the relevant study on longitudinal waves are not presented here. The simulated results of the wave fields induced by different methods are presented, and the feasibility of using the propagation of transient mechanical waves are predicted.

3.4.1. Finite element simulation

Although there had been a good amount of work using transient wave, especially using shear waves for biological tissue elastography, to detect transient wave propagation with OCT is still a new research field. No report about the transient wave behaviour within OCT imaging range has been presented so far. This makes the simulation study a critical part in the development of transient wave OCE. There are multiple benefits to expect from simulation:

- 1) Feasibility test of practical experiment to induce detectable transient wave.
- 2) Observe the wave mode generated from different stimulation methods.
- 3) Optimize wave generation scheme to achieve effective shear wave launching
- 4) Provide guidance for experiment arrangements.

The finite element method (FEM), also known as finite element analysis (FEA) for its practical application, is a numerical method to obtain approximate solutions by solving partial differential equations (PDE) and varieties of integral equations. For the steady state solutions, approaches are made by solving the differential equations completely, while other techniques involving approximations of ordinary differential equations

(ODE) could be utilized to solve dynamic domain solutions.

ABAQUS is a powerful interactive environment for modelling and solving all kinds of scientific and engineering problems. As an FEA software, the solution of the problems is based on partial differential equations (PDEs) from the basis of the laws of science, which are the foundation for modelling a wide range of scientific and engineering phenomena. In this study, ABAQUS provided built-in physics interfaces and the advanced support for material properties and made it possible to build transient mechanical wave propagation models by defining the relevant physical quantities – such as material properties, loads, constraints, and energy sources. ABAQUS then compiles a set of equations representing the entire model. The general modelling procedures are described below.

Problem definition

Model definition is the first stage of the simulation preparations. The analysis field of the real-world structure is imported as a model to the software, after steps of simplification such as eliminating duplicates and symmetric modelling. The most efficient simplification is the decrease in the dimensions of the model, accompanied by the reduction of the degree of freedom. Then the figure and dimensions, with all degree of freedom considered should be fully defined in the modelling procedure.

The parameters, including the relative properties of the model material and the information about the loads and restrictions are also vital to the simulation result. Most of the parameters are set as the boundary conditions and the initial conditions.

Meshing is the procedure to divide the model into finite elements and generate the PDEs for the model. The mesh would define the nodes and the degrees of freedom for each node. Acting as the critical step of discretization, the mesh is a limiting factor of the accuracy of solving, hence a refined mesh is necessary to obtain satisfactory resolution of the simulation results in areas of specific interest.

Solution

Before running the calculation, the solution type is must be defined, depending on the application area, there are time-dependent, eigenfrequency and stationary analysis etc. This will determine the solver that will be used in PDE-based solving. Solution control is required to be defined, such as the solver manager parameters, and non-linear settings. As the solution progressed, the convergence information of the variables that are solved is monitored. For a reliable solution, the rate of change of the variables will decrease rapidly. That means the solution has converged to a stable solution.

Post-processing and visualization

ABAQUS CAE provides numerous of visualization and post processing tools for analysing the results obtained from the model solver. There are a variety of formats to plot the figure, such as the contour plots, isosurface plots, streamline plots and surface plots. These plot types are available on pathline and cross-sections. With the expression post-process, user-defined variables, standard variables and logical or mathematical functions could be combined to generate the outcome.

3.4.2. Simulation of mechanically induced waves

Model definition

A finite element model is created in ABAQUS CAE to simulate the transient mechanical waves generated by direct contact mechanical stimulation on the surface of a phantom. Some details of this model is given in Figure 3-5. For simplicity, the model is based on a symmetrical 2-dimensional configuration, since the mechanical waves generated by a linear shaped source are plane waves. In [Figure 3-5 \(c\)](#) another model with a cylindrical inclusion is shown, with the inclusion highlighted, at the centre of the region of interest.

The transient wave source is a blade-shape shaker head, and modeled as a rigid body. The initial distance between the blade and phantom is set to 0.2mm, the temporal profile of shaker head displacement is defined accordingly, as shown in Figure 3-6,

two types of stimulation are defined, i.e. a pulse stimulation with duration of 0.2 ms, and 4 cycles tone-burst at 5 kHz.

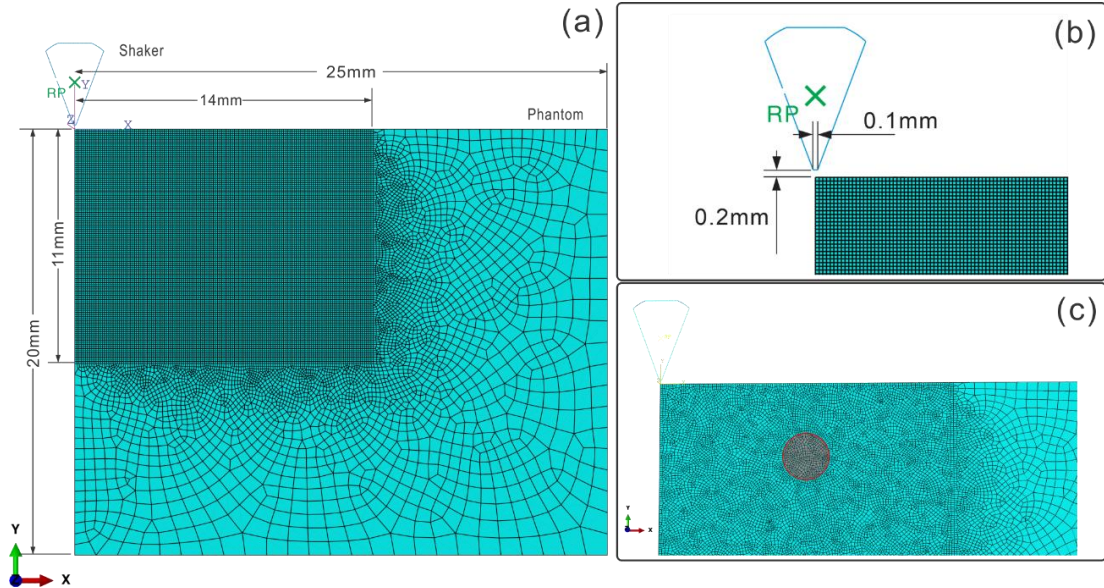


Figure 3-5 Model geometries and mesh for contact generation of transient waves

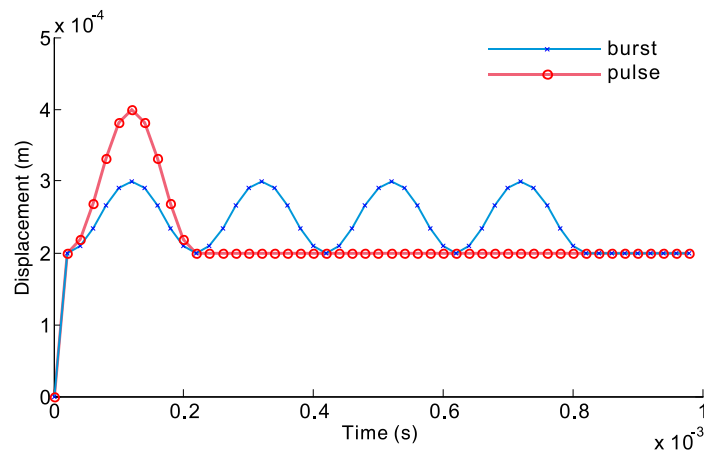


Figure 3-6 Shaker head displacement profile in simulation model

The mesh of a FEA model is critical to an efficient and accurate simulation. For the balance between field output accuracy and computational time, the New Mark Schema is applied to determine the element size and time increment in the simulation, according to the expected wavelength and frequency of the mechanical waves:

$$\Delta t = \frac{1}{10f_{\max}} \quad , \quad l_e = \frac{\lambda_{\min}}{10} \quad [3.19]$$

where Δt is the integration time and l_e is the element length. The f_{\max} refers to the highest frequency and λ_{\min} refers to the shortest wavelength. Based on the aforementioned principle, the maximum time increment is defined as 50 us, and element length in the region of interest is 50 um. The outer region in this model is used to avoid the reflected waves from model boundary, thus the mesh in this region is relatively coarser than the region closer to the source.

Symmetrical boundary condition is defined on the left boundary of phantom. The bottom and right hand side boundary is considered as fixed. A total simulation time of 2 ms was defined, as at the end of 2ms simulation time the mechanical waves have passed the region of interest, according to the model dimensions and wave velocity.

As the wave propagation analysis is clearly a high-speed, dynamic problem, the ABAQUS/Explicit procedure is chosen. In the explicit procedure, ABAQUS determines the solution without iterating by explicitly advancing the kinematic state from previous increment, so that the stable time increment is small, and computationally cost-effective.

The displacement field outputs inside the phantom region are requested for every 50 us time increment. A python script is used to read the field output frames of the simulation results and convert to element node data records. Then the data is imported to MATLAB for visualization and analysis.

Results

The displacement amplitude (U), displacement vector in X axis ($U1$) and Y axis ($U2$) are exported in the field output. To simulate the displacement that is captured by PhS-OCT, only the Y-axis components were processed and visualized, as shown in Figure 3-7.

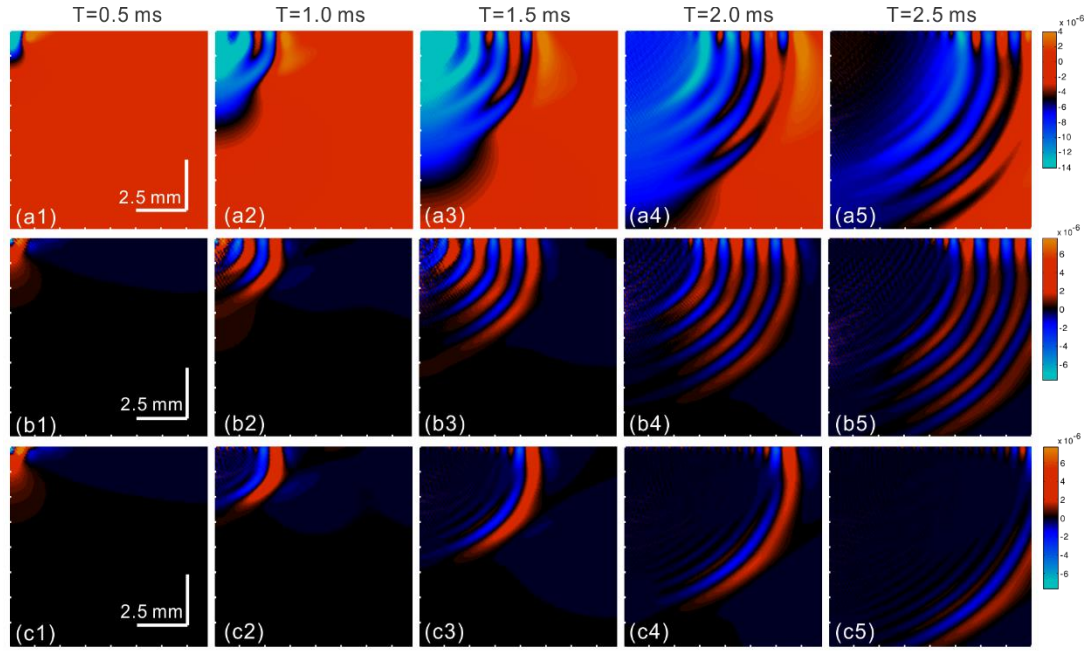


Figure 3-7 Simulation results of contact induced shear waves (a1-a5, b1-b5) burst excitation; (c1-c5) pulse excitation.

In Figure 3-7(a1-a5), the Y-axis (axial direction) displacement field snapshots at five evenly-spaced time points were visualized. The displacement at each sampling point (grid size 50 μm) is used for color coding the wave image, with a positive value indicating the motion upwards, to the “OCT imaging probe”. Since the relaxation of the sample takes more time than the simulated period, the bulk sample is “pushed” away from the shaker tip: the accumulated displacement shows a negative value after the shaking stimulation. In (a1-a5) images, the color map baseline is shifted, using red to stand for zero displacement, using middle tone to fit the wave displacement range for a clearer visualization of the wave field.

In these wave propagation snapshots, the shear wave mode can be clearly observed, with the main energy distributed around the 45 degree angled line, which retains good correspondence to the theoretical model of the waves generated by a pulse stimulator on an infinite half-space solid[129]. In comparison with the simulated waves on a metal plate as shown in Figure 3-2, the compressional waves (P-waves) are not observed because the P-waves are many times faster (~ 1560 m/s) than the shear wave or surface waves in soft-tissue mimicking media.

Since the displacement detected by PhS-OCT is a temporal differential result between adjacent acquisitions, the shear wave imaging results provided by PhS-OCT will be the differential map of wave field snapshots (See Chapter 4.2 Phase sensitive OCT). The differential results obtained from adjacent wave field frames are given in Figure 3-7(b1-b5), which presented an even clearer visualization of the wave fronts of shear waves in the cross-section. The differential displacement map of a 0.2 ms duration pulse stimulation is also illustrated in Figure 3-7(c1-c5). In this image some trace of shorter-wavelength, high frequency components can be observed close to the surface, with an active depth of about one wavelength. This is confirmed by the surface acoustic wave theory about the penetration depth of specific wavelength.

As a homogenous sample, the shear wave velocity was calculated to be 4.87 m/s, indicating a good agreement with the input Young's modulus according to Eq.[3.15]

The simulated wave field displacement data for a further simulation with a cylindrical inclusion are displayed in Figure 3-8. Similar to the homogenous phantom model, the displacement snapshots are the differential results, as seen in Figure 3-8(b1-b4), in comparison with the same time instance in homogenous phantom model as Figure 3-8(a1-a4). The dashed line in the wave snapshots are the indication of the boundary of the cylindrical inclusion. In Figure 3-8(b2), the first wave front of the shear waves has reached the inclusion. As a consequence of the change in shear wave velocity in the inclusion, the wave front shape has distorted, since the waves inside the inclusion travel faster than the waves outside in the background media. (b3) and (b4) further illustrated this phenomenon, showing the waves that passed through the inclusion propagated further than the waves that were not affected by the inclusion.

Diffraction can also be observed in this simulation result, as the inclusion can be considered as an obstacle. Some of the shear waves has changed direction of propagation, and forming interfere with the waves that didn't pass through the inclusion. Since the wave velocity difference between the inclusion and the background is small, the reflection waves present an amplitude that is too small to be visually observed on these images. The reflected waves can also interfere with the on-ward propagating waves. However, the diffraction and interference of shear waves will

not alter local wave velocity. After proper processing, localized shear wave velocity can still be obtained, and used to estimate localized mechanical property.

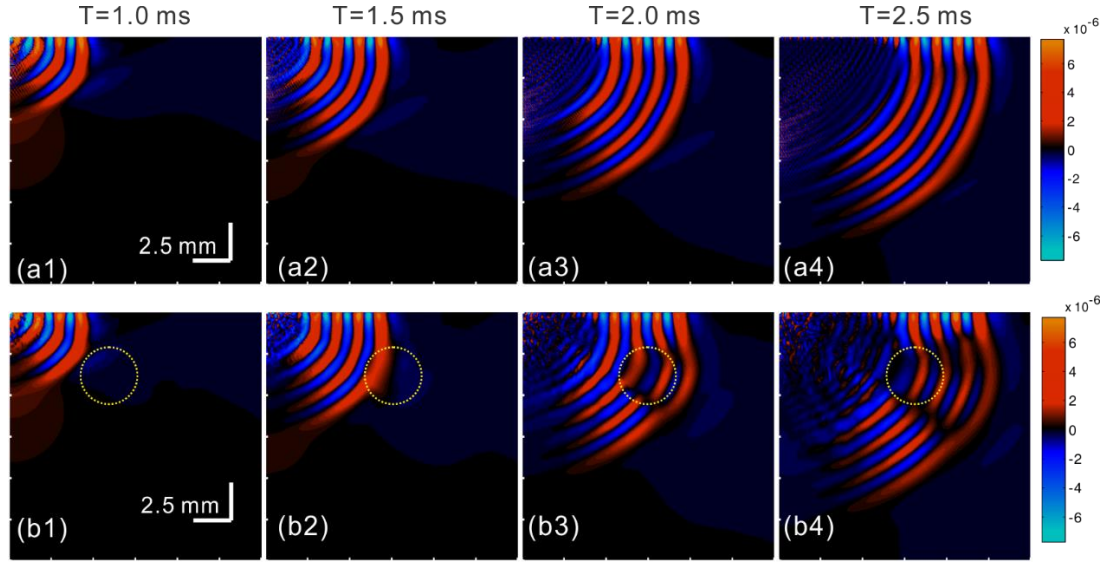


Figure 3-8 Simulated wave snapshots on a phantom with embedded inclusion

Again, using the time-of-flight method, the wave velocity inside the inclusion are estimated as 7.01m/s, and the velocity of waves outside the inclusion in the background phantom are 4.92m/s. This is also in good agreement with the input parameters of 150 kPa and 75 kPa of Young's modulus in the inclusion and background phantom, respectively.

3.4.3. Simulation of pulsed laser induced transient waves

Model definition

The laser pulse is assumed as a laser pulse with Gaussian profile. The spatial intensity distribution at the beam cross-section is described as:

$$F(r) = F_0 \exp\left(-\frac{r^2}{r_0^2}\right) \quad [3.20]$$

where F_0 is the laser intensity at laser spot centre, r is the radius coordinate, r_0 is the

radius of laser pulse. And the temporal intensity profile form a pulsed laser is described as[130]:

$$G(t) = (t/t_0) \exp(-t/t_0) \quad [3.21]$$

where t is the exposure time and t_0 is the pulse rise time. The laser pulse has different effects on optically dense medium and optically thinner medium. For example, metals are generally optically dense thus the laser pulse can hardly go through the metallic surface. During the short pulse duration, the laser energy can just be absorbed by a depth strictly confined to the surface. The thickness of the absorption area is typically in the order of 5~10nm. In other words, the laser affected area in metallic samples is very thin and this type of laser effect is called the heat flux. An expression used to describe the heat flux irradiance is as below:

$$I_d = I_0 \cdot F(r) \cdot G(t) \quad [3.22]$$

where I_0 refers to the central irradiance of laser pulse. In the steel simulation, Eq.[3.22] is used. However, the case is not the same with soft biomaterials, where the laser pulse will penetrate a significant depth into the tissue. Accordingly, the laser affected area is extended into the materials interior and this kind of mechanism is defined as the heat generation. In this case, the irradiance can be described as follows:

$$I_d = I_0 \cdot \mu_a \cdot F(r) \cdot G(t) \cdot \exp(-\mu_a Z) \quad [3.23]$$

where μ_a is the absorption coefficient and Z is the coordinate describes the depth below surface. Eq.[3.22] is used in steel simulation while Eq.[3.23] is suitable in agar simulation. The dimensions of the model and the setup of laser radiation input is presented in [Figure 3-10](#).

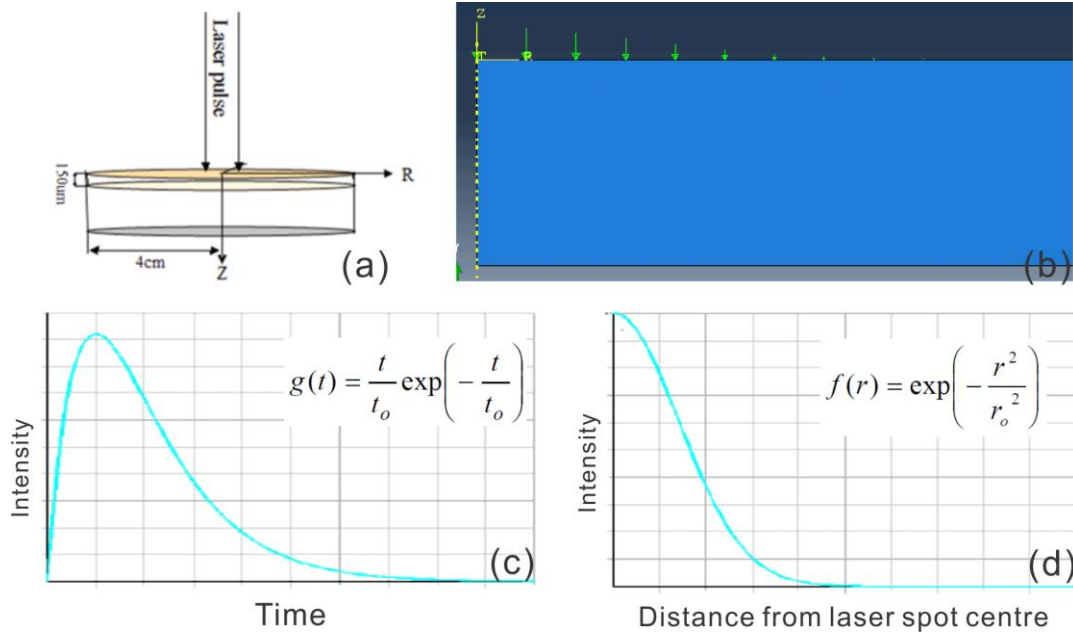


Figure 3-9 Simulation setup of pulsed laser generated mechanical waves on single layer and two layer medal model

The set-up in thermal analysis is kept the same with the available laser pulse source in the lab where the applied laser energy is ~3 mJ, the laser pulse rise time is 6 ns. The thermal and mechanical parameters of steel and tissue mimicking agar phantoms with concentrations of 2% are listed in Table 3-1.

Table 3-1 Input parameters of pulsed laser induced mechanical wave model

Input Parameter	Steel	Copper	agar phantom, 2%
Young's Modulus (kPa)	6.9×10^7	1.21×10^7	180
Poisson's Ratio	0.34	0.34	0.47
Density (gmm^{-3})	2.77×10^{-3}	8.96×10^{-3}	1.04×10^{-3}
Thermal Expansion coefficient (K^{-1})	2.31×10^{-5}	1.65×10^{-5}	3.0×10^{-4}
Specific Heat ($\text{Jg}^{-1}\text{K}^{-1}$)	0.875	0.386	3.590
Thermal Conductivity ($\text{Wmm}^{-1}\text{K}^{-1}$)	0.394	0.401	2.4×10^{-4}

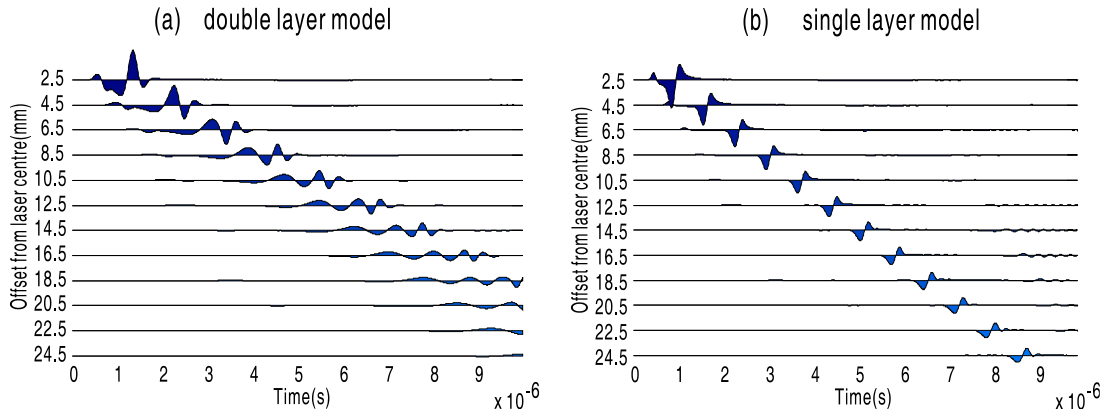


Figure 3-11 Surface wave results from single layer and two layer FEA models

The dispersion analysis is performed for each wave group. Phase velocity in the range of 0.5 GHz to 5.5GHz were calculated by phase delay, between wave forms acquired on adjacent offsets. Then the mean and standard deviation of phase velocity are shown in Figure 3-12.

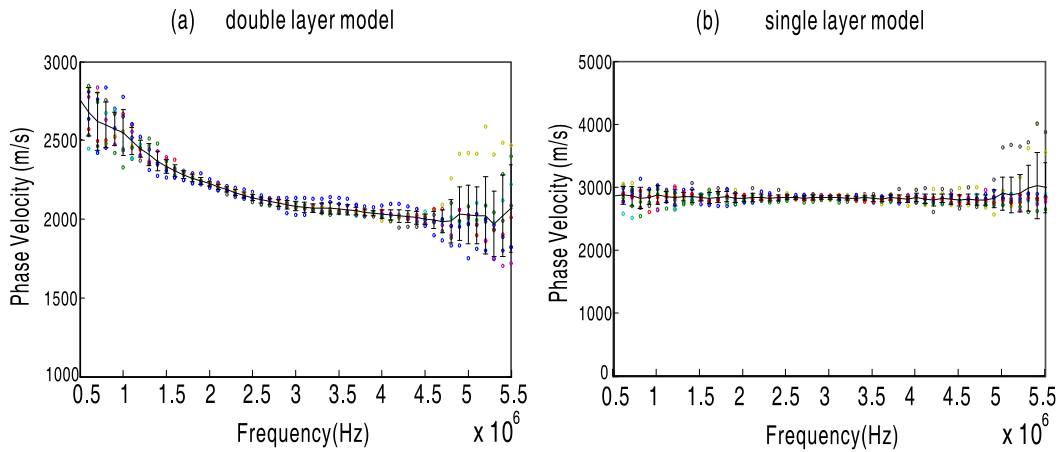


Figure 3-12 Phase velocity result of surface waves simulated in single layer and two layer FEA models.

From the above phase velocity results, the dispersion of surface acoustic waves has been demonstrated for the two-layered model with different mechanical property. The wave velocity results of the low-frequency waves (below 1 MHz) matched the Young's modulus value (2721 m/s, 69 GPa), and the high frequency components tends to present a surface wave velocity (1929 m/s) that indicates the Young's Modulus of superficial layer(copper, 12.1 GPa).

The simulation results of pulsed laser generated surface acoustic waves are shown in Figure 3-13(a). The sample points are distributed with 0.5 mm interval, starting from 2 mm distance from the laser source center, to 11 mm distance. The waves are propagating with a non-dispersion speed before 4 mm, and an increase in the group velocity can be observed on the wave traces from 4.5 mm to 8 mm (indicated by the slope on the dashed lines which indicates the wave fronts, as higher slope value in this graph representing a higher group velocity.)

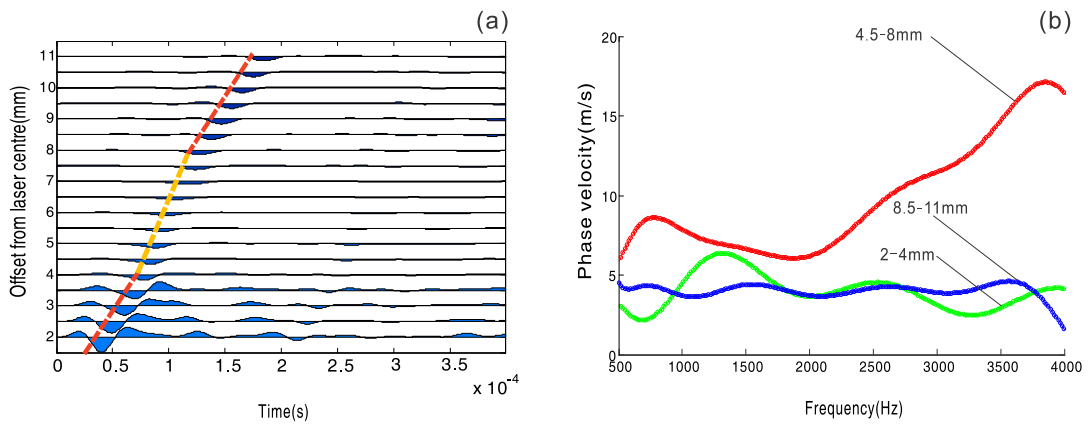


Figure 3-13 Surface acoustic wave traces on the surface of agar phantom with embedded inclusion

The wave traces are grouped into three, according to its relative location to the embedded hard inclusion: 2-4 mm is before the inclusion, 4.5-8 mm on the inclusion and 8.5-11 mm after the inclusion. The averaged phase velocity dispersion curves are shown in Figure 3-13(b). The blue and green curves indicates no dispersion, since in those areas the media is homogenous, while as the red curve indicates, in the two-layer region, high frequency travels faster than low frequencies. The wave velocity before and after the inclusion present an average wave velocity of 4.8 m/s, with relatively low variations, which indicates non-dispersion behavior. For the surface waves on the inclusion, the low frequency components remains a similar, low phase velocity value, the high frequency components presents a higher phase velocity value (16.4 m/s, 3.5-4 kHz), since the high frequency component phase velocity is dominated by the Young's modulus of shallower structures.

3.5. Conclusions

Transient elastography, which mostly deals with shear wave, surface wave and Lamb wave can achieve many applications in biomedical area. As the different nature of these three kinds of waves, combining them with different kinds of technologies has the potential to be an invaluable measurement and diagnostic tool in many areas, especially in imaging and the mechanical properties estimations.

The use of shear wave, surface wave and Lamb wave in biomedical area is still relatively new, therefore, it is essential that we can understand them fully, use them in the correct way and develop their applications further. In the first part of this chapter, the behaviour of transient waves were studied. Bulk shear waves are considered as the most promising wave mode to provide localized elastic property.

Following the above conclusion, finite element models were designed and simulations are performed to study the shear wave behaviour in biological tissue. Contact mechanical generation and pulsed laser induced transient waves are simulated, and the wave propagation behaviour were observed, demonstrating the ability of shear waves for showing localized shear modulus. Furthermore, the dispersion behaviour of laser induced surface wave is also studied. The conclusion can be made that even though the transient waves presents Rayleigh wave mode, the high frequency components can still be considered as shear waves, since the wavelength of high frequency waves are small, and their velocity is dominated by local mechanical property.

The above observations and conclusions has led this study to the next objective, which is the design of shear wave imaging technique for capturing the transient wave propagation with OCT.

4. SHEAR WAVE IMAGING TECHNIQUE USING PHS-OCT

4.1. Introduction

To achieve the requirements of the OCT system for capturing shear wave propagation with the goal of reconstructing OCE images, the design of OCT system, data acquisition and optimization needs to be considered. Although there are many commercially available OCT systems, the customizability, raw data accessibility and system performance are insufficient for OCT shear wave imaging. Based on the existing laboratory prototype OCT system, several critical parts of the OCT system need to be re-considered to meet the requirements of SWI.

OCT-SWI is based on Phase-sensitive ability, which is a relatively new feature, with certain problems to overcome. The data acquisition protocol and data optimizing is a critical topic in designing the SWI OCT system, to record and recover ideal dynamic wave propagation data.

In This Chapter

- * A general introduction of the system specification and performance is presented.

- * The design and assembly of several critical parts, that are relevant to OCT-SWI, is presented.

The relevant OCT parts includes laser source, sample arm, reference arm, spectrometer and processor. The considerations in the design are illustrated, and the specifications of essential parts are introduced. The comprehensive explanation of the working principles of PhS-OCT system is given, for a better understanding of the following section of data processing

- * OCT data processing: structural image and motion detection

The necessary pre-processing of OCT raw spectrum data are presented, and the theoretical background for OCT structural imaging and Doppler phase motion detection.

- * OCT –SWI data optimization

In common with other SWI techniques, OCT-SWI data is contaminated with noise and artefacts. The discovery of the surface ripple artefacts are demonstrated, and the theory of formation, together with a compensation algorithm are given.

A technique that uses coded excitation for elevating the SWI SNR is also presented in detail.

4.2. Phase sensitive OCT

In this section the general function and performance of a Phase-Sensitive OCT (PhS-OCT) system are briefly presented, to introduce the tool that is used later to study the transient mechanical wave. Then the design and construction of this PhS-OCT system that based on a Spectral Domain OCT system is presented, and the procedures for obtaining OCT structural image and phase detection are discussed, as the fundamental for shear wave imaging (SWI) technique.

4.2.1. System specifications of Spectral Domain OCT system

In year 2012, a Fourier Domain/ Spectral Domain Optical Coherence Tomography (SD-OCT) system was built in University of Dundee, for the purpose of high-resolution biological tissue tomography imaging, and development of multiple modality elastography technique in combination with OCT. This work is equally contributed by the joint effort with another PhD student, Guangying Guan, based on an improved design inspired by the OCT systems built in Biophotonics And Imaging Laboratory (BAIL), University of Washington. Optical contrast tissue structural imaging is the fundamental function of this SD-OCT system, and the designed system specifications are listed in Table 4-1.

There are many factors that determines the performance of an actual OCT system which could present disparity to designed values, for example, the imperfection of optical components and the accuracy of calibration. Moreover, as the OCT system is designed for multiple purposes, some components, especially the imaging probe parts, were designed to be interchangeable, thus the actual performance are dependent on the imaging probe.

Table 4-1 Specifications of the SD-OCT system (f – Objective lens focal length)

		Designed value	Actual performance	
Light source	Central wavelength	1310 nm	1309 nm	
	Bandwidth (FWHM)	~200 nm	~160 nm	
Imaging performance	Depth of field (2 x Rayleigh length)	Up to 2.5mm	172 μ m	(f = 18 mm)
			480 μ m	(f = 30 mm)
			1334 μ m	(f = 50 mm)
	Lateral resolution	Up to 5 μ m	5.1 μ m	(f = 18 mm)
			8.5 μ m	(f = 30 mm)
			14.2 μ m	(f = 50 mm)
	Axial resolution	Up to 8 μ m	9~15 μ m	
Scanning	Camera exposure rate	Up to 92kHz	47 kHz	
	Max scan angle	$\pm 20^\circ$	$\pm 12.5^\circ$	Small beam
	Frame rate	70Hz	0.1~1 kHz	Angle dependent

4.2.2. Hardware design of an SD-OCT system

A schematic drawing of the OCT system is displayed in Figure 4-1. Briefly, the OCT system is based on low-coherence light and Michelson-interferometer. Two reflected laser beams from a stationary mirror and imaging target forms interferometry in a fiber-optic coupler. The optical reflectance in imaging target is depth-coded by the wavenumber domain interferogram frequency. Interferogram is acquired by linear array charge-coupled device (CCD), and the depth-resolved information is then recovered by Fast Fourier Transform in a micro-computer based processor, comparable to the ultrasound A-scan. The 2-dimensional cross-sectional image or 3-dimensional volumetric images can then be acquired by one, or a pair of precisely synchronized Galvanometer scanning mirrors.

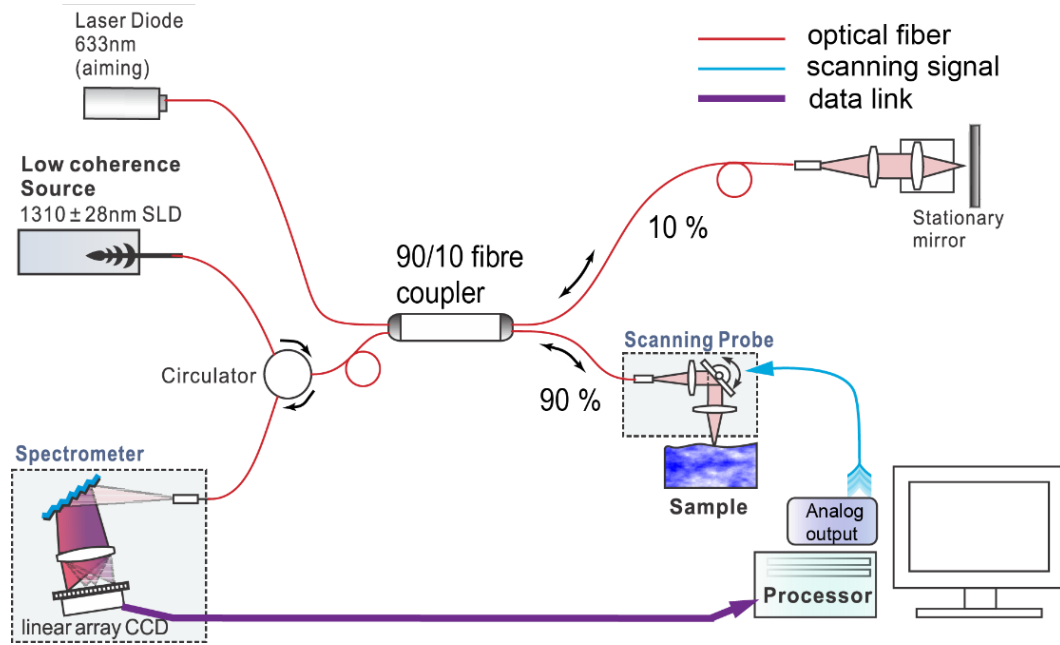


Figure 4-1 Schematic drawing of the SD-OCT system

Laser source

In this OCT system, an extended bandwidth Superluminescent Diode (SLD) light source (LS2000B, Thorlabs, Inc., USA) was employed. As in OCT imaging systems, the axial resolution is inversely proportional to the bandwidth of the light source, an extended broadband light source is essential to the OCT system performance. The LS2000B laser source features a dual SLD arrangement, which provides a high bandwidth ideal for high resolution OCT imaging system.

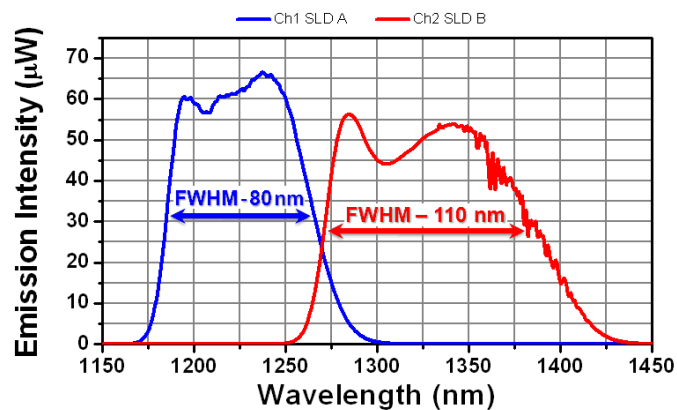


Figure 4-2 Emission spectrum of two separate SLDs in OCT laser source

The two SLDs in the laser source are designed so that their emission spectra are offset from each other, as plotted in Figure 4-2, the emission of SLD A and SLD B cover a FWHM bandwidth of 80nm and 110nm, respectively. The output of each SLD are delivered into Channel 1 and Channel 2. The output of Channel 3 and Channel 4 are the combination of both SLDs, featuring a total FWHM bandwidth of around 200 nm. The offset of SLD emission spectrums are arranged to minimize the deviation of combined spectrum from uniform distribution, as shown in Figure 4-3. Typical deviation from maximum intensity less than 3dB. The maximum emission power from each channel is more than 10 mW.

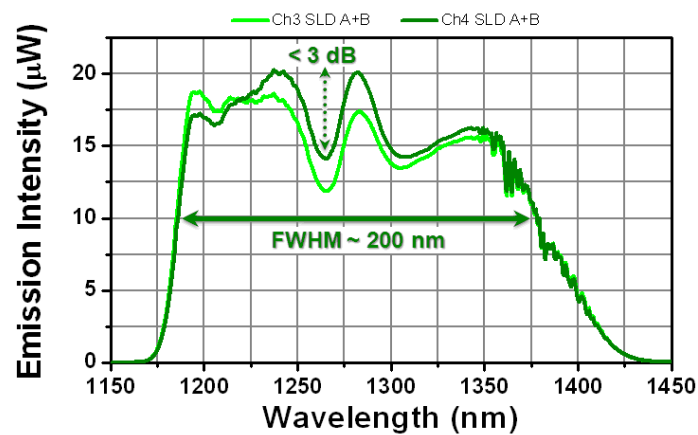


Figure 4-3 Emission spectrum of combined SLD output in OCT laser source

Interferometer

The broadband infrared laser are coupled into optical fibre through FC/APC ports. The first optical component after the laser source is an optical circulator. The purpose of the circulator is to re-direct the reflected coherent beam to the spectrometer, as well as avoiding any laser energy re-entering the laser source. Passing by the circulator, the light from the SLD is split into two paths with a 10:90 fibre based coupler, which works as a Michelson interferometer. The ninety percent power beam is delivered to the sample arm, whilst ten percent power beam goes to a reference mirror, referred to as the reference arm. The back-scattered laser from sample arm and the mirror reflected beam from reference arm meets again in the fibre coupler where the interference occurs and is then delivered to the spectrometer.

Reference arm

The reference arm consists of a collimator, a focusing lens and a stationary mirror. The stationary mirror is mounted to a linear translation stage, in order to position it on the focal point of the reference arm lens. The collimator-lens-mirror assembly creates a mirror re-insertion setup, in order to facilitate a stable, yet optical path length adjustable reflection of laser back into fibre. For the lens-mirror assembly, the reflected beam from a mirror that is placed on the focal point of a lens is always parallel from the incident beam. This configuration helps to minimize the requirement for alignment: since the mode field diameter of the optical fibre is only around $9.5\ \mu\text{m}$, it is extremely difficult to achieve a stable re-insert of the reflected laser into fibre mode field without a second focusing lens.

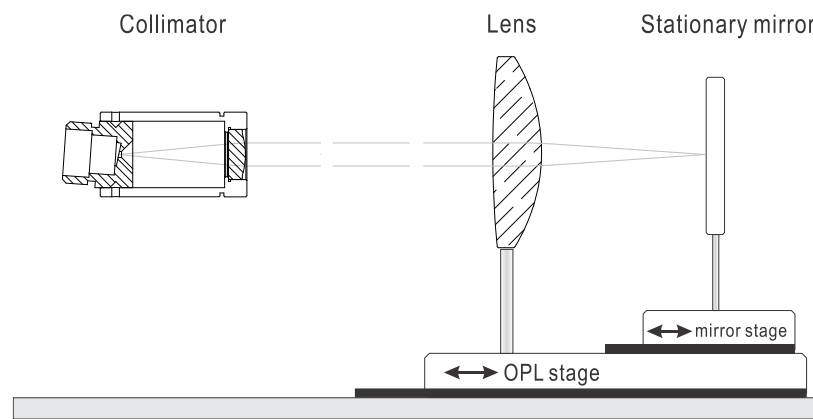


Figure 4-4 Reference arm assembly

The optical path length (OPL) of the reference arm is designed to be adjustable, in order to match the OPL on the sample arm. Hence, the lens-mirror assembly is mounted to another micrometer-driven linear stage, and the stage is aligned to be parallel to the collimated beam. The movement of micrometer will lead to an adjustment of the relative position of coherence window and the objective lens focal region.

Sample arm

The sample arm of an OCT system is the imaging probe in essence. The second beam

of the Michelson interferometer is delivered to another collimator (F260APC-C, Thorlabs, USA) to extract a collimated beam into free space. The theoretical $1/e^2$ beam diameter is 2.8 mm when combined with SMF-28e type fibre.

For the scanning, a pair of galvanometer scanning systems is utilized. A galvanometer is a precision motor with a limited travel, normally within 30 degrees. The acceleration of a galvanometer is directly proportional to the current applied to the motor coil. The servo driver board of galvanometer scanners are designed to output dynamic control voltages to scanners to drive the mirror position angle to be proportional to the input signal. With the rotation angle controlled by an analogue command signal from PC, the incident sample beam location is scanned on the lateral direction, so that 2 or 3 dimensional imaging can be achieved, depending on the scanning protocol. One mirror is scanned rapidly to form the B-scan, and the other one take one position increment for one B-scan, to form a C-scan.

For a specific objective lens, there exists a trade-off between the lateral resolution and imaging. The lateral resolution depends on the focal spot size, i.e. the beam waist size. For an incident beam with Gaussian shape, the beam waist size w_0 at the focal spot is given by[131]

$$w_0 = \frac{2f\lambda}{\pi\Phi_i} \quad [4.1]$$

where f is the focal length of lens, λ is laser wavelength, and Φ_i is the incident beam diameter. Normally, we regard the Rayleigh range as the optimal imaging range of OCT, since inside Rayleigh range the beam cross section area is less than twice of the minimum beam cross-section area[132]. The Rayleigh length is given by

$$Z_R = \frac{\pi w_0^2}{\lambda} \quad [4.2]$$

A conclusion from equation [4.1] and [4.2] is, to improve the lateral resolution, i.e. decrease the w_0 value, the focal length of the objective lens should be shorter,

meanwhile the optimal imaging range, $2Z_R$ is decreased. There are three lenses used on the OCT system, one microscopy scanning lens (LSM02-BB, Thorlabs Inc., USA) with equivalent focal length of 18mm, and two spherical lens with 30 mm/ 50 mm focal length. The performance of these objective lens were listed in Table 4-1. The microscopy scanning lens has 10X magnification, and best lateral resolution but very limited imaging range, while a 30mm lens is a good balance between depth range and lateral resolution, since it provides 8.5 μm lateral resolution within 480 μm imaging depth.

To eliminate the OCT image aberrations, the scanning beam needs to maintain a fixed direction during scanning. This requires that the rotation axis of the scanning mirror to intersect the focal spot of objective lens. Since there are two scanning mirrors, it is not possible to put the focal spot on both scanning mirror axis, consequently the focal spot is positioned on the axis of fast scanning mirror(B-scan mirror).

High-speed spectrometer

The spectrometer is an essential component of an SD-OCT system. The typical components of a fibre-coupled spectrometer include the collimator, diffractive grating, objective lens and linear detector array as shown in Figure 4-1. There are two determination factors of the axial resolution of an SD-OCT system, as 1) Spectral detection range of the spectrometer, and 2) available wavelength bandwidth of infrared laser.

Another performance criterion, axial signal intensity fall-off, is also determined with the optical resolution and spectral range integrated by each pixel of the spectrometer, since the origin of OCT intensity fall-off is the washout of fringe contrast as the object gets further away from zero-delay.

The spectrometer in our SD-OCT system is made of the following optical components: a collimator ($f = 50 \text{ mm}$), a transmission grating (1200 lines/mm), an achromatic focusing lens ($f = 100 \text{ mm}$) and a high speed line scan CCD camera (SUI, Goodrich Corp, NJ, USA). The camera is an InGaAs camera with 1024 active elements. A

Zemax simulation of the spectrometer is given in Figure 4-5.

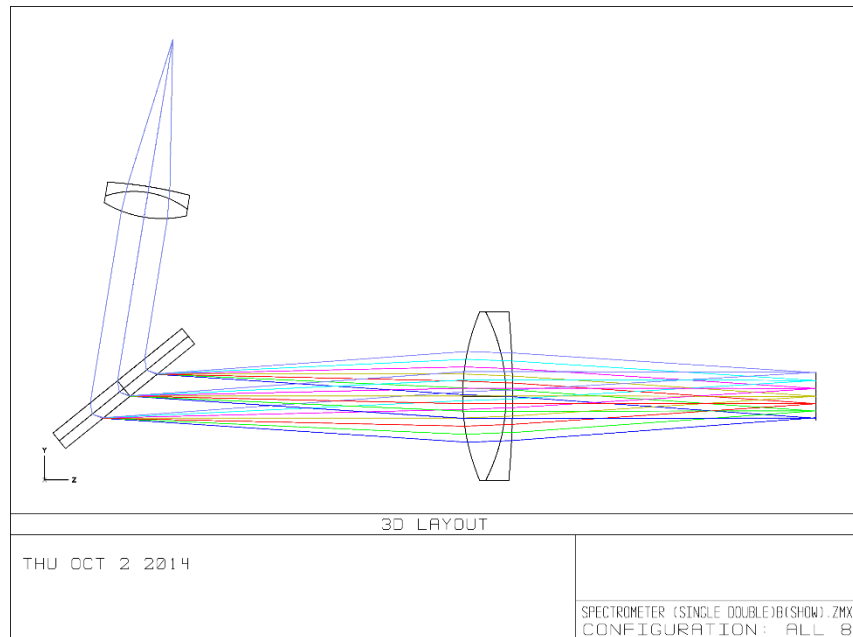


Figure 4-5 A ZEMAX model of spectrometer for SD-OCT system

In the design of this spectrometer, the orientation of the grating is fixed at the optimum incident angle at the center wavelength for the expected laser source spectrum, which makes the design relatively simple. The broad bandwidth coverage requires good achromatic optics. The achromatic lens was chosen to provide acceptable spot profiles through the entire spectrum of the light source. The line scan camera is capable of providing > 80% average detection efficiency with in the assorted light source wavelength range of 1200-1400 nm. The designed spectral resolution of the spectrometer was ~0.11 nm, and correspondingly, a 2.5 mm total detectable distance on each side of the zero delay location.

Processor

The processor in the SD-OCT system is designed for three functions:

- 1) Control scanning protocol and synchronisation of scanning and camera
- 2) Receiving data from line scan camera

3) Real time image processing and high-speed recording

Most of the processor components are based on NI (National Instruments Corp., TX, USA) platform. An analogue output card, NI PCI-6713 is used for sending galvanometer scanner driving signal, and camera trigger signal. The maximum update rate of this board is 1 MS(mega-sample)/sec. Image acquisition card NI PCIe-1429 is used for camera configuration and data transfer, based on CameraLink interface. A high-performance PC with 2.8 GHz quad-core Intel Core i7 CPU provided the hardware host platform.

4.2.3. Data acquisition in SD-OCT system

As described before, the SD-OCT data acquisition hardware is based on NI platform, hence the data acquisition program is implemented in LabVIEW (National Instruments Corp., TX, USA). A flow chart of the data acquisition program is presented in Figure 4-6.

The program first prepares a background reference data by either sampling the spectrum from the reference beam, or by loading in a previously captured data. The reference beam spectrum is captured by prompting the user to shade the sampling arm, and sending trigger signal to camera to capture a number of A-lines, followed by performing average operations to obtain a higher SNR. Then this data was stored for future use. Since the reference data generally remains stable, the acquisition of this data is only necessary when performing a daily calibration, on the beginning of each experiment. After preparation of the reference data, the analogue output system and NI-IMAQ system are initialized: the NI PCI-6713 card is configured to output trigger signal and scan mirror driving signal, and image acquisition parameters are also configured for NI PCIe-1429.

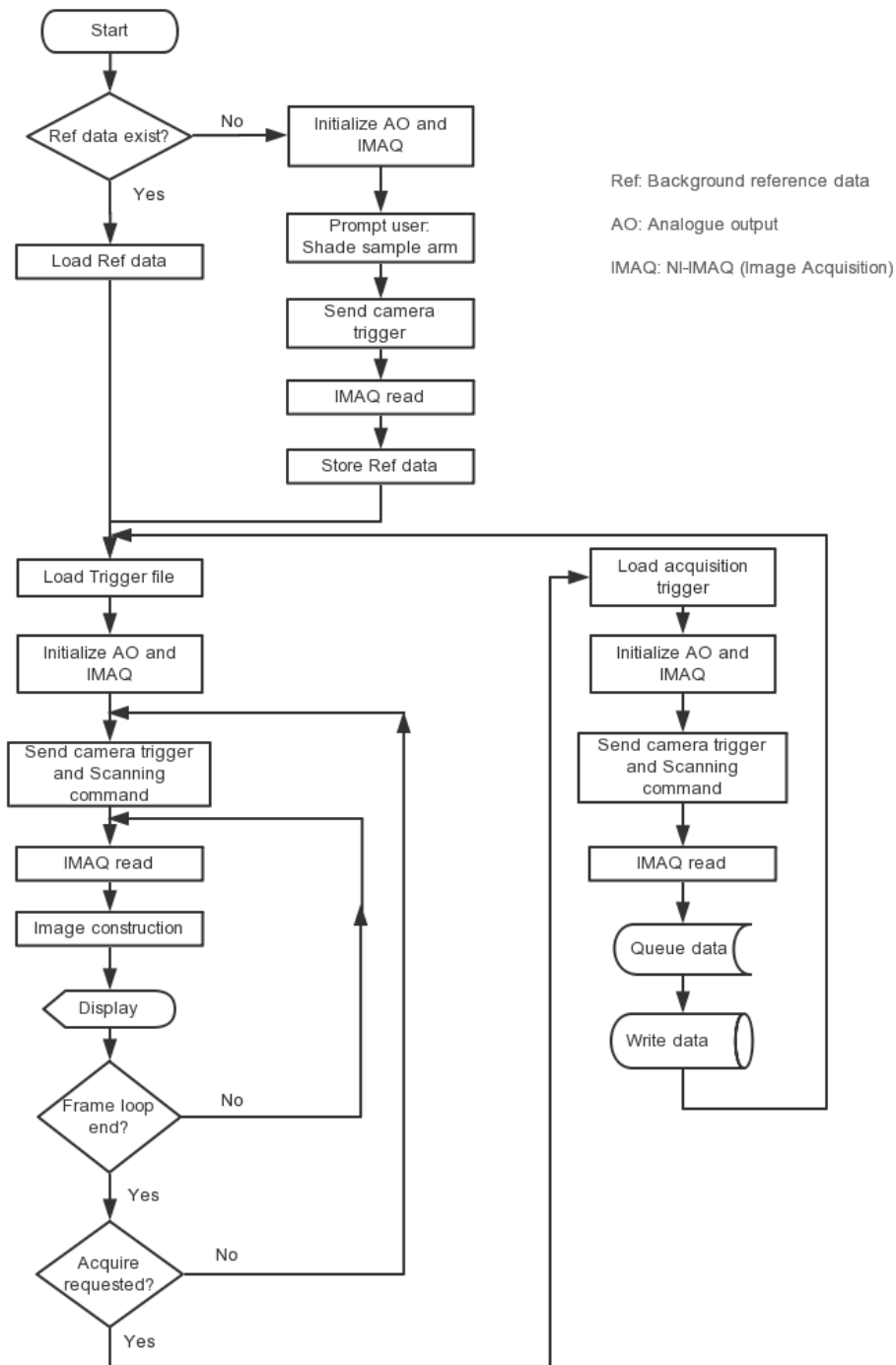


Figure 4-6 OCT data acquisition program flowchart

The OCT system can be operated in two modes: real time mode, and acquisition mode, as shown in Figure 4-6. The scanning protocols of these two modes can be defined

separately. Normally OCT is used for 3-D structural imaging, these two modes use same scanning protocol, with the real-time mode to observe the scanning area on-line, and the acquisition mode to record data for off-line processing. The two modes follows similar workflow: loading pre-defined trigger file, initialization of AO(analogue output) and IMAQ(National Instruments IMAge AcQuisition), camera data collection, and image display or raw data storage. For acquisition mode, since the data transfer rate from camera to the PC is faster than hard drive writing speed, to avoid data overflow, some part of the RAM is preserved for a cache zone, i.e. a “queue”, then raw-data are re-written on to hard drive. For real-time mode, the CPU repeatedly reconstructs the images that was obtained from camera, achieving up to 40 frame per second and displayed real-time. The image reconstruction is explained in the following “Data processing” section.

In OCT image acquisition, the controlling of scanning mirror position and its synchronization is an essential function. To implement this feature, “trigger files” are created prior to OCT imaging acquisition, pre-defining the scanning protocol. The trigger file contains the scanning mirror driving pattern and the camera trigger signal. Matlab code is used for the generation of trigger files, and the code is integrated in LabVIEW for a user-friendly GUI (graphic user interface). A trigger file example of a 3-D scanning protocol is depicted in Figure 4-7, with a frame number of 256, A-line number 256, frame rate 140 fps (frames per second). Two channels of the trigger file is allocated for scanning mirror positioning control. Channel 1 is a triangle wave, with typical rising time ratio of 85%, controlling a linear scan of the X-galvonometer for B-scan. Channel 2 is the control signal to Y-galvonometer, for C-scan. The Y-axis scan signal is a step signal, with a step time equal to one B-scan period. On channel 3, IMAQ trigger is sent to the NI PCIe-1429 image acquisition card, to trigger the receiving of camera data. Channel 4 signal is the gating trigger for camera exposure. The camera is operated in “internally timed, externally gated” mode, while the camera repeatedly exposures according to its internal clock when the external trigger is TTL high.

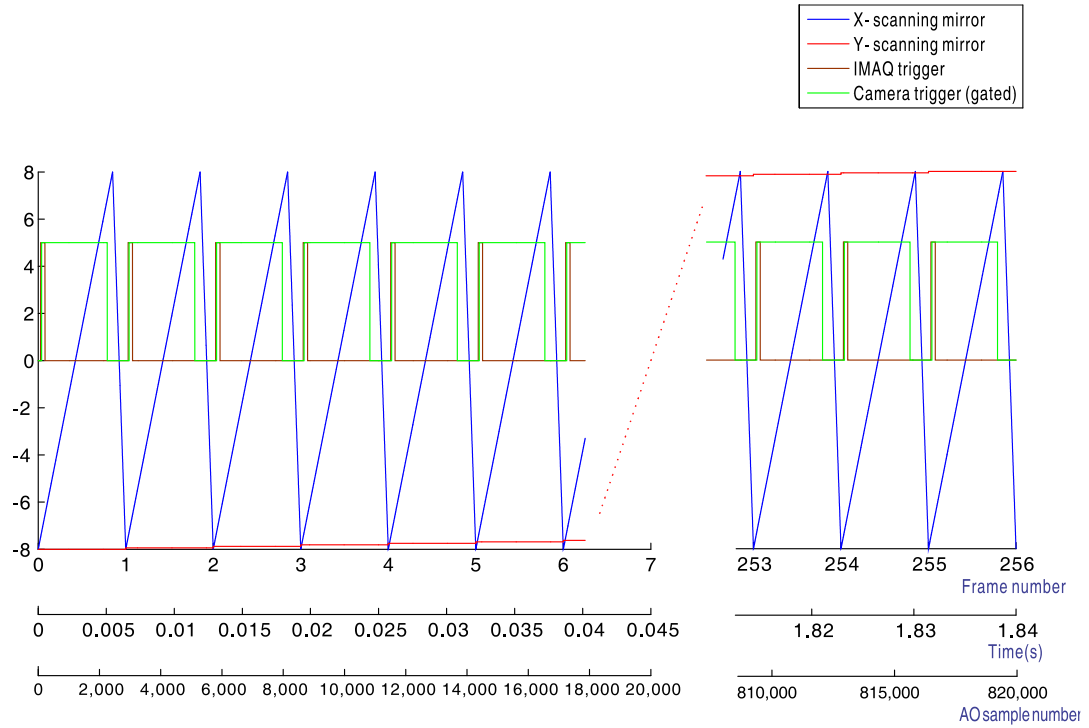


Figure 4-7 Trigger file example for a 3-D OCT scanning

With NI PCI 6713 analogue output card, the aforementioned 4 channel signals are output through the DAC (digital analogue converter) module, and sent to the corresponding control ports through BNC cable. The starting of output is triggered by either a TTL signal generated by the same AO card, or by an external TTL signal (for example, the synchronization signal from pulsed laser source).

4.2.4. OCT data processing

Dispersion compensation

In theory, the spectral interferometry Fourier domain OCT is based on the equation $F_s(z) \propto \text{FT}\{A_s(K)\}$, where z stands for depth, K stands for wavenumber; in which the spectrum of the back scattered sample light amplitude $A_s(K)$ is obtained using a spectrometer. Practically, with the broad spectral bandwidth and the fact that the optics could not be exactly identical in the sample beam and reference beam, the dispersion difference can lead to a non-linear sampling in k -space, thus deteriorate the axial

resolution when obtaining $\text{FT}\{A_s(K)\}$. Therefore, dispersion compensation is important for a high-resolution OCT imaging system.

In time domain OCT with analogue demodulation dispersion compensation is usually performed by matching the optical materials and path lengths in the two interferometer arms [133-135]. Grating based phase delay scanners can also be used to provide dispersion compensation with group and phase delay scanning[136]. These methods require re-adjustment if the dispersion varies between samples, hence it presents limited practical functionality.

For the SD-OCT system, a numerical *a posteriori* dispersion compensation technique has been developed to correct the dispersion on the detected spectrum. A flow chart of spectral domain OCT dispersion compensation procedure is given in Figure 4-8.

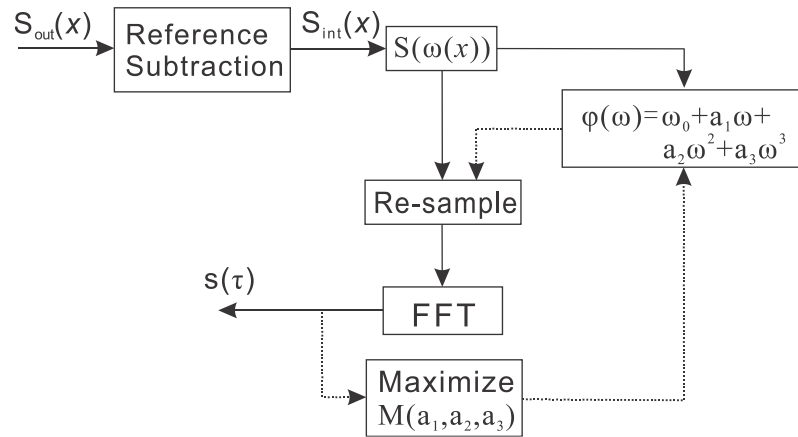


Figure 4-8 SD-OCT dispersion compensation procedure flowchart. Dashed path shows the dispersion compensation

The spectral signal sampled at the line-scan camera $S_{\text{out}}(x)$ is subtracted by the reference signal that was obtained from the reference beam, leaving only the interference signal $S_{\text{int}}(x)$. A third-order function of evenly sampled k -space to dispersed k -space is constructed, and the compensation path (dash line in Figure 4-8) then uses Fourier domain reflector magnitude to find optimised parameter, in order to maximise the magnitude of post-FFT OCT signal at the reflector location. In Figure 4-9(a1) (a2), the spectral interferogram without dispersion compensation produced by two reflectors (at $\sim 0.22\text{mm}$ and 1.08mm from the zero delay location) are plotted,

together with an optimized k-space function (mapped to line-scan pixel number for more intuitive presentation). Note that in this region this wavenumber function is a concave function. The spectrum was then re-sampled (interpolated) according to the discrete point set on this function curve to recover an evenly-spaced k-space interferogram, as depicted in Figure 4-9(b1) (b2). In this example the interferometry fringes are shifted to the left, in correspondence to the k-space concave function.

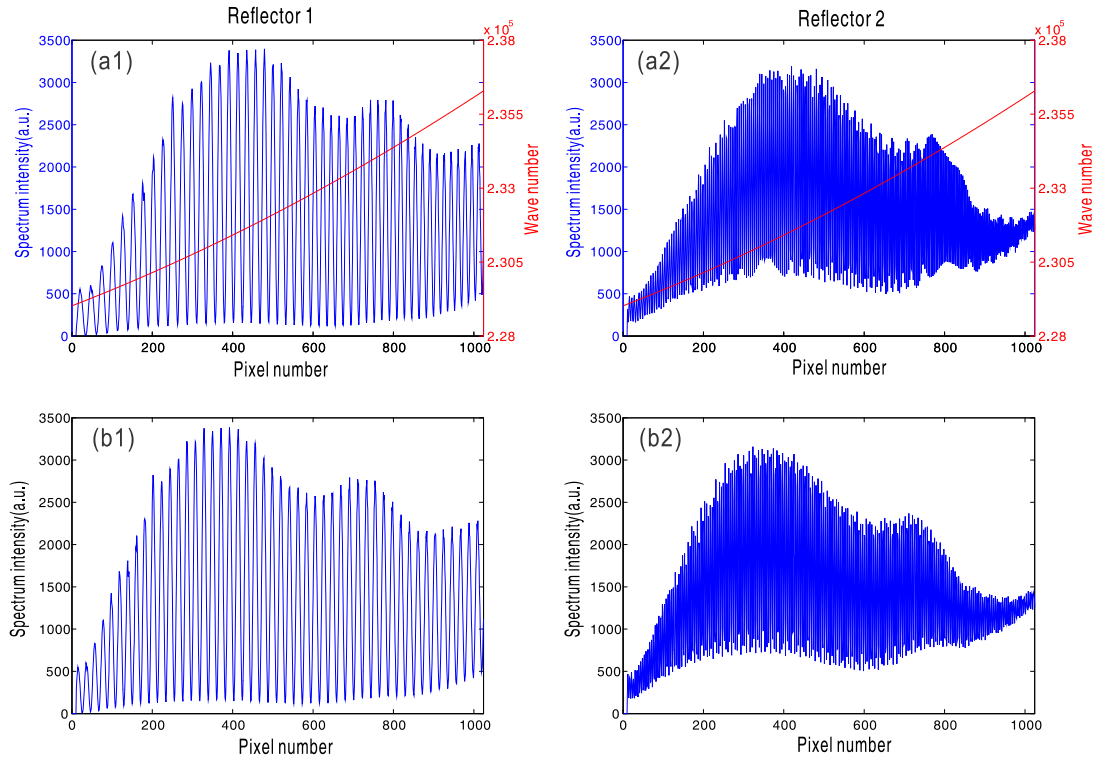


Figure 4-9 Raw spectrum from camera and the dispersion compensation, (a1,a2)
un-compensated spectrum of the interferogram produced by two reflectors
(b1,b2) compensated

After the FFT operation on the spectrum data, the OCT signals obtained from both the compensated and un-compensated spectrum are shown in Figure 4-10. The coherence range (i.e. OCT resolution) is significantly improved after compensation, with a significant improvement in the signal to noise ratio. This dispersion compensation technique facilitated the SD-OCT system to maintain an axial resolution performance that is close to the theoretical value ($9\text{ }\mu\text{m}$ and $4\text{ }\mu\text{m}$).

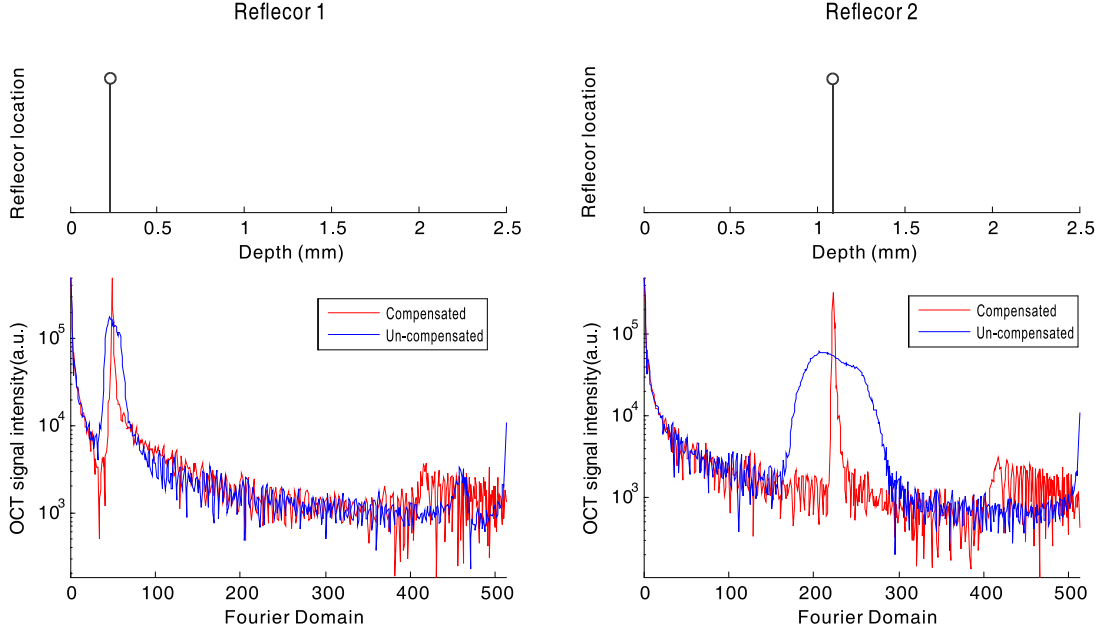


Figure 4-10 OCT intensity signal from compensated spectrum

OCT imaging and phase detection

In SD-OCT, the interference fringes at the linear detector after a proper dispersion compensation can be expressed by[137]:

$$i(k) = \frac{1}{2} \rho S(k) \delta k \left\{ R_R + \sum_n R_n + 2\sqrt{R_R} \sum_n \sqrt{R_n} \cos[2k(\Delta z_n + \delta z_n)] \right\} \quad [4.3]$$

where $S(k)$ is the source power spectral density; k is the wave number (in radians per meter); δk is the spectral bandwidth of light source; ρ is the detector responsivity; R_R is the reference arm reflectivity and R_n is the reflectivity of the sample at location z_n (i.e., local reflector). Δz_n is an integer multiple of discrete sampling interval in z domain (depth), given by $m\pi/\delta k$, where m is any positive or negative integer indexing 1-D z domain A-scan array. δz_n is the sub-resolution deviation of the local reflector (scatterer) location away from Δz_n . As the PhS-OCT mainly detects the sub-resolution movement, δz_n is the primary determinant factor of the OCT signal phase.

A Fourier transformation of $i(k)$ (realistically, discrete Fourier transformation) will give the complex-valued z domain signal [137]:

$$\mathbf{I}(2\Delta z_n) = \frac{\rho S_0 (R_R R_n)^{1/2}}{2ef_s} E(2\delta z_n) \exp(jk_0 2\delta z_n) \quad [4.4]$$

where S_0 is the total sample illumination power, i.e. $\int S(k)dk$. The term $E(2\delta z_n)$ denotes the unity-amplitude z domain autocorrelation function, k_0 is source centre wavenumber, and f_s is the A-scan rate in Hz. This complex signal \mathbf{I} is normally referred to as the OCT complex signal, with its absolute value is the depth (z) resolved backscattered laser intensity, i.e. structural image. The phase of \mathbf{I} is proportional to δz_n , i.e. representing the motion signal.

For the phase-resolved method [138], the instantaneous displacement of a local scatterer between two successive A-scans is equivalent to the instantaneous Doppler shift represented by the derivative of the phase with respect to time, which can be written as:

$$\begin{aligned} d(t) &= \frac{\lambda_0}{2 \cos \theta} f_{dopp} \\ &= \frac{\lambda_0}{4\pi \cos \theta} f_s [\angle \mathbf{I}(2\Delta z_n, t) - \angle \mathbf{I}(2\Delta z_n, t - f_s^{-1})] \end{aligned} \quad [4.5]$$

Here \angle denotes phase operator, λ_0 is the central wavelength of the light source, f_{dopp} is the Doppler frequency shift, f_s is the A-scan rate, and θ is the Doppler angle between optical axis and motion direction. In the most cases, one assumes the sample displacement is only in optical axial direction, meaning that only displacement vector projection on axial direction is detected, Eq.[4.5] can be simplified to :

$$d(z, t) = \Delta \varphi(z, t) \lambda_0 (4\pi T_s)^{-1} \quad [4.6]$$

where $\Delta \varphi(z, t)$ is the phase difference between adjacent A-scans at location (depth) z and time t .

Using the above principles, Both OCT structural images and motion detection images can be reconstructed from the camera data, thus this SD-OCT system is also classified as a Phase-Sensitive Optical Coherence Tomography (PhS-OCT) system.

The reconstruction of B-scans can be real-time updated in the LabVIEW program GUI, while the motion detection image that compares adjacent A-lines in a B scan can also be provided as a preview of the displacement that is induced in the imaging range. To achieve high frame rate shear wave imaging, there are still more configurations to be made, and will be expounded in detail in the next section.

4.3. Shear wave imaging technique

To develop a high-sensitivity, high-speed shear wave imaging (SWI) technique using the OCT system is one of the main objectives in this study. This section describes the SWI technique for the acquisition of wave propagation data with PhS-OCT system; particular attention is paid to the method of wave field data recovery in such a way to obtain the maximum of information and the minimum of artefact error and uncertainty. The possible defects of OCT motion detection and different sources of artefact errors of the acquisition are presented, considering the procedures to reduce their effect. This allows to give practical indications on the acquisition parameters, and to obtain high quality wave propagation data for improving the elastography accuracy.

4.3.1. Shear wave imaging hardware set up

The first practical step for shear wave imaging is the launching of shear waves in the sample. There are three methods for wave generation that are discussed in this dissertation, i.e. contact mechanical stimulation, acoustic radiation force impulse, and pulsed laser. The contact mechanical stimulation is the most direct and representative method, as its setup schematic is depicted in Figure 4-11.

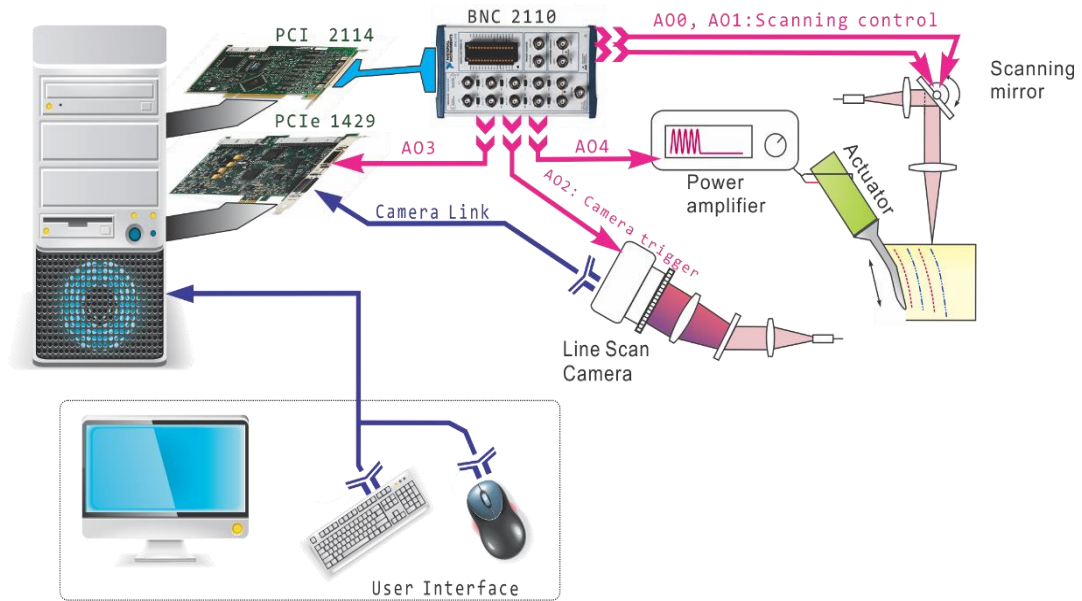


Figure 4-11 hardware set up of shear wave imaging technique with a contact mechanical stimulation

A low-voltage, stacked piezoelectric actuator is utilized as the mechanical stimulation source in the contact generation of shear waves. The driving signal is either generated by a function generator, or directly from the analogue output card. As shown in Figure 4-11, five analogue output channels are used for controlling the PhS-OCT system: AO0 and AO1 are allocated for scanning mirror positioning control, AO2 is preserved for camera trigger, AO3 is to generate trigger signal for IMAQ card, and AO4 for generating driving signal for the actuator.

The hardware setup for Acoustic Radiation Force Impulse (ARFI) generated shear wave imaging and pulsed laser generated shear wave imaging differs from the contact mechanical stimulation SWI in the synchronization scheme. The external triggering is not provided for the ultrasound controller, nor for the pulsed Nd-YAG laser. To meet the need for precise synchronization in SWI, the OCT system is re-programmed to be capable of receiving trigger signals. The schematic drawing of the hardware set up for ARFI-SWI and pulsed laser SWI are shown in Figure 4-12

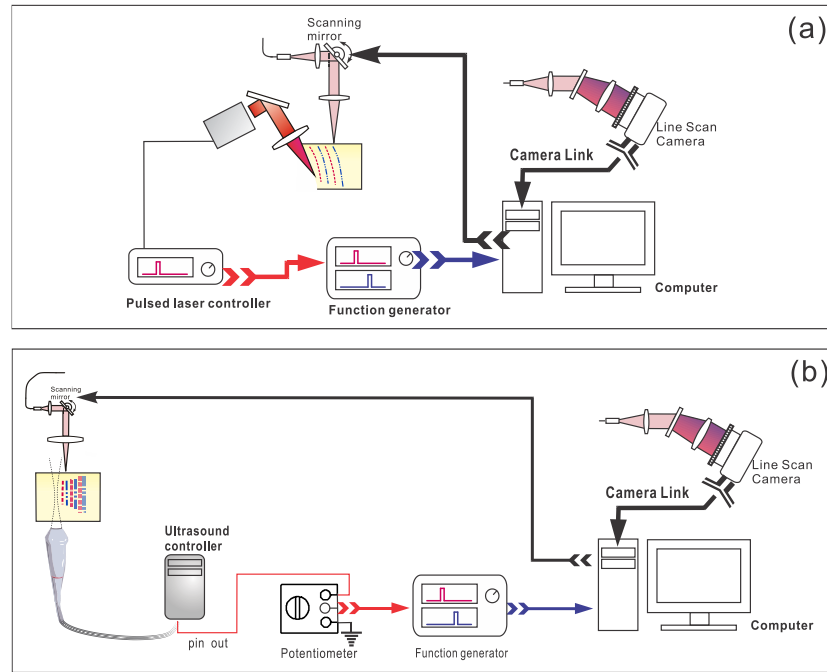


Figure 4-12 Synchronization setup schematic of ARFI-SWI (a) and pulse laser SWI (b)

The Continuum Surelight Nd:YAG laser source controller provided a TTL-compatible synchronization signal after 50 ns of the pump discharge. For synchronization between PhS-OCT and the pulsed laser, a function generator is used as a delay generator, and delay the rising edge of the laser source sync signal by 99.5 ms, i.e. 0.5 ms before the laser pulse, to trigger the start of PhS-OCT acquisition.

A similar technique is also applied to ARFI-SWI. In the ultrasound controller, the ultrasound burst pushes repetition rate is 140Hz, the driving signal from the center element is taken out, and attenuated to act as a synchronization signal. Then this signal is passed on to function generator which produces a trigger signal for the starting of PhS-OCT acquisition.

4.3.2. Data acquisition

To track shear waves propagating in tissue, the PhS-OCT was operated in M-B mode, wherein a sequence of 256 A-scans (one M-scan) was captured at every spatial location sequentially within the B-scan (total 128 locations) mode while the actuator repeatedly

fired the stimuli. Thus, a complete M-B scan consisted of 256x128 A-scans. Synchronization of shear wave generation and OCT beam-scanning was precisely controlled using custom software written in the LabVIEW language.

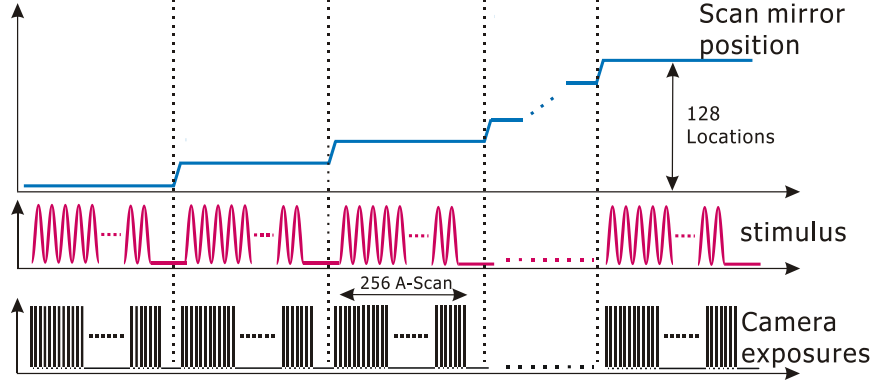


Figure 4-13 Timing schematic of shear wave imaging scanning protocol

The timing shematic drawing is shown in Figure 4-13. When the system A-scan rate was set to 46.992 kHz, M-scan repetition rate is determined as 140 Hz. Each M-B scan acquisition takes about one second. The 128 M-B scans were re-arranged to form 256 B-M scans. In this way, the re-arranged B-M scan had an equivalent frame rate the same as the A-line rate (~47 kHz). This high frame rate could provide a direct visualization of the propagating mechanical waves within a range of 1 to 7 kHz, commonly with wavelength of 0.1-1mm in soft tissue, which is appropriate for OCT imaging.

Phase-sensitive data output from the spectral interferograms were used to calculate 256 B-frames of the displacement field. Localized displacement estimates were obtained by comparing phase differences within the M-scan. The axial component of the displacement u_z at a given pixel at time t , i.e., $u_z(x, z, t)$, was computed from the linear relationship between displacement and phase difference between adjacent A-scans:

$$u_z(x, z, t) = \frac{\Delta\phi(x, z, t) \cdot \lambda}{4\pi n} \quad [4.7]$$

where $\Delta\phi$ is the detected phase change, λ is the central wavelength of the SLD

(1310 nm) and n is the refractive index of the sample. Figure 4-14 illustrates this scanning scheme, where the displacement field over a cross section is imaged with time. A typical structural image is also presented in this figure.

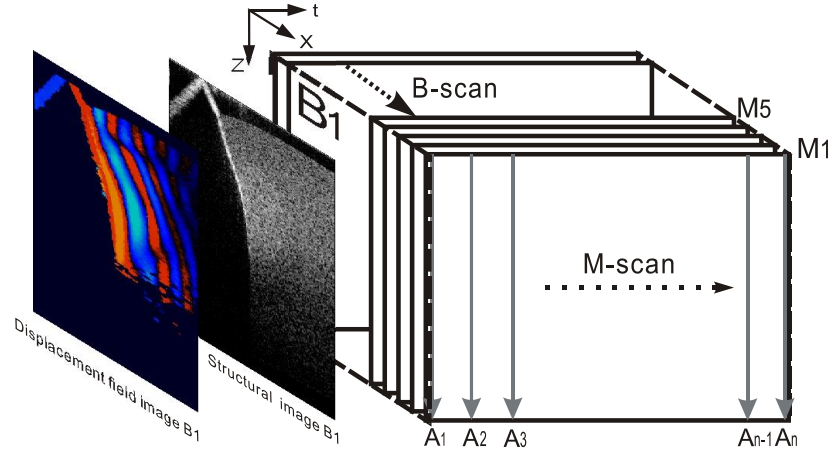


Figure 4-14 Illustration of shear wave imaging scanning protocol

In the experiments, when the camera is operated at 47kHz A-scan rate, each M-scan took approximately 15 ms, thus the full M-B scan took less than 2 seconds for a single measurement. The scan range of the B-scan (128 locations) was 2.5 mm, which limited the lateral pixel size at $\sim 25 \mu\text{m}$. The axial pixel size is $\sim 5 \mu\text{m}$. The dynamic range of the PhS-OCT system was measured to be $\sim 100 \text{ dB}$ at 0.5 mm axial depth with a phase noise of 3 mrad (milli-radian). However, the SNR in the region of interest (ROI) of the tissue sample was $\sim 50 \text{ dB}$.

4.4. Shear wave imaging data processing

4.4.1. Phase unwrapping on wave field data

According to the working principles of OCT motion detection that are given in the previous section, the motion detection is based on the phase difference between adjacent A-scans. By definition, the calculated difference ($\Delta\varphi$) is an instantaneous phase, i.e. a wrapped phase. Phase wrapping happens if $|\Delta\varphi| > \pi$, hence, when the instantaneous displacement amplitude u_z is larger than $4n/\lambda$ (see Eq.[4.7]), the motion detection results will present wrapped images, and these images are unusable unless they are first unwrapped so as to form a continuous phase map.

The phase unwrapping operations of images that are sampled at sufficiently high sampling rates, and that do not contain noise, or sudden phase changes, are relatively simple and this process can be carried out using the 2D Itoh Phase unwrapping algorithm[139]. However, as soon as any single one of these three conditions is violated, the phase unwrapping can become a difficult task to accomplish: the presence of noise can cause false phase wraps, which is difficult to differentiate from genuine wrapping. Furthermore, the phase unwrapping is accumulative in nature: if a single genuine phase wrap is missed due to noise, or a false wrap appears, an error occurs in unwrapping and this error then propagates throughout the rest of the image.

A large number of algorithms have been suggested as solutions to the phase unwrapping problems, while the most robust of the numerous algorithms can still fail in many occasions[140]. Driven by the application of shear wave imaging which leaves no margin for error, a few 2-D unwrapping algorithms were explored and tested on the shear wave imaging data, including multi-grid techniques[141], network programming unwrapping[142] and some quality-guided phase unwrapping algorithm[143], etc. Among the tested algorithms, an algorithm based on reliability sorting following a non-continuous path (2D-SRNCP algorithm) [144] has been tested

to be the most suitable and robust phase unwrapping algorithm for OCT-SWI data, with very low execution time, and no human interaction is necessary. The example of phase unwrapping results on SWI data is given in Figure 4-15.

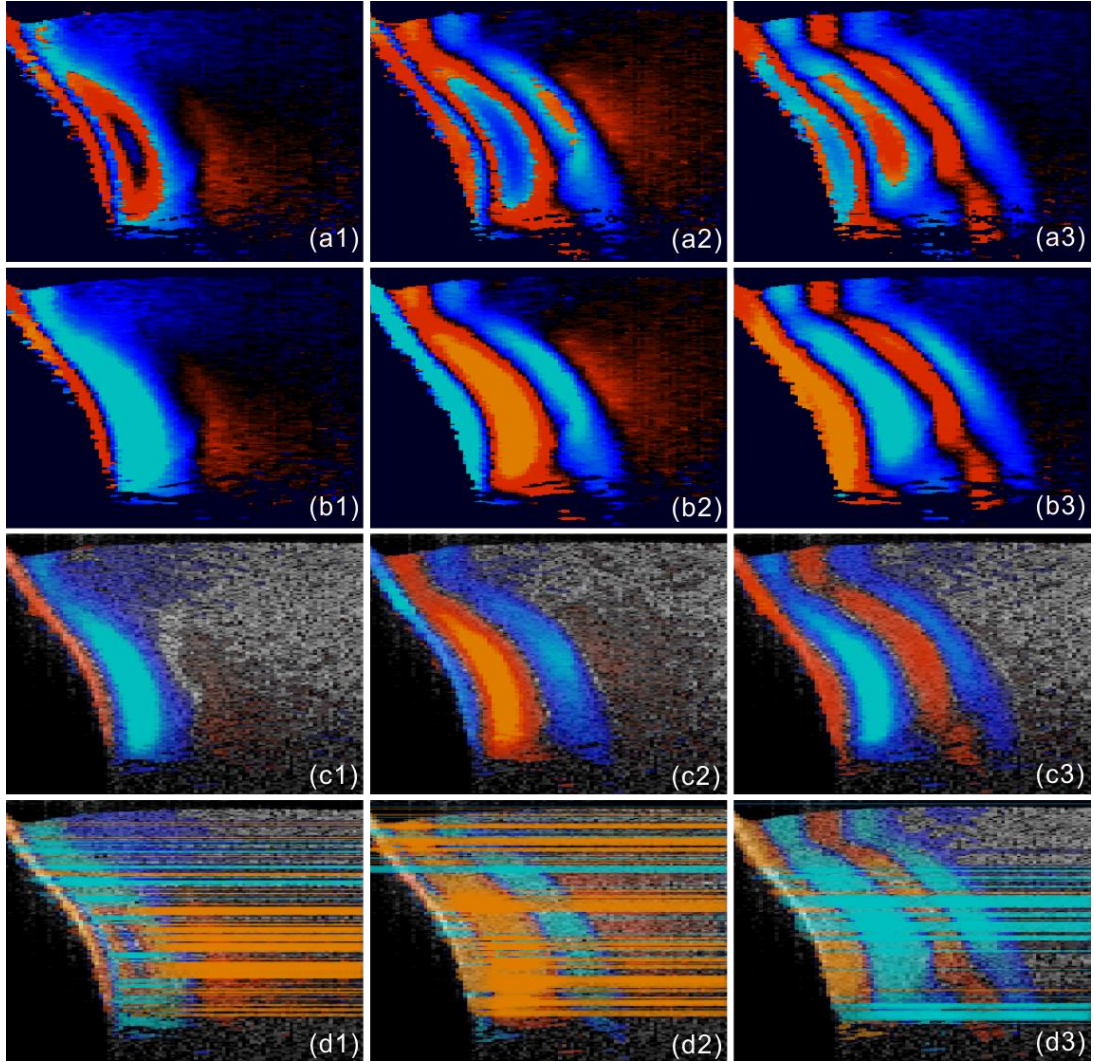


Figure 4-15 Comparison of phase unwrapping methods

(a1-a3) wrapped shear wave images at 5Ts, 10Ts, and 15Ts (b1-b3) unwrapping results of shear wave images at 5Ts, 10Ts, and 15Ts using Miguel 2-D unwrapping algorithm; (c1-c3) overlapping visualization of unwrapped data; (d1-d3) overlapping visualization of simple sequential 2-D unwrapping algorithm, T_s =Sampling period(23.5 us)

In Figure 4-15(a1-a3) the wave snapshots captured by PhS-OCT are given, this dataset is obtained in a soft tissue-mimicking agar phantom, with a cylindrical inclusion

embedded. The shaker tip is attached to the left side of the phantom, and generating a vibrating motion in the depth direction. Shear wave images are captured with an equivalent frame rate of 47 kfps (kilo frames per second). The total peak-to-peak displacement of the shaker tip is estimated to be 5 μm , as the shear wave images are the differential displacement field snapshot, the maximum displacement is inducing a wrapped phase in many locations, especially in the region that is close to the shaker tip. The presence of phase wrapping artefact in the wave field snapshots will obviously deteriorate the accuracy of wave velocity estimation that is based on the spatial-temporal propagation data of shear waves.

In the post processing of the SWI data, the 2D-SRNCP algorithm is implemented with c++ language and MATLAB code, before applying to this dataset, and the unwrapped data is visualized as Figure 4-15(b1-b3). The wave snapshots are also overlapped on the corresponding OCT structural image in Figure 4-15(c1-c3). This unwrapping algorithm showed a remarkable capability and robustness to provide a fixing of phase-wrapping for all wave field images. For comparison, the phase-unwrapping results using a simple, sequential, repeated 1-D phase unwrapping algorithm provided in the MATLAB function library is given in Figure 4-15(d1-d3). This algorithm has showed multiple failures in all the wave field snapshots, caused by the presence of noise and false decisions of phase wraps. The propagation of this error has induced multiple lateral stripes, which severely decreased the image quality.

As a short conclusion, 2D-SRNCP algorithm is proved to be an effective phase-unwrapping method for SWI images, which helps to improve the SWI data quality, and enables the utilization of large displacement amplitudes, which further extended the applicability of OCT-SWI.

4.4.2. Surface ripple artefact removal

In some experiments of shear wave imaging, a wave artefact is found to arise in the detection of mechanical waves with PhS-OCT. This motion artefact was then proved to be a combined product of sample surface motion and refractive index difference between sample and air, which cannot be neglected when imaging the displacement within tissue. The detailed description of the cause of formation is given in this section, together with a method of compensating the motion artefact. The theoretical analysis and experimental results are published in journal paper [J-1] and necessary figures are adapted from this paper.

Theoretical analysis of surface ripple artefact

Based on the principle about OCT motion detection introduced in the last section, it is reasonable to assume that $\Delta\phi(z, t)$ calculated between adjacent A-scans is caused by the displacement of the scatterer at the location z . However, OCT phase signal is in fact only sensitive to the path-length difference between the optical path length (OPL) of reference mirror and the OPL of the scatterer at the location z in the interferometer. In terms of measured phase change, it is accumulated over the optical path along the sample beam. Thus, $\Delta\phi(z, t)$ is the true representation of the displacement of the scatterer only when there is no OPL perturbation above the scatterer of interest. This requirement is met when 1) there is no tissue movement above the scatterer, and 2) refractive index along the beam propagating path in the sample arm is uniform over time. While these conditions are generally satisfied in the use of phase-resolved technique to evaluate the blood flow velocity, they become complicated when using PhS-OCT to monitor/trace the propagating waves within sample induced by a mechanical stimulus. Mechanical stimulus may induce different mechanical waves propagating within tissue, for example shear wave, Rayleigh wave (surface acoustic waves), and longitudinal waves. Even more complicated is the case of heterogeneous properties of the sample because by definition, elastic heterogeneities produce reflected waves. All these mechanical waves would affect the accuracy of PhS-OCT monitoring of the movement of the scatterer at the location z due to the dynamic mechanical wave of interest.

In the current study the research interest is to use PhS-OCT to track the shear wave propagating within tissue, the phase difference detected is induced by dynamic OPL change. Assuming that the tissue is uniform in refractive index, two main factors can cause a change in OPL: 1) the motion of the scatterer due to the shear wave of interest, and 2) the tissue surface motion at air-tissue interface that perturbs the OPL along the detection beam. The latter becomes a severe artefact in the dynamic motion detection. Because the phase change is accumulated along the optical path, the detected value is the summation of phase changes due to these two motions. This situation is shown in Figure 4-16:

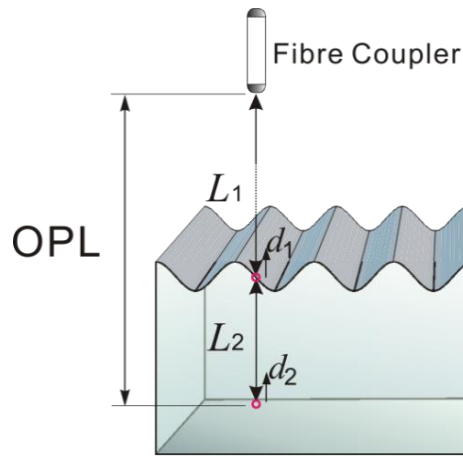


Figure 4-16 Illustration of a situation when OCT phase is influenced by both sample surface motion and scatterer motion

Note that in this case, The change of refractive index due to compression wave is not considered, based on two reasons: 1) The change of refractive index caused by compression is very small. Even in extreme condition of 1% density change under shock compression[145], the refractive index change is only 1.7×10^{-4} . This magnitude is too small to cancel out the OPL change in shear wave imaging. And 2) for gels and soft tissues, the assumption of incompressibility is widely used for modelling mechanical waves in tissue[146, 147], where the wave amplitude is small (micron scale).

Assume that the scatterer of interest is located at the depth of L_2 away from the sample surface, and the distance is L_1 between sample surface and the fibre coupler where the

reference beam and reflected sample beam interfere, the total equivalent OPL takes the form

$$OPL_0 = L_1 n_1 + L_2 n_2 \quad [4.8]$$

at the time $t = 0$ when there is no motion. Here, n_1 is the refraction index of air and n_2 is that of the sample. At a successive A-scan ($t=T_S$, where $1/T_S$ is the A-scan rate of the OCT system,), the sample surface moves a distance of d_1 while the scatterer travels a distance of d_2 , (defining the motion towards detector is positive direction). Thus, the equivalent OPL at the time $t=T_S$ becomes

$$OPL_1 = (L_1 - d_1)n_1 + (L_2 + d_1 - d_2)n_2 \quad [4.9]$$

The OPL difference between the times $t = 0$ and $t=T_S$, which gives rise to $\Delta\phi$, is then,

$$\Delta OPL = OPL_0 - OPL_1 = d_2 n_2 + (n_1 - n_2) d_1 \quad [4.10]$$

Here, the term $d_2 n_2$ is caused by the true motion of the localized scatterer. $(n_1 - n_2) d_1$ is caused by the surface motion, e.g. SAW induced by the mechanical stimulus. This latter term would give rise to an artefact to the experimental measurements of the motions beneath the sample surface in the z domain. Therefore, within the B-frame image of the displacement field that is determined by the PhS-OCT system, a propagating surface wave will lead to stripe artefacts according to the above analysis.

From Eq.[4.10], when the scatterer is close to surface, i.e. $L_2 \rightarrow 0$, the scatterer displacement will approach the surface displacement, i.e. $\lim_{L_2 \rightarrow 0} d_2 = d_1$. Then, we have,

$$\begin{aligned} \lim_{L_2 \rightarrow 0} \Delta OPL &= d_2 n_2 + (n_1 - n_2) d_1 = d_1 n_2 + (n_1 - n_2) d_1 \\ &= d_1 n_1 \end{aligned} \quad [4.11]$$

Thus, if the detected phase near the sample surface is $\Delta\phi_{surf}(z_{surf}, t)$, we have,

$$d_1 = \frac{\Delta\varphi_{surf}(z_{surf}, t)}{n_1} \quad [4.12]$$

Therefore, combining Eq.[4.12], Eq.[4.10] and Eq.[4.7], the real phase change $\Delta\varphi_c$ due to the motion of the scatterer at the location z can be deduced:

$$\Delta\varphi_c(z, t) = \Delta\varphi_d(z, t) + (n_2 - n_1)\Delta\varphi_{surf}(t) \quad [4.13]$$

where $\Delta\varphi_d$ and $\Delta\varphi_{surf}$ are the phase changes directly determined by PhS-OCT at the location z and at the surface, respectively.

Experimental evidence of artefact

To demonstrate the presence of the artefact, a layered glass plate phantom is fabricated to create a condition where the mechanical wave is propagating within a layer of soft phantom between free surface and a glass plate while at the bottom there is an air gap above the substrate rigid body (steel plate), see [Figure 4-17\(a\)](#). With this configuration the steel plate can be safely assumed to be static, i.e. without mechanical waves propagating in it, because the glass plate and a layer of air isolate the acoustic waves from the soft phantom. And also the excitation is not able to launch detectable motion in steel with given frequency and amplitude. In the experiments, the stimulation tip was driven by a stack piezoelectric actuator, and the tip was emitting 5 kHz sine waves of 5 cycles. All the phantoms were more than 50mm in diameter and at least 15mm deep, to avoid any reflected wave from the boundaries. The vibration amplitude was below 3 μ m. The tip was a wedge-like shape, with a width of 1.7mm edge. The waves generated by this tip can therefore be considered approximately planar, having negligible out-of-plane displacement, which simplifies the experiments for 2-dimensional analysis. When attaching the tip to the sample, the OCT system was used to provide the real-time B-scan of the region of interest.

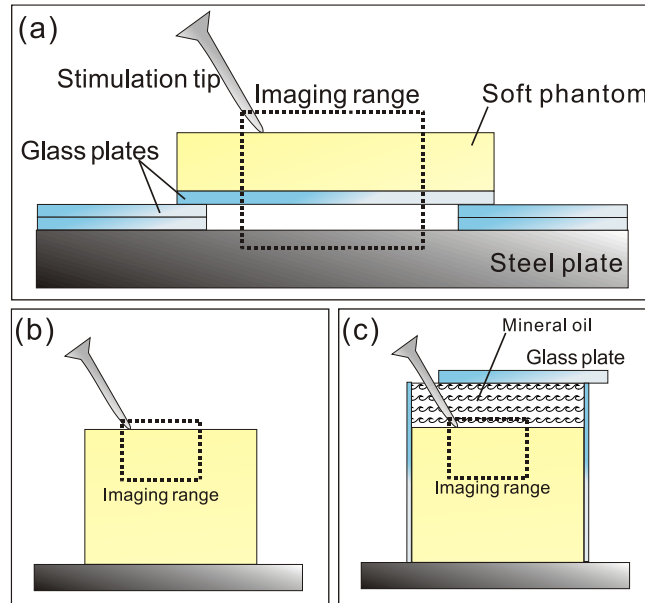


Figure 4-17 Illustration of phantom configuration in surface ripple artefact experiment

(a) thin phantom plate (b) large homogeneous phantom in air (c) large homogeneous phantom with a layer of oil and a glass plate in the top. Note in (b) and (c), the dashed box indicating imaging range (B-scan) is not in scale

After processing PhS-OCT data, a video that provides visualization of propagating mechanical wave was generated. The phase map was encoded with bi-polar color map, where red color denotes the motion towards the OCT light beam. The phase image was then overlaid onto the OCT B-scan structural image, with higher transparency for lower amplitude of motion, as shown in Figure 4-18.

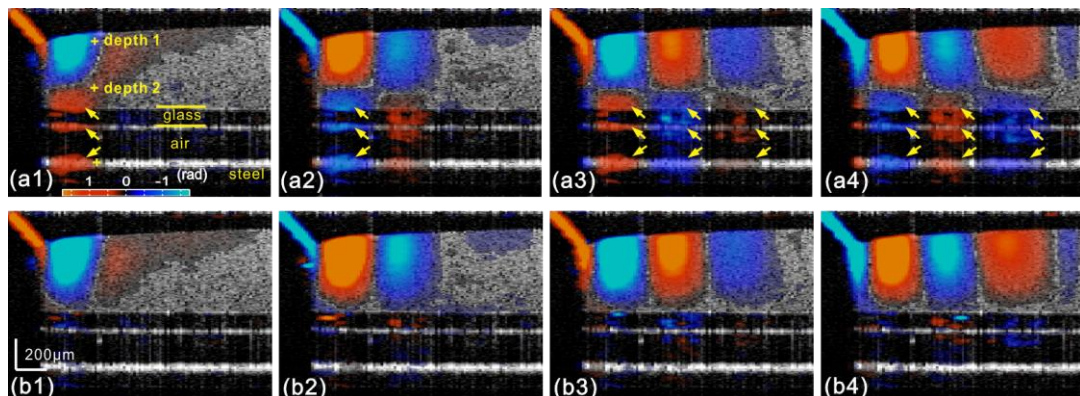


Figure 4-18 Shear wave imaging results for demonstrating the presence of surface ripple artefacts

(a1-a4) PhS-OCT detected displacement field, [(a1) $t=5T_s$ (a2) $t=10T_s$ (a3) $t=15T_s$ (a4) $t=20T_s$, T_s = sampling period]. (b1-b4) Compensated displacement fields. Same colourbar as shown in (a1) applies to each sub-figure

Before mapping the phase, a mask was applied to the phase image. The mask was generated from the structural image so that any pixel with low OCT signal intensity, e.g. from transparent structures, was masked out. This masking method was applied to all the phase images presented. Four snapshots of the dynamic wave (displacement field) are shown in Figure 4-18(a1-a4), each snapshot is noted by the time offset from $t=0$. The same applies to all the snapshot images. The bright line at the bottom of each image is the surface of steel plate. The phase artefacts are clearly indicated in these images, with smaller but opposite phase values to the surface phase, as indicated by arrows in Figure 4-18. This supports the analyses presented in the theoretical analysis of the artefact that a positive phase (motion) on a surface will cause a negative phase (artefact) at all locations underneath the surface. Hence, on the B-scan image, the stripe artefacts are created by the surface motion.

The phase compensation method was then applied on these wave field dataset. The results are shown in Figure 4-18(b1-b4). After compensation, the phase artefacts on the steel plate and also on the glass plate surface are eliminated. Leaving the corrected wave pattern to decrease to zero from surface to bottom of the phantom, as expected. Note that in this figure, there still exists phase signal (red or blue) within some region that is of low OCT signal. This is largely due to the imperfection of the masking method used. This however does not affect the demonstration of artefact compensation.

To show the strength of artefact, the displacement waveform at different depths are plotted in Figure 4-19, where the compensated and uncompensated waveform at three depths/locations (marked as “+” in Figure 4-18(a1)) are given. At depth #1, the vibration amplitude is the largest, as this location is close to the phantom surface where the artefact effect is less obvious. As the depth goes deeper to depth #2, both the phase and amplitude shows a severe distortion. Because in the deeper region, the true displacement becomes smaller while the artefact amplitude is uniform at all depths, the error rate increases significantly at deeper region. As shown at the bottom pair of

waveforms, there is no displacement signal on the steel plate after compensation as expected, which demonstrates the effectiveness of the compensation method.

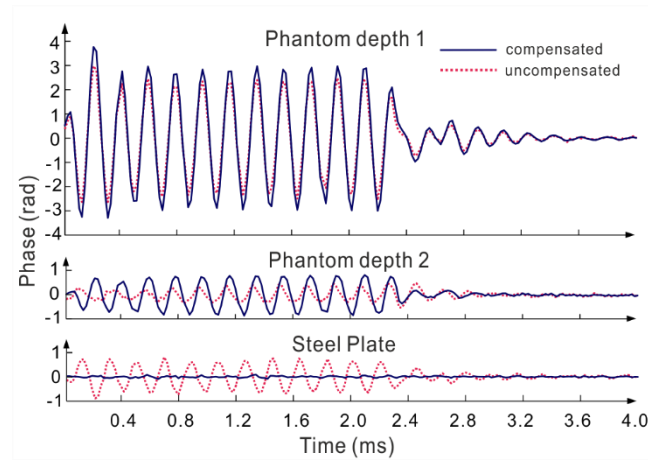


Figure 4-19 Displacement waveforms at three depths of the layered phantom

The artefact could lead to the apparent amplitude increase or decrease (see depth 2 and steel plate), or a certain phase shift (see depth 2). This is because the displacement waveform is independent on surface motion, which could be in different phase with artefact error. The composition of the true displacement and artefact will lead to those three situations above.

Validation of compensation algorithm

To further validate the artefact compensation algorithm, a numerical solution to the wave field in a homogenous phantom is created, the dimensions and physical parameters were set to mimic the soft phantom. The longitudinal wave (P-wave) and shear wave (S-wave) velocity were set to 1050 m/s and 2.5 m/s. The simulation modelled a homogenous phantom with a stimulation source emitting 3 cycles of 5 kHz sine waves on surface. A snapshot of displacement field (z direction component) is presented in Figure 4-20(a). In this figure to avoid any reflections, only a 2×3.5 mm section is shown, which is relatively far from any fixed boundaries. Figure 4-20(b) is the measured wave propagating pattern at the same time instance of the stimulation. Because the stimulation in the experiment was applied with a small angle, the wave front observed in the stimulation presents some difference from that in the simulation.

In general, the wavelength, amplitude and the wave pattern reached good agreements between the experiment and the simulation.

The result of simulation demonstrates the co-existing shear wave and surface wave (Rayleigh wave) modes. Rayleigh wave propagates on the free surface of media, with an active depth of about one wavelength. There is no strict division boundary between the bulk shear wave and Rayleigh wave. The wave field snapshot (Figure 4-20) indicates the shear waves with a wavelength of ~ 0.5 mm, and Rayleigh wave with a similar velocity. The displacement amplitude are in good agreement with that from prior literature about the amplitude map of shear waves generated by surface point source[148].

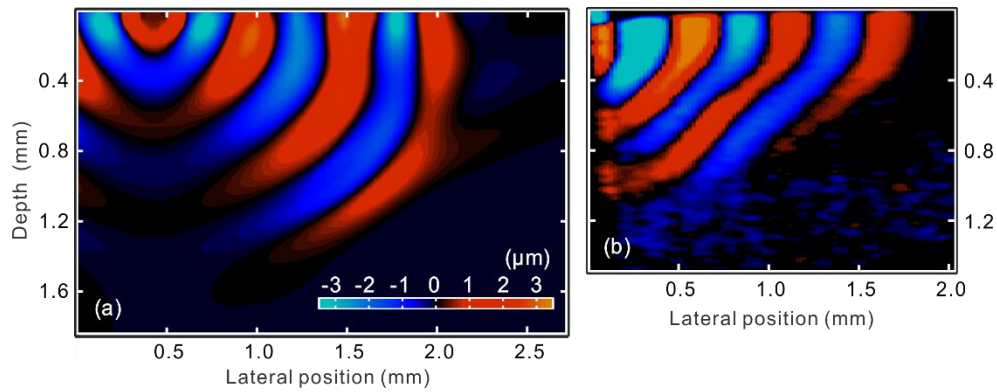


Figure 4-20 A snapshot of displacement field from the numerical simulation of shear waves in homogenous phantom. (a) A snapshot of displacement field from the numerical simulation, and (b) measured displacement field by PhS-OCT. The images are displayed at the same scale and time point.

As the wave pattern (spatial-temporal displacement field) is critical for the reconstruction of wave velocity map, the elimination of motion artefact has always been an important issue for all wave imaging modalities. Here, a homogenous phantom that is large enough is used to avoid reflected waves to show the pure shear wave images. As shown in Figure 4-17(b), the stimulation source is attached to phantom surface. Figure 4-21(a1-a4) show snapshots at 4 different time instants when the wave propagates within the phantom. The stripe artefacts are clearly noticeable in all the frames. Also in comparison with the theoretical wave pattern in Figure 4-20, the wave fronts exhibit obvious distortion. Figure 4-21(b1-b4) shows the wave field frames with

surface phase compensation. The stripe artefacts and wave distortion are effectively suppressed. The compensated wave pattern still shows a small difference when compared to Figure 4-20. This is, because the excitations are launched with an angle in the experiments, and also the attenuation is not modelled in the theoretical model. However, the phase images are much more realistic than the artefact-contaminated ones.

There is a circumstance where the artefacts can be mitigated without compensation. This is shown in Figure 4-17(c) where the phantom is placed in a container. Then a layer of mineral oil is poured onto the surface. To avoid the oil surface motion, the oil layer is covered with a thin glass plate. In this case, the oil layer works as an optical coupling media because the oil has a refractive index that is close to that of phantom, and there is no surface motion on the oil due to the glass plate. The measured wave patterns in this oil-covered phantom are presented in Figure 4-21(c1-c4). It can be seen that the images (without compensation applied) are basically artifact-free. However, as the mineral oil still exhibits a slightly higher refractive index than the phantom (~ 1.42 vs ~ 1.33), there exists an opposite stripes, i.e., a very weak amplitude stripe artefact with same phase direction could be observed [as indicated with arrows in Figure 4-21(c1-c4)]. This also confirmed the validity of the compensation method, because for this oil-phantom interface, $(n_2 - n_1)$ is a negative value, opposite to the case of air-tissue interface.

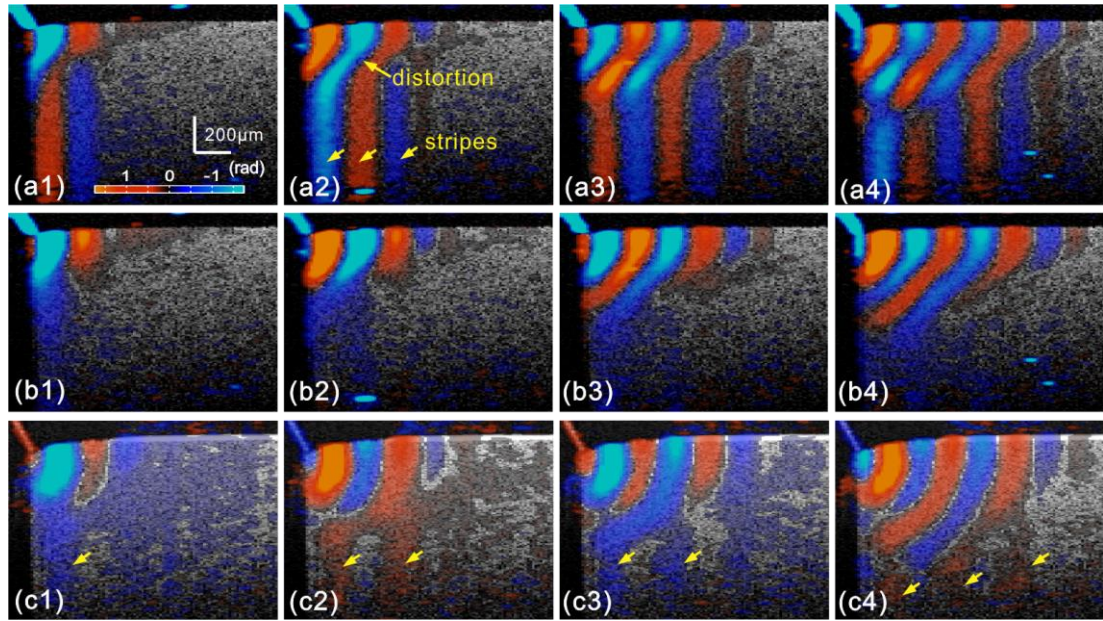


Figure 4-21 (a1-a4) Wave propagating pattern detected with PhS-OCT in a homogenous tissue phantom; (b1-b4) wave pattern after phase compensation; and (c1-c4) wave pattern in homogeneous phantom with a layer of oil above.

Shown are the snapshots at the time instants of $5T_s$, $10T_s$, $15T_s$ and $20T_s$ where T_s = sampling period, $23.4\mu s$. Same colour bar as shown in (a1) applies to each sub figure.

Discussion

In this section, the formation and characteristics of the surface ripple artifact are theoretically and experimentally proved, starting from the study of phase-resolved motion detection methods. Furthermore, a method of compensating for these artifacts is proposed accordingly. The artifacts are first observed on a phantom with a moving part and a static part, and then on a homogenous phantom with propagating shear waves and surface waves. For both the cases, the compensation method showed the ability to remove the stripe artifacts and correct the distorted waveforms. As the described circumstances are common in dynamic OCE methods, the compensation algorithm is expected to have wide applications. This investigation also suggests that special attention should be given to the phase errors whenever nonhomogeneous optical medium exists, as the varying refraction expresses a lens effect for phase.

In this work, the refractive index is considered constant and uniform in the specimen.

Although a complex sample with variation of refractive index would complicate the proposed compensation method, it is still reasonable to conclude that using a rough estimation of refractive index, most of the artifact errors could be eliminated, providing much a higher SNR than leaving this artifact uncorrected. Because the artifact amplitude is $(n - 1)$ times the surface displacement, the variation of refractive index has a small variation range in the same type of biological tissue.

One difficulty for this compensation technique is in the situation where the sample surface is uneven or rough. In this case, the optical path would become more complex, leading to complications for interpreting the results. As there already exist very effective algorithms to inversely compute the OCT beam path for refraction correction[149], it is feasible to use this compensation method based on the beam path corrections. However, it is more computation-intensive. Nevertheless, the method given above is only one possible approach for the artefact correction; more effective and robust approaches remain to be explored.

4.4.3. Pulse compression

For a further enhancement of the shear wave imaging by increasing the signal to noise ratio (SNR), and to improve the elastography map resolution by shortening the shear wave signal duration, a method called pulse compression is proposed. In this work, a digital pulse compression method is combined to the dynamic elastography technique to improve shear modulus estimation.

Pulse compression was first introduced for radar detection in the early 1960's [150, 151] and later extended to ultrasound applications[152]. The main idea is to improve axial resolution by shortening the signal duration and increase the signal-to-noise ratio (SNR) by spreading the instantaneous peak energy level over a longer period.

Pulse compression technique is proposed in this study to combine with shear wave imaging in order to: 1- improve the SNR of detected displacements induced in the sample, and 2- compress spatially and temporally the shear wave for better

reconstruction of shear modulus maps. For that purpose, a broadband frequency-modulated (chirp) mechanical excitation is generated and applied digital pulse compression to the resulting displacement field detected with PhS-OCT. The performance of this pulse compression scheme is evaluated by comparing the results to those from un-chirped excitation.

A demonstration of the chirp compression process is given in Figure 4-22. From Figure 4-22(a) we can see the initial chirp that is used to drive the actuator. Figure 4-22(b) shows the chirp that is repeated three times, as a stimulation source that is send into sample. Figure 4-22(c) gives the simulated, OCT acquisition of the displacement waveform, which is contaminated with high amplitude of white noise. Figure 4-22(d) shows the signal after pulse compression procedure. The amplitude of these three chirps, in order are 0.5, 0.4 and 0.3.

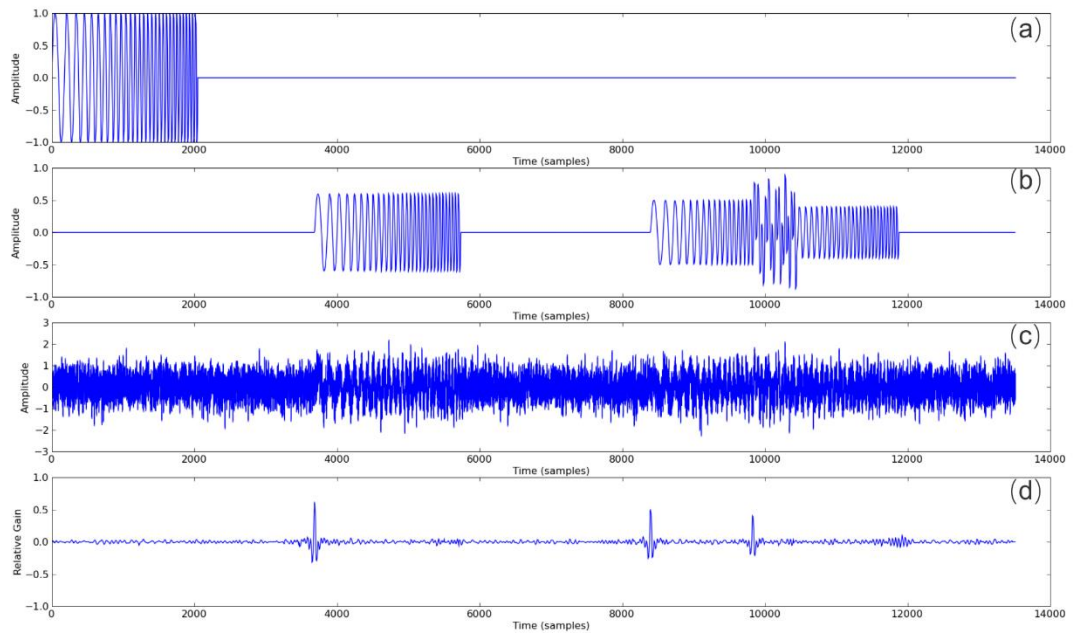


Figure 4-22 Chirp compression of a simulated signal

We can clearly see the chirps have been compressed around a center residing at the beginning of three instance of the detected signal, and resemble a positive spike at each chirp. The amplitude and location are clearly indicated in the compression result, with an effectively elevated SNR.

Pulse compression algorithm

Digital pulse compression is theoretically achieved by performing the autocorrelation of the displacement field. In practice, an inverse filter method is used to optimize the autocorrelation, mainly by reducing the side lobes of the autocorrelation function. The filter was designed using the following steps:

- 4) A reference signal $u_z^{ref}(x=0, t)$ is computed by averaging along depth the axial displacements at $x = 0$ (nearest point to the shear source).
- 5) An ideal output pulse $pulse(t)$ is derived from the autocorrelation of the reference signal:

$$pulse(\tau) = [u_z^{ref}(t) \otimes u_z^{ref}(-t)] * w(\tau) \quad [4.14]$$

where $w(\tau)$ is a weighting function designed to suppress side lobes of the autocorrelation function.

- 6) An inverse filter $f(\tau)$ is then designed by inverting:

$$[u_z^{ref}(t) \otimes u_z^{ref}(-t)] \otimes f(\tau) = pulse(\tau) \Leftrightarrow U_z^{ref}(\tau, \tau') \cdot f(\tau) = pulse(\tau) \quad [4.15]$$

where $U_z^{ref}(\tau, \tau')$ is the convolution matrix of the reference signal. The inverse filter is then applied to the autocorrelation of the axial displacement field at each location in the region of interest. This approach closely parallels that discussed in detail in [152] for conventional ultrasound imaging.

An example of a compressed pulse on a 0.5% agar phantom is shown in Figure 4-23, together with its corresponding inverse filter.

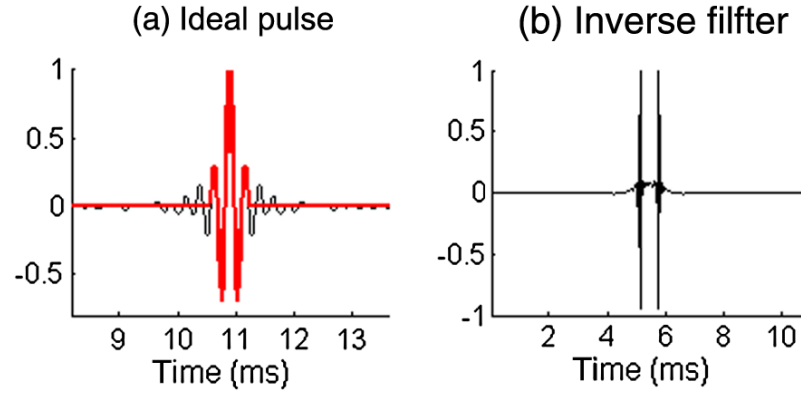


Figure 4-23 An example of a compressed pulse on a 0.5%-agar phantom.

(a) Ideal output pulse (red thick line) derived from the autocorrelation function (black line) as defined in Eq.[4.14] and Eq.[4.15]. (b) Inverse filter obtained from Eq. [4.15]

The original shear wave signal is a 1-7 kHz chirp, which last for 8 milliseconds. The shear wave signal has been compressed temporally and spatially, with a higher signal to noise ratio. The applications of pulse compression algorithm is presented in Chapter 5.3.3.

4.4.4. Directional filter

In the shear wave imaging data, the destructive interference of back-reflected waves, and refracted shear waves can degrade the quality of estimated wave velocity map that is derived based on the time-of-flight method[153]. In order to suppress this effect, the shear wave imaging data needs to be directionally filtered. Directional filtering is especially important when the shear waves were reflected in a sample that has hard inclusions.

The displacement data obtained from shear wave imaging is a function of lateral and axial position as well as time, i.e. a 3-dimensional data. The data is typically 256x512x255 in data size (width x depth x time), as shown in Figure 4-24(a). Each SWI data is regarded as a stack of lateral-temporal image slices, which were filtered separately.

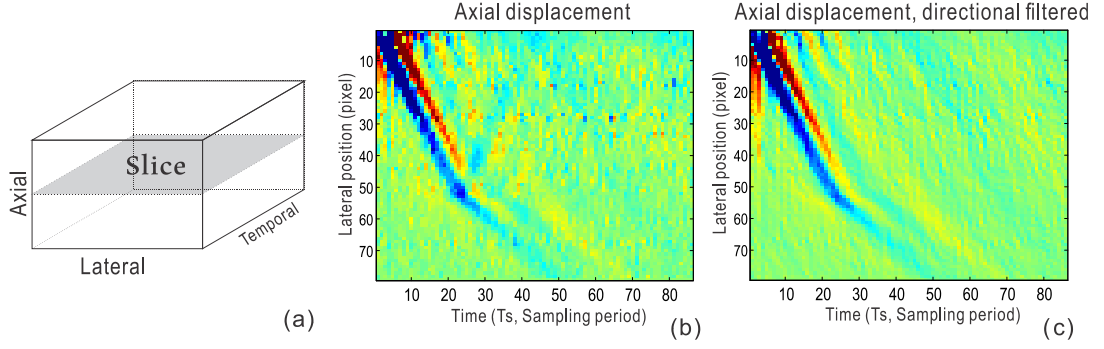


Figure 4-24 Directional filter process on one slice of SWI data

(a) Diagram of a slice from the 3D matrix of SWI axial displacement data (b) A lateral-temporal slice of the displacement of a propagating, pulse shear wave at depth 0.8 mm (c) the lateral-temporal displacement image after directional filtering operation.

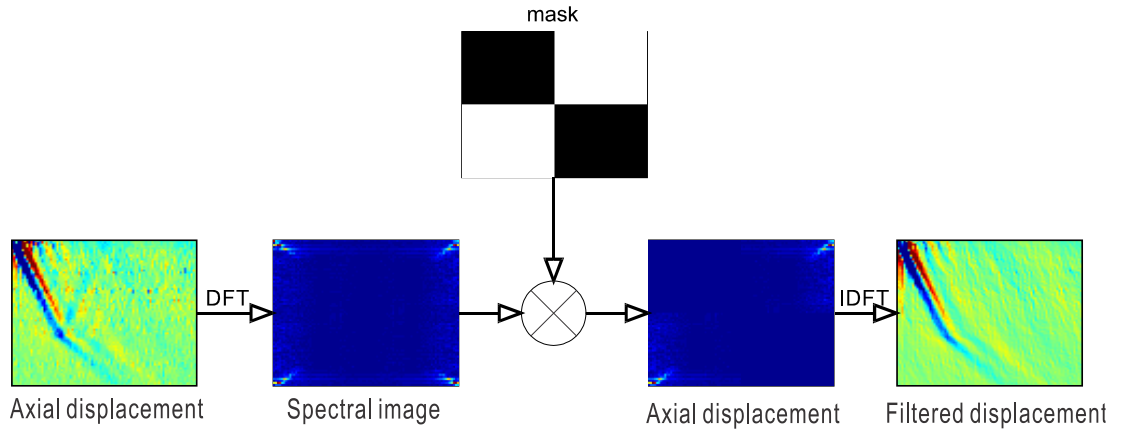


Figure 4-25 Directional filter processing workflow.

In Figure 4-25, the workflow for a directional filter is presented. The axial displacement at a specific depth (Figure 4-24) is presented in the wavenumber-frequency domain using a 2D discrete Fourier transform (DFT). Quadrants corresponding to negative shear wave speed are removed by multiplication with a binary mask. After inverse DFT (IDFT), the filtered axial velocity is obtained.

The 2D DFT of a lateral-temporal slice can be written as a function of wavenumber k and angular frequency ω with the phase velocity $c_s = \omega/k$. Therefore, the energy of the right-propagating shear waves lies in the first and third quadrants of the spectrum, where $c_s > 0$, whereas that of the left-propagating shear waves lines in the second and

fourth quadrants, where $c_s < 0$. The directional filtering is then accomplished by keeping only the desired quadrants in the wavenumber-frequency matrix for each slice, followed by inverse transformation to the spatial-temporal domain. Figure 4-25 illustrates the filtering procedure and demonstrates the wave propagating to the left are removed.

4.5. Conclusions

The design and construction of a PhS-OCT system is presented, according to the requirements for OCT shear wave imaging. The essential techniques that is developed for producing and optimizing the wave field images is also given in this chapter.

The PhS-OCT system is able to provide a structural imaging of up to 9 μm axial resolution and 5.1 μm lateral resolution, and dynamic range of 100 dB. The proposed protocol provides the motion detection of nanometre scale sensitivity and an ultra-high frame rate of up to 92 kfps. This provides a novel solution to capture the propagation of transient waves inside target OCT samples, with both high spatial resolution and high imaging frame rate, which is a necessary route for obtaining the elastography result with dynamic OCE.

Another significant contribution described in this chapter is the analysis of the source of imaging artefact and the algorithm for compensating the artefact. With a correct estimation of sample refractive index, the stripe artefacts can be removed, leaving an accurate image of wave field snapshot.

A technique for improving the signal-to-noise ratio in SWI results using coded wave excitation is also proposed. The outcome of this chapter is a technique to obtain high quality SWI images for OCE reconstruction in the subsequent chapter.

It is the hoped that the theoretical analysis and methods reported in this chapter will help improve the accuracy of OCT motion detection techniques and advance the developments of a wide range of related biomedical applications.

5. SHEAR WAVE OCE AND APPLICATIONS

5.1. Introduction

Given the shear wave imaging acquired from PhS-OCT, this chapter takes the final phase of this study: development of OCE algorithm and OCE application.

In This Chapter

- * Implementation of elastogram reconstruction methods are introduced, including time-of-flight method and wave inversion method, providing the algorithm to obtain localized shear modulus from shear wave propagation data.
- * OCE experiments on TMM phantoms, to validate the effectiveness and accuracy of SW-OCE. Different technique of wave generation has been tested, including the contact mechanical stimulation, acoustic radiation force impulse, and pulsed laser.
- * Effectiveness of pulse compression technique on improving OCE result accuracy is tested.
- * OCE experiments are carried on mouse tissue: *in vitro* Thiel mouse skin and *in*

vivo mouse cornea are measured for elasticity map.

5.2. Elastogram reconstruction

Shear wave speed is directly related to the linear elastic modulus of gels and soft tissues in which the Poisson's ratio approaches 0.5. For these materials, an incompressible elastic model can be assumed in which the shear modulus (μ) is simply proportional to the modulus of linear elasticity, i.e., the Young's modulus E , according to the expression $E=3\mu$. Measurement of either the Young's modulus, as in static elastography reconstruction routines, or the shear modulus fully characterizes the linear elastic properties of soft tissue. Consequently, reconstruction of the shear modulus from shear wave measurements can fully characterize the linear elastic properties of the soft tissue sample under study.

As shear wave elastography is based on the estimation of localized shear wave velocity, the shear wave speed estimation is a critical process in the elastogram reconstruction.

5.2.1. Time-of-flight method

For a locally homogenous medium (i.e. spatial variations of elastic properties occur on a larger scale than the shear wavelength), a shear wave at a specified frequency would travel with constant speed, i.e. the phase delay $\Delta\phi$ and distance along a wave path Δr is linear; thus,

$$C_s(\omega) = \frac{\omega \Delta r}{\Delta \phi} \quad [5.1]$$

Experimentally, the shear wave speed can be calculated using measurements of $\Delta\phi$ and Δr , i.e. the phase shift and distance that the wave traces at a specific location produce an estimate of the shear wave speed according to Eq. [5.1].

A number of points along a line can be used to specify the propagation path. The

displacement waveforms at these points are then analysed, generating a series of phase delays as a function of corresponding position offsets. Linear fitting to these phase delays produces the shear wave velocity according to Eq.[5.1].

Furthermore, to extend the speed estimation to 2-D mapping, a shear wave speed estimation procedure can be repeated for each target pixel, where the corresponding shear wave speed was determined on two reference pixels: By comparing the time-dependent axial displacement between the two reference pixels, the time taken for the shear wave to travel between them could be estimated, and taken as the local shear wave speed at the target pixel. As shown in Figure 5-1, the process of shear wave speed estimation is illustrated.

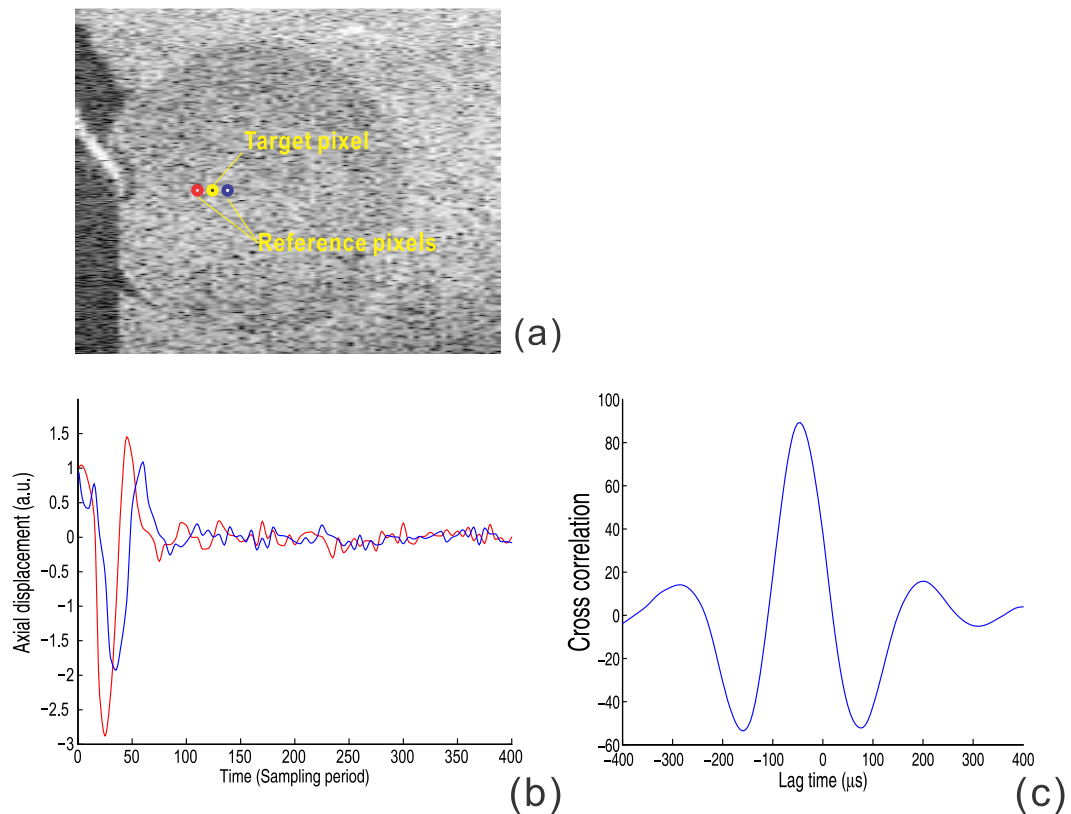


Figure 5-1 Shear wave speed estimation with time-of-flight cross correlation

- (a) The B-scan image around the target pixel, two surrounding pixels (red and blue) that is 3 pixels away from the target pixel at the same depth are considered. (b) Time-dependent axial displacement at the two reference pixels, after interpolation. (c) The correlation of the two waveforms, indicating the delay time, and thereby the speed.

The waveforms on two reference pixels, which are a few (typically 3~6) pixels away from the target pixel at the same depth, are plotted in Figure 5-1(b), forming a kernel. The shear wave estimation is performed in this “kernel”. The shear wave propagating from left to right would reach one of these two reference pixel (red) first. These axial displacement waveforms are interpolated by a factor of 5 using cubic interpolation to increase the temporal resolution of correlation. The two interpolated axial velocity functions were windowed with a symmetric Hanning window in order to reduce the effects of discontinuities at the first and last frames. Figure 5-1(c) shows the resulting cross-correlation of the two waveforms, for computational efficiency, only delays that would result in shear wave speeds above 0.6m/s were considered in the cross correlation. The delay that yielded the largest cross-correlation was considered as the propagation time between the reference points, denoted as Δt . For each pixel, this estimation process can be repeated for a few times, with a different reference distance (kernel size). The flowchart of this process is given in Figure 5-2. This process is repeated for each pixel in the B-frame, then forming a wave velocity map.

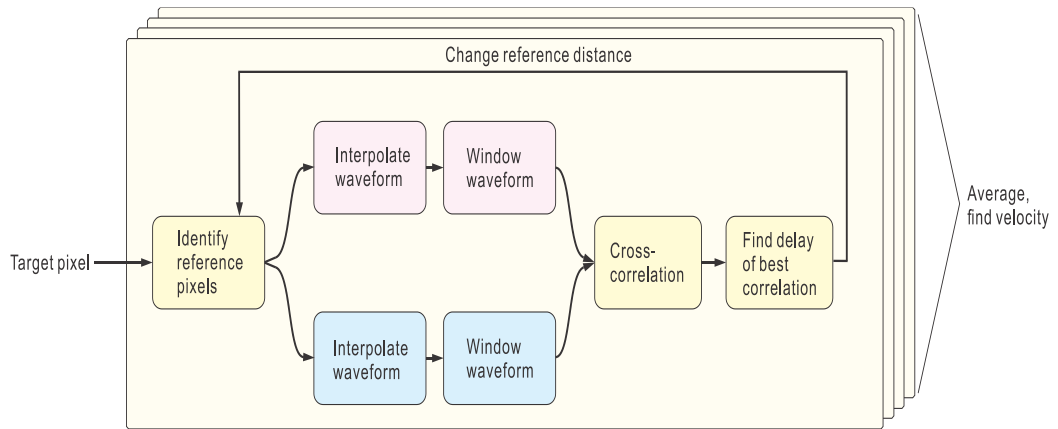


Figure 5-2 Flowchart of the speed estimation algorithm for a single pixel in 2-D shear wave velocity mapping.

5.2.2. Wave inversion method

To reconstruct the shear modulus map from shear wave processing, an inverse algorithm is needed. As the localized displacement field (\vec{u}) within the sample is captured, not only can the localized wave velocity be extracted at the specified wave

path using the method described above, but also the wave velocity map can be reconstructed by solving the wave propagation equation[111, 116]:

$$\rho \frac{\partial^2 \vec{u}}{\partial t^2} = \mu \vec{\nabla}^2 \vec{u} \quad [5.2]$$

This is a Helmholtz equation assuming that the medium is locally homogeneous and isotropic. Here μ is the shear modulus, and ρ is the density. By transforming the displacement vector \vec{u} into its three components, Eq.[5.2] takes the form:

$$\frac{\partial^2 u_i}{\partial t^2} = \frac{\mu}{\rho} \left(\frac{\partial^2 u_i}{\partial x^2} + \frac{\partial^2 u_i}{\partial y^2} + \frac{\partial^2 u_i}{\partial z^2} \right), i = (x, y, z) \quad [5.3]$$

As dynamic wave data obtained from PhS-OCT represent one component of the displacement field along the direction of the probe beam (u_z), two of the three second-order spatial derivatives can be calculated in the imaging area (xz-plane). In the configuration of this study, since the out-of-plane width of the shear wave is far larger than the elevation thickness of the OCT imaging plane, the out-of-plane displacement (u_y) is nearly constant over the slice thickness and variations in this displacement component can be ignored in the region of interest; thus,

$$\frac{\partial^2 u_z}{\partial y^2} \ll \frac{\partial^2 u_z}{\partial x^2} + \frac{\partial^2 u_z}{\partial z^2} \quad [5.4]$$

and Eq.[5.3] simplifies to:

$$\frac{\partial^2 u_z}{\partial t^2} = \frac{\mu}{\rho} \left(\frac{\partial^2 u_z}{\partial x^2} + \frac{\partial^2 u_z}{\partial z^2} \right) \quad [5.5]$$

Assuming the attenuation of acoustic waves in the frequency range of interest is small, the relationship between shear modulus and shear wave velocity can be simplified to:

$$\mu = \rho V_s^2 \quad [5.6]$$

where V_s is the shear velocity computed as the square root of the ratio between temporal and spatial second derivatives, which are available from the u_z images estimated in the experiment. Multiplexing these equations, the local shear modulus is then reconstructed as:

$$\mu(x, z) = \rho \frac{1}{N} \sum_{n=1}^N \frac{\left(\frac{\partial^2 u_z}{\partial t^2} \right)_{x,z}}{\left(\frac{\partial^2 u_z}{\partial x^2} + \frac{\partial^2 u_z}{\partial x^2} \right)_{t=nT}} \quad [5.7]$$

where T is the B-frame sampling period, and N is the total frame number. The computational power required for this inversion algorithm is much lower than that needed for previous phase-resolved OCE methods. The post processing is tested on a standard dual-core 3.3 GHz PC, the reconstruction of the 2D spatial elasticity map from displacement data took ~5 seconds.

The wave inversion method for estimating localized shear wave velocity offers the advantage of short computation time and no *a priori* assumption about shear wave propagation direction needs to be made when analysing a given region of dynamic displacement data. However, as Eq.[5.7] indicates, second-order spatial and temporal derivatives of displacement are required for the shear wave speed reconstruction. Given the noise that presents when obtaining the dynamic displacement field, appreciable filtering and smoothing of this displacement data must be performed before processing, which will certainly induce a decrease in the elastogram resolution and sensitivity.

5.3. Elastography experiment on tissue-mimicking phantoms

Following the last chapter, where a shear wave imaging OCT (SWI-OCT) system has been proposed to track the shear wave propagation in OCT imaging samples, the local estimates of shear wave speed obtained from tracking results can image the local shear modulus. This shear wave optical coherence elastography (SW-OCE) method has been examined for its performance in a series of experiments and the results were discussed in this section.

A few types of tissue mimicking phantoms are made, which are designed to present an elasticity variation in axial and transverse directions. Three types of mechanical wave generation methods were also tested, including the direct, easy achievable contact mechanical stimulation, the remote, acoustic radiation force impulse stimulation, and non-contact, laser pulse based shear wave generation. The experiment set up for each type of wave stimulation are briefly introduced, thereafter results of shear wave imaging are presented, and analysed for shear wave propagation, providing SW-OCE results of phantom inclusion dimensions and shear modulus. The OCE results are compared with practical expectations of stiff inclusion boundary locations and literature values of shear modulus, to calibrate and assess the accuracy of SW-OCE technique. The results presented in this section are published in a journal paper [J-2].

5.3.1. Mechanically induced shear wave OCE

Experimental arrangements

Figure 5-3 shows a schematic of the system used to generate and detect induced shear waves. It includes: (a) a piezoelectric actuator and driving system to generate mechanical waves propagating within the sample, and (b) a PhS-OCT system to detect and record mechanical displacements.

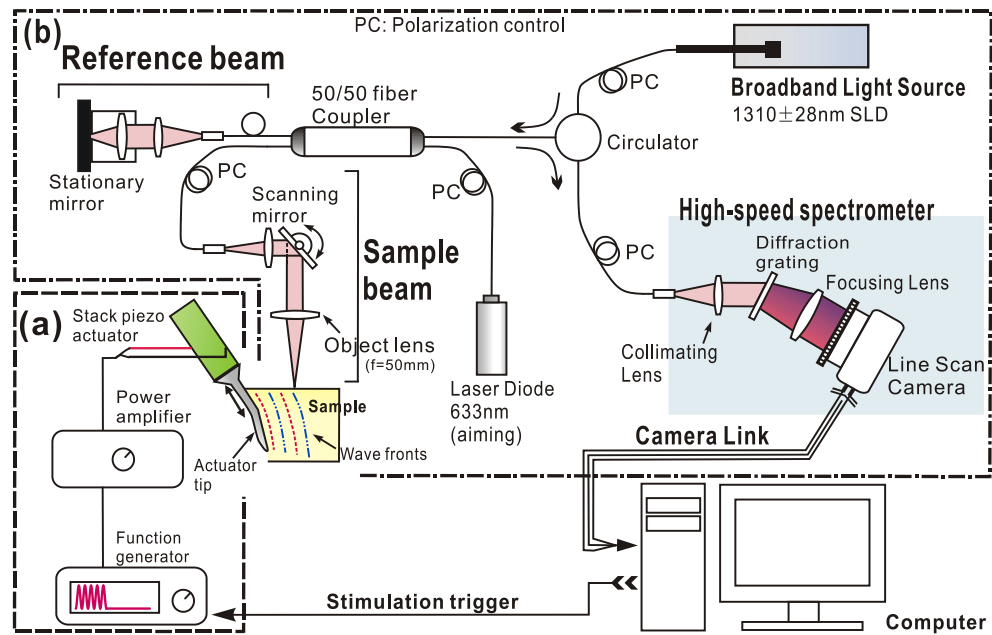


Figure 5-3 Schematic of system for SWI-OCT for mechanically induced shear waves

A low-voltage, stacked piezoelectric actuator (Thorlabs, Newton, USA) was used to induce a displacement of $15\ \mu\text{m}$ at a maximum input voltage of 100 V. The external mechanical load is a six-cycle tone-burst at 5 kHz. This quasi-continuous wave provides higher signal-to-noise ratio (SNR) for the specified frequency compared to that of a broadband stimulus of the same magnitude. During experiments, the maximum actuator displacement was restricted to $5\ \mu\text{m}$, with the typical wave amplitude within the specimen less than $3\ \mu\text{m}$. With such small strain magnitude, the tissue-like specimen can be considered linear, thus avoiding the complexity of potential elastic non-linearities within soft tissue. A power amplifier (AE Techon, Elkhart, USA) with a controllable voltage gain was used to optimally drive the actuator's capacitance.

A slender stainless steel rod with a small polished tip was fixed to the actuator as the contact to the sample. The tip was in a wedge-shape with a width of 1.7mm, so that the waves generated by this tip is considered as planar waves since this width is much larger than the wavelength. The actuator assembly was then mounted to a precision positioning stage, enabling precise advancement of the actuator-tip to gently contact

the specimen at the side (see Figure 5-3). The contact between the specimen and the actuator-tip was also visualized in real-time by the OCT system (see below in Figure 5-4), which helped ensure consistent stimulation conditions for all measurements.

Phantom preparations

Agar is an easily accessible material that can be used to produce tissue phantoms with controllable mechanical properties similar to those of human soft tissue[154]. By increasing agar concentration, we prepared a series of agar-agar phantoms to mimic the Young's modulus (shear modulus) in soft tissue such as within the anterior segment of the eye. To produce these phantoms, the proper amount of agar-agar powder (Fisher Scientific Inc., USA) was stirred into boiling distilled water until completely dissolved. Before casting into an 8 mm high, 50 mm diameter petri dish, a few drops of milk were added as scattering particles to facilitate OCT detection. We made the specimens with agar-agar concentrations between 0.5% - 2% (W/V), producing phantoms that could be easily handled mechanically for the studies presented below.

Results

Shear wave imaging experiments were performed on a series of tissue-mimicking phantoms with agar-agar concentrations of 0.5%, 0.75%, 1%, 1.5%, and 2% (W/V), respectively. Guided by real-time structural images provided by PhS-OCT, the phantom was advanced by a translation stage so that the actuator-tip was mechanically coupled to the phantom surface at the side (See Figure 5-3). One typical image of the displacement field, overlaid onto the structural image of the phantom, is presented in Figure 5-4.

With the stimulation source generating a 5 kHz mechanical wave, shear wave phase images from the different agar-agar phantoms showed wave patterns of varying wavelength. Typical patterns from four phantoms are shown in Figure 5-5(a-d). Differences in wavelength are clearly distinguishable between each specimen, demonstrating differences in wave velocities, thus the stiffness. We note that because free boundaries are very close to the shear wave source, induced mechanical waves are

most likely Rayleigh-like with mixed longitudinal and shear components. For this geometry, the estimated propagation speed is closer to that of Rayleigh waves. As Rayleigh waves exhibit slower propagation speeds than bulk shear waves, the simple analysis presented above for bulk shear waves likely underestimates the shear wave speed by about 5%. However, this estimate can be used to compare relative values of shear modulus between different materials.

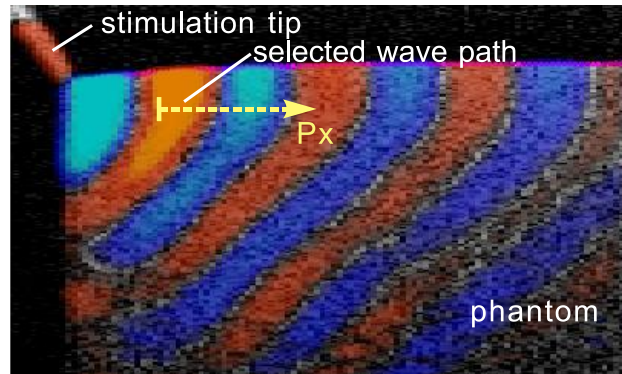


Figure 5-4 Displacement field overlaid onto structural image of a homogenous phantom

To calculate the shear wave velocity in the phantom with the time-of-flight method, a wave propagation path with a known direction needs to be defined. The target shear wave paths are selected near the sample surface and about one wave length in depth, where the wave propagation direction is nearly horizontal. For every pixel on this wave path, temporal displacement data are taken for analysis. As an example, wave traces on the path shown in Figure 5-4 are plotted in Figure 5-5(e). By calculating the phases at 5 kHz frequency of each wave trace, the phase delay versus offset distance from the first point is shown in Figure 5-5(f). The slope, $\Delta r / \Delta \phi$ resulted from linear fitting is then calculated to solve Eq.[5.1] for wave velocity C_s .

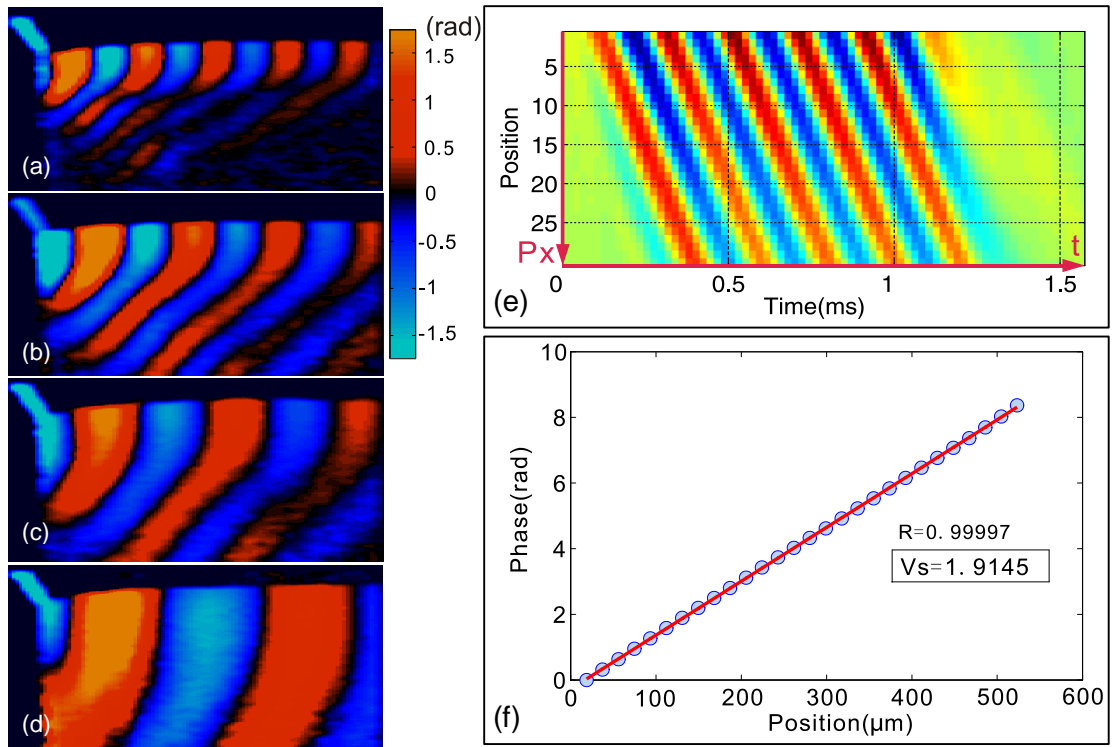


Figure 5-5 (a-d) Wave propagation pattern in agar phantoms with agar concentration: (a) 0.5%, (b) 0.75, (c) 1% and (d) 2%, respectively. (e) Wave traces along the specified wave propagation path shown in Figure 5-4 as 'Px'. (f) Linear fitting of the phase delays vs. position offsets from the first point.

Figure 5-6 shows the reconstructed shear modulus map for an agar phantom with 0.5% agar concentration. The shear modulus map (color scale) is superimposed on the B-scan (gray scale). The shear modulus is displayed wherever the correlation coefficient of the linear fitting is greater than 0.99. The median shear wave speed across the imaging plane is estimated to be 1.8 ± 0.5 m/s, corresponding to a shear modulus of 3.28 ± 1.77 kPa.

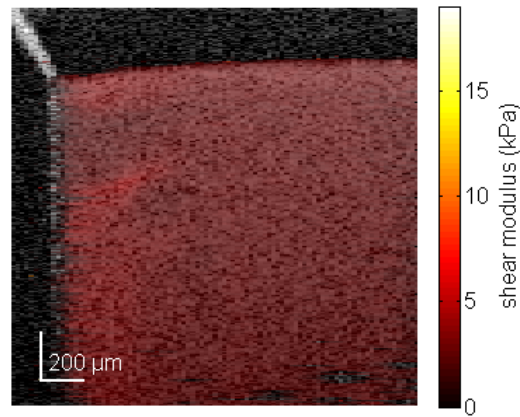


Figure 5-6 Shear modulus map of a 0.5% agar phantom reconstructed using SW-OCE

In Figure 5-7 measured shear wave velocities in agar-agar phantoms are presented, along with results extracted from prior literature[154]. Note that the prior method used magnetic resonance elastography to estimate shear wave speed at an excitation frequency of 400 Hz for the results presented in Figure 5-7. We performed repeated measurements on each specimen ($n=5$) to provide a conservative estimate of standard deviations (SDs), as shown by the error bars in this figure.

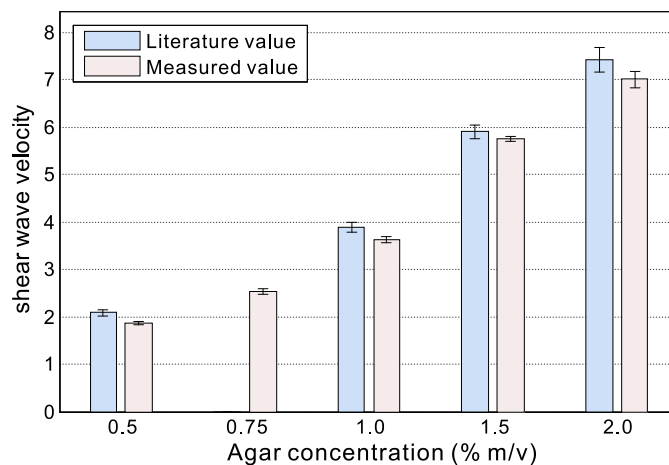


Figure 5-7 Measurement results of shear wave velocity in agar phantom

The measured shear wave velocities generally agreed well with literature values: the deviation is smaller than 6% of the shear wave speed for the different agar concentrations. This value is comparable to the standard deviation of the experimental

measurements, which is $\sim 5\%$ of the shear wave speed. The consistent underestimation also can be a result of measuring the velocity within about one wavelength of a free surface where Rayleigh wave effects tend to reduce the apparent wave velocity. In any event, the results presented in Figure 5-7 are very precise (i.e., small measurement errors) and match well with literature values for shear wave speed in similar agar gels.

In Figure 5-8, the structural image of an agar phantom with a cylindrical inclusion is presented. The inclusion was $\sim 500\ \mu\text{m}$ in diameter and made of 1% agar solution, while the background was made of 0.5% agar. In the B-mode OCT image (Figure 5-8), the boundary of the hard inclusion is barely visible, as indicated by the dotted line. However, the stimulation tip attached to the left side of the tissue-mimicking phantom is clearly visible.

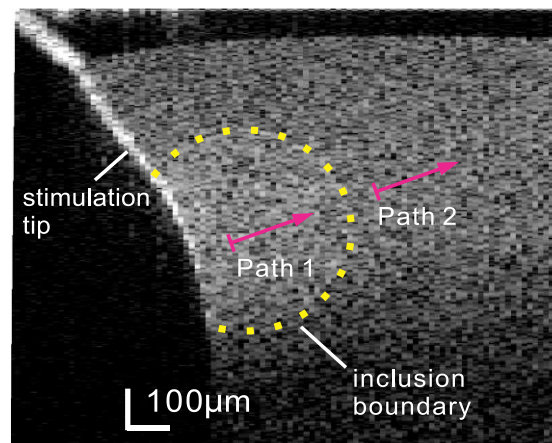


Figure 5-8 B-mode structural image of agar phantom with inclusion

After processing M-B scan data, the B-frame sequence of displacement maps was generated, i.e., full wave propagation data. Typical phase frames are presented in Figure 5-9(a-d) at different time points, where propagation of shear waves can be observed.

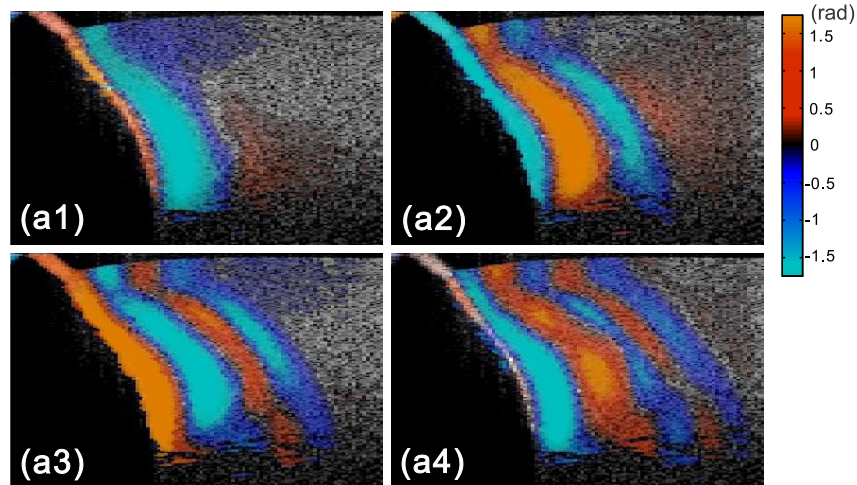


Figure 5-9 Displacement field snapshots at a evenly sampled time points

(a) $T=2T_s$, (b) $t=4T_s$, (c) $t=6T_s$, (d) $t=8T_s$, (T_s = sampling period, $23.4 \mu s$)

A major benefit of directly visualizing these wave patterns is that the wave propagation direction at specific locations can be easily identified as the normal to the displacement front. This facilitates the extraction of shear wave velocity using the time-of-flight method. Two propagation paths were selected, as shown in Figure 5-8, each containing 20 wave traces. For each path, time-of-flight method is used to estimate the wave velocity, as shown in Figure 5-10(a). The shear wave velocity was calculated by linear fitting to these curves, yielding 1.71 m/s and 4.13 m/s in path 1 and 2 (Figure 5-8), respectively. These results are in good agreement with the wave speeds found in equivalent gels (c.f. Figure 5-7). By substituting these values in Eq.[3.15], the shear moduli in these two regions are 2.92 kPa and 17.06 kPa, respectively. Note that these two paths are located respectively in the hard inclusion and soft background.

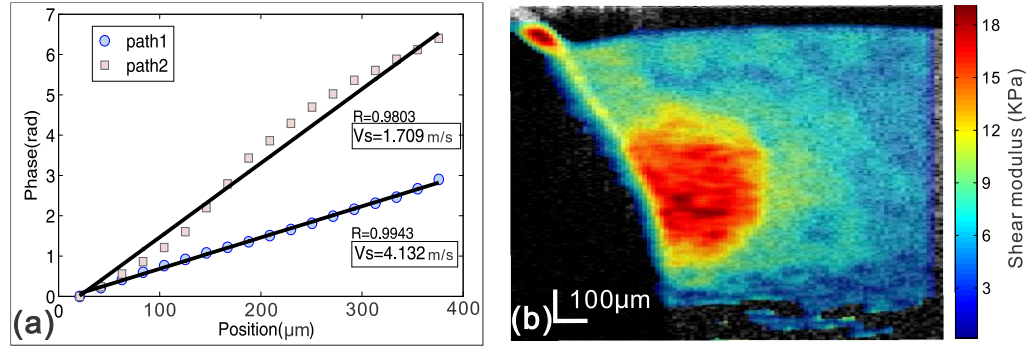


Figure 5-10 (a) Linear fitting of phase delays vs. position offsets for two selected wave propagation paths. (b) Quantitative map of shear modulus (μ) computed from dynamic shear wave visualization

To obtain a quantitative shear modulus map in the measured phantom, we applied the reconstruction algorithm to all spatial-temporal wave propagation data. The result is shown in Figure 5-10(b) with the shear modulus color-coded and overlaid onto the grey-scale structural image using precisely the same display dynamic range as that of Figure 5-6. In the region near the contact with the stimulation tip, the shear modulus value is not accurate because the simple wave equation of Eq.[5.5] is not applicable in the immediate source region. Overall, this image clearly demonstrates the capability of the current approach to differentiate stiffness within mechanically heterogeneous tissue. The position and shape of the inclusion are clearly visible, with the boundary matched well with its expected location. The lateral resolution of the shear modulus map is affected by two main factors. First, the linear fitting of the phase delay curve is performed over $\sim 500 \mu\text{m}$. Second, the shear wave can be diffracted by the inclusion. By comparing shear modulus values with the time-of-flight method, consistency is maintained in both the stiff lesion region ($\sim 17 \text{ kPa}$) and the homogenous background ($\sim 3 \text{ kPa}$).

Discussion

The shear wave OCE technique combining acoustic biomechanical analysis and remote PhS-OCT measurement of dynamic displacement fields were employed. . Using the time-of-flight method, i.e., analyzing phase delays vs. distance travelled by the dynamic wave, the shear wave velocity in the specimen can be calculated to

provide quantification of the shear modulus. Through simple algebraic inversion of the wave equation, we have shown that tissue elasticity can be successfully mapped.

Shear wave imaging offers a new way to measure the localized shear modulus, while OCT provides a complementary structural image of the same tissue. The ability to measure the localized shear modulus in conjunction with morphology at high resolution has significant advantages over conventional ultrasound or MRI methods for those applications where OCT represents an appropriate imaging modality.

5.3.2. Ultrasonically induced shear wave OCE

Experimental arrangement

The sample is illuminated from the top while the US transducer is placed at the bottom. The US transducer was mounted on two linear translation stages so that the shear source could be swept across the sample. Echographic coupling gel was placed at the bottom of the sample to enable US propagation as well as at the top of the sample to avoid strong US reflection at the sample surface. The US transducer was accurately positioned by emitting low-energy US bursts and by visualizing in real-time OCT the resulting phase changes to detect and localize the US waves.

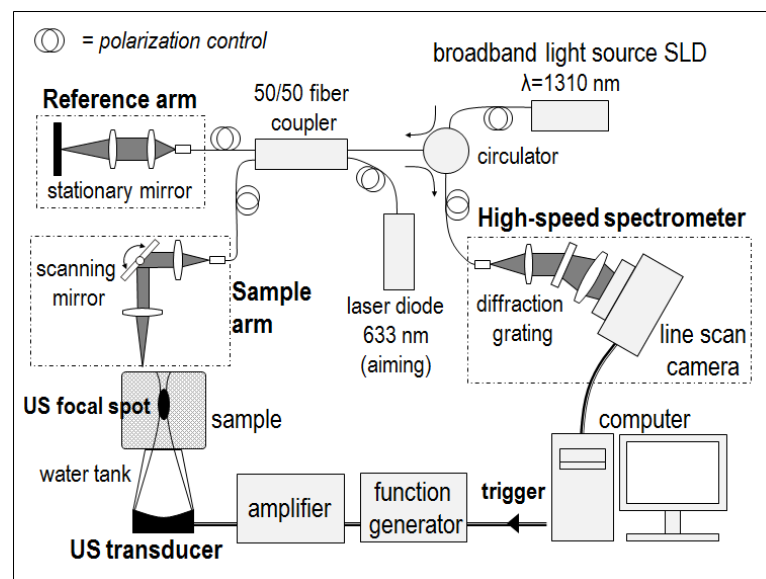


Figure 5-11 Experimental setup for shear wave elastography combining a PhS-OCT system with US radiation force

The layer of echographic gel placed at the top of the phantom also helps to reduce surface artifacts in the OCT imaging. Surface ripple artifacts can indeed occur due to the refractive index difference at the air-sample interface when the interface moves axially, as described in [18]. In addition, an echographic gel layer with a thin cover glass is applied on the phantom top surface to ensure a complete removal of that artifact.

The experiments were carried on agar phantoms, different agar concentrations provide a range of phantom stiffness. Latex nanospheres (0.3 μm diameter, 10% weight/weight solution, Duke Scientific Corporation, Palo Alto, CA, USA) were added to the phantoms as optical scatterers, providing sufficient backscattered signal to reach a 2 mm imaging depth.

Results

Axial displacements induced by US radiation force and detected by PhS-OCT in a homogeneous agar phantom are displayed in Figure 5-12(a) for different instants, showing the propagation of the shear wave front. As shown in Figure 5-12(b), measured displacements have an amplitude of 0.6 μm close to the shear source and a wide spectrum ranging from 200 Hz to a few kHz. The shear wave has a spatial resolution of ~ 1 mm (one shear wavelength). The axial displacements were detected with a signal-to-noise ratio of ~ 21 dB. For this acquisition, the lateral and axial resolution of the OCT image were respectively 58.5 μm and 4.15 μm .

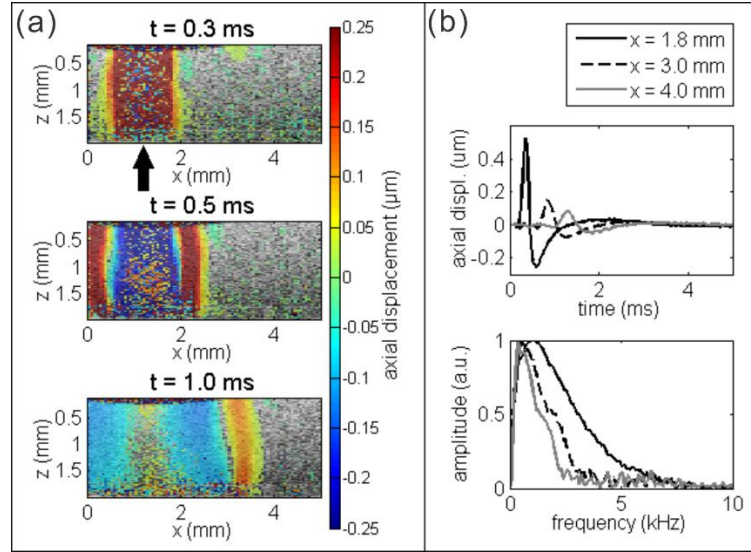


Figure 5-12 Shear wave imaging results of ultrasonically induced shear waves

(a) Snapshots of shear wave propagation at different time steps (the US emission starts at $t = 0$ ms and lasts 0.1 ms) in a homogeneous agar phantom. The black arrow indicates the lateral position of the US beam. (b) Temporal profile (top) and spectral content (bottom) of the displacement field averaged over the sample depth at different lateral positions.

Figure 5-13 illustrates the shear modulus map reconstructed for a 0.5% agar phantom. Correlations are performed in the spatio-temporal plane (Figure 5-13a), leading to the shear wave propagation speed that is then converted to the shear modulus using [3.15]. The dashed line in Figure 5-13(a) and Figure 5-13(b) delineates the near field of the shear source (distance smaller than a shear wavelength) where shear modulus estimation is biased by the coexistence of longitudinal, transverse and coupling modes. A threshold is applied on the shear modulus display: only correlations with a coefficient above 0.9 are considered.

Repeated measurements ($N = 5$) were carried on a 0.5% agar phantom. For each measurement, the spatial heterogeneity of the shear modulus map was found to be smaller than 10% of the shear modulus. The shear modulus was estimated to be 5.5 ± 0.3 kPa (median value \pm inter-experiments deviation).

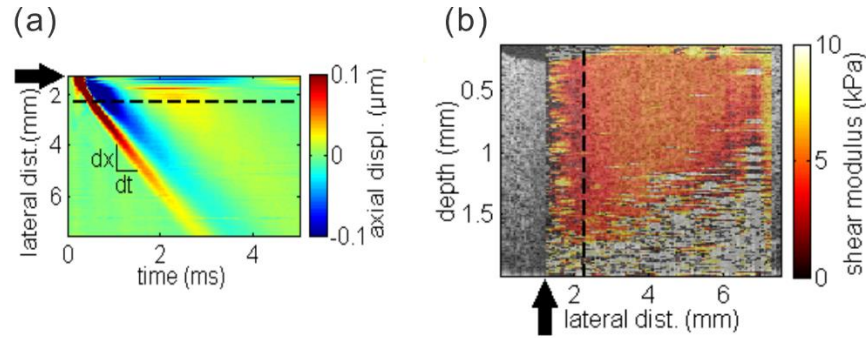


Figure 5-13 Shear wave speed estimation and elastogram reconstruction on SWI result

(a) Spatial-temporal representation of axial displacements at a given depth. The correlation of two rows distant from dx gives the travel time dt yielding the local shear wave speed $C_s = dx/dt$. (b) Reconstructed shear modulus map (colour scale) of a homogeneous 0.5% agar phantom superimposed on the B-mode image (grey scale). In both figures, the black arrow indicates the lateral position of the US beam and the dash line delineates the near field of the shear wave.

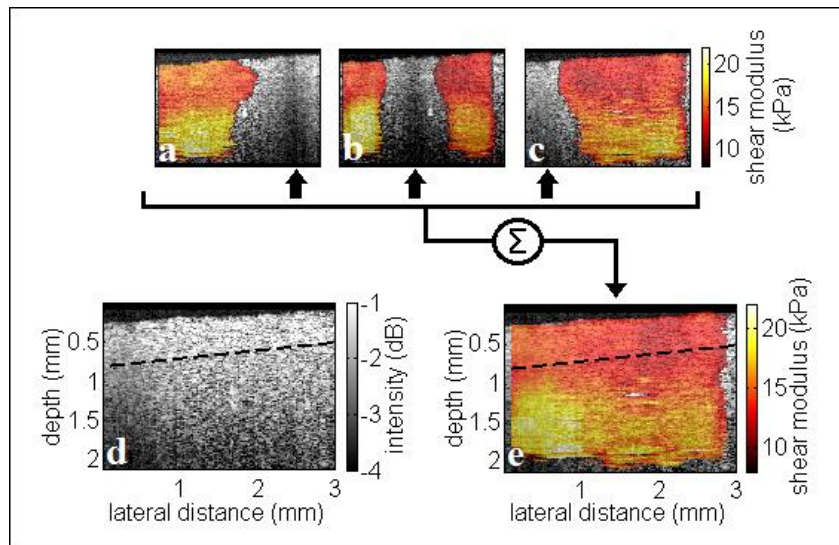


Figure 5-14 Results obtained on a bi-layered phantom in ARF-SW-OCE

(a) Partial shear modulus maps reconstructed from shear waves generated at different locations. Shear modulus maps (color scale) are superimposed on the B-mode image (gray scale). The black arrows indicate the lateral position of the US beam. (b) B-mode image of the phantom, made of a 1%-agar top-layer and a 2%-agar bottom-layer. The dash line delineates the boundary between both layers. (c) Shear modulus map obtained from the combination of the partial maps shown in (a).

The case of a heterogeneous, bi-layered, phantom is then considered as the specimen. The top and bottom layers were respectively made from a 1% and 2%-agar solution. For this experiment, the lateral and axial resolution of the OCT image were respectively $23.4\ \mu\text{m}$ and $4.15\ \mu\text{m}$. The thickness of the top layer is about 0.5 mm. Figure 5-14 shows a B-mode image of the phantom. The dash line delineates the boundary between both layers. The US beam was placed at three different lateral locations and each of the corresponding acquisitions yield a partial shear modulus map (Figure 5-14a-Figure 5-14c). The partial maps were then recombined to reconstruct a shear modulus map across the whole imaging plane (Figure 5-14e). A weight based on the correlation coefficient was applied for the recombination. The shear modulus was estimated to be $13.1 \pm 0.1\ \text{kPa}$ for the top layer and $16.6 \pm 0.4\ \text{kPa}$ for the bottom layer (median value \pm spatial variance). One should note that the soft region (red) of the elastic map extends below the top layer boundary, due to a limited axial resolution of the shear wave. However, the shear modulus map is able to clearly identify the elastic heterogeneity whereas the B-mode image does not exhibit any significant contrast. Besides, the B-mode images acquired simultaneously to the US emission exhibit a low-intensity region corresponding to the US beam location (Figure 5-14a-Figure 5-14c).

Discussion

In the tests described above, the feasibility of combining US radiation force and PhS-OCT to perform non-contact shear wave elastography measurements and obtain cross-sectional maps of the shear modulus of tissue-mimicking phantoms are demonstrated. The use of a US radiation force is a great improvement to previous systems using a mechanical actuator primarily because shear waves can be generated efficiently at depth. This could be particularly valuable to characterize the elasticity of the peripheral vasculature or the intraocular lens where contact shear sources cannot be applied. In addition, it provides good reproducibility compared to mechanical actuation which can be biased by contact issues. In this experimental configuration, the obtained shear wave are $\sim 1\ \text{kHz}$ in central frequency, leading to a millimetre lateral resolution of the shear modulus map in soft tissues that have a typical shear wave speed of a few metres per second. The shear wave central frequency (and thus the lateral resolution) can be

increased by varying the US emission central frequency or duration. The pulse compression technique can also be used to elevate the spatial resolution.

5.3.3. Pulse compression optimized SW-OCE

As introduced in Chapter 4.4.3, chirp compression is an effective algorithm to elevate the SNR of detected shear wave signal, with the objective of improving the reconstruction of shear wave velocity map.

The pulse compression algorithm has been applied to both mechanically induced shear waves and ultrasonically induced shear wave imaging. The performance of this pulse compression scheme is evaluated by comparing the results to those from monochromatic excitation, the reconstructed shear modulus map is also compared and discussed.

Pulse compression of mechanically induced shear wave

Figure 5-15 shows the broadband displacement field detected in a 1%-agar phantom resulting from an 8-ms long chirp excitation. As illustrated by Figure 5-15(a), the shear wave propagates laterally (from the left to the right) with lower frequencies (i.e. larger wavelengths) at early times and higher frequencies (i.e. smaller wavelengths) at later times. The signal-to-noise ratio (SNR) was computed from the spectrum of the displacements at one location (Figure 5-15(b)) as the ratio between the energy contained in the [1 - 5] kHz range and the energy out of that range. For this example, the SNR was estimated to be 10.2 dB.

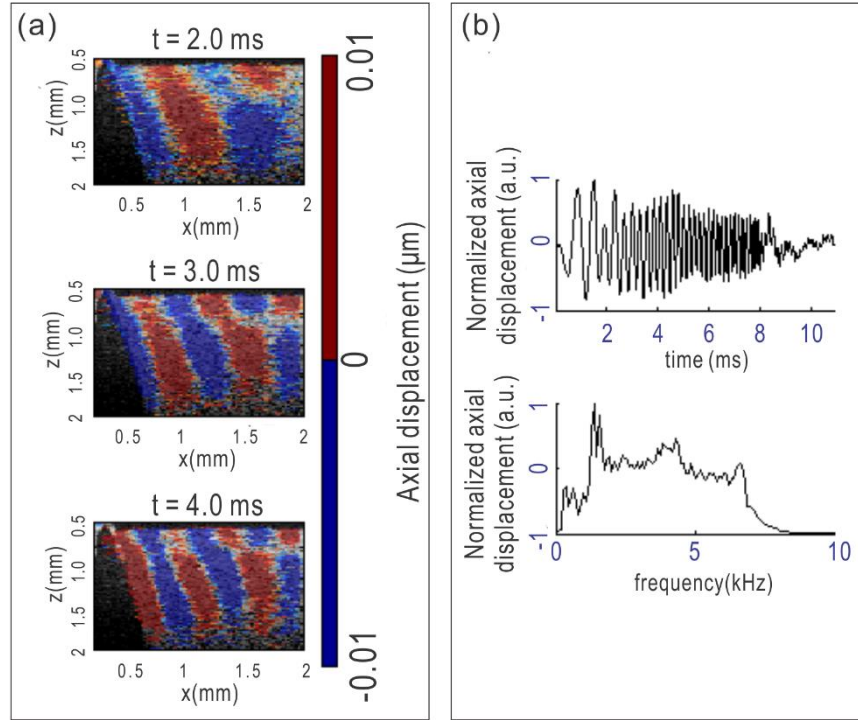


Figure 5-15 Displacement field in a 1% agar phantom resulting from a chirp excitation.

(a) Axial displacements (colour scale) superimposed on the B-mode image (grey scale) at different instants. (b) Normalized axial displacements profile (upper) and spectrum (lower) at one location.

The distortion of the displacement field at the phantom surface are probably due to interferences between surface waves and bulk shear waves, which propagate with slightly different speeds. Thus, the surface region was not considered for pulse compression.

Figure 5-16 shows the result of pulse compression performed on the data shown in Figure 5-15. The initial displacement field has been spatially and temporally compressed to a short broadband pulse of 1 ms duration. The SNR was estimated to be 23.0 dB from the spectrum shown in Figure 5-16(b), which corresponds to a 12.8 dB increase compared to the initial chirp.

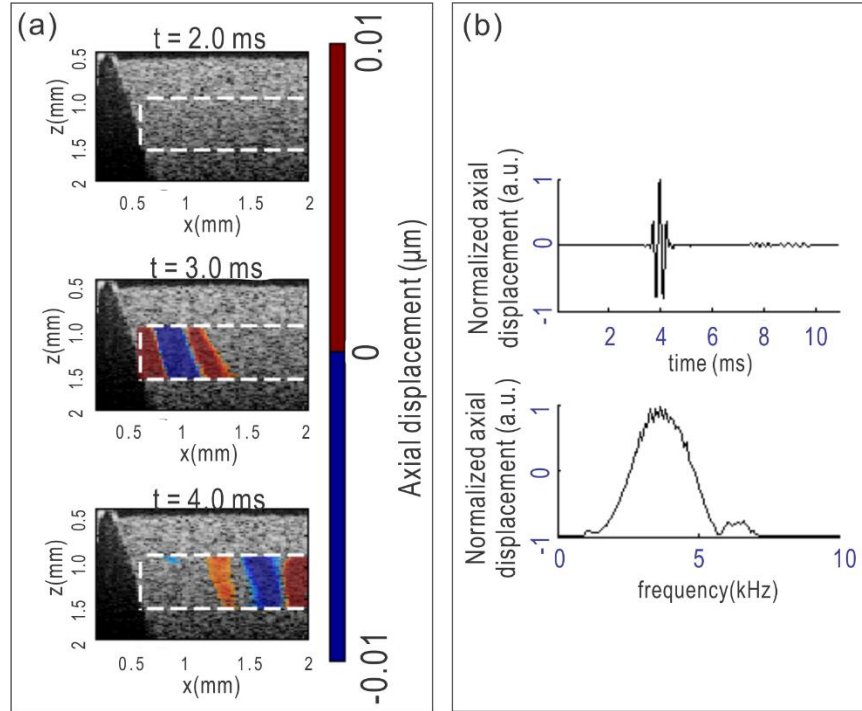


Figure 5-16 Displacement field in a 1%-agar phantom after compression

(a) Normalized axial displacements (colour scale) superimposed on the B-mode image (grey scale) at different instants. The white dash line delineates the region of interest where compression has been applied. (b) Axial displacements profile (upper) and spectrum (lower) at one location.

Based on the above results, the conclusions can be made that the digital pulse compression is effectively implemented in OCT-based shear wave elastography technique. A broadband ([1 - 5] kHz) frequency-modulated mechanical excitation was applied to phantoms through a piezoelectric actuator. The subsequent displacement field was detected and recorded using a PhS-OCT system. Inverse filtering was performed on the recorded displacements to obtain a spatial-temporal compression of the initial propagating chirp into a broadband propagating pulse. Pulse propagation is then used to either reconstruct maps of the local shear modulus or compute dispersion curves.

The pulse compression algorithm significantly improves the signal-to-noise ratio of detected displacements: a 12.8 dB increase has been obtained in a homogeneous agar phantom. PhS-OCT already has great sensitivity (nanometre scale) to detect axial

displacements compared to other imaging modalities such as ultrasound or MRI. Increasing the signal-to-noise ratio will still be valuable for *in vivo* applications and particularly for ocular tissues.

The compressed displacement field at a given depth can also be represented in the (t,x) domain as displayed in Figure 5-17(a). In the (t,x) domain, the local slope of the signal represents the local shear wave propagation speed. Local shear wave speed values are converted to local shear modulus values, leading to the shear modulus map shown in Figure 5-17(b). For this phantom, the median shear modulus was estimated to be 4.14 ± 0.63 kPa

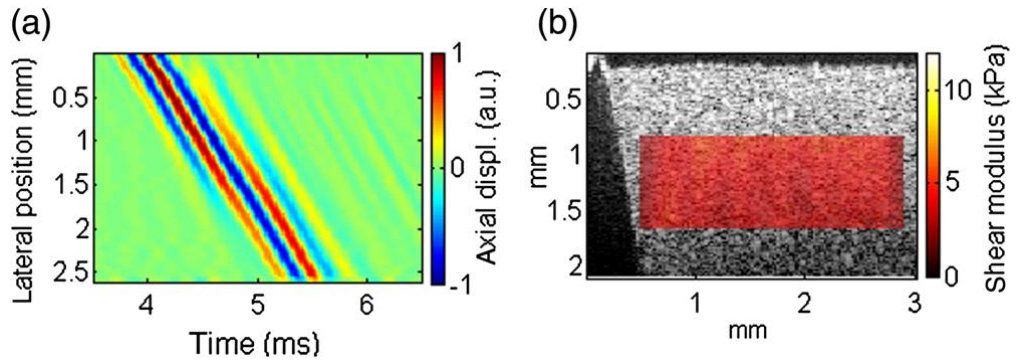


Figure 5-17 (a) Spatial-temporal representation of the normalized axial displacement field at a given depth of a 0.5%-agar phantom. The x -axis represents the time whereas the y -axis represents the lateral position. (b) Reconstructed shear modulus map (colour scale) superimposed on the B-mode image (grey scale).

The experiments are also performed on a heterogeneous phantom to investigate the advantages of pulse compression in a more complex medium. Figure 5-18 shows a B-mode image of the phantom, made from a 1%-agar background and a 2%-agar inclusion. This structural image exhibits very low contrast between the inclusion and the background.

Firstly, measurements using a 3-kHz single-frequency excitation were performed for comparison. Figure 5-19 depicts the displacement field detected at a given depth in the (t,x) domain. Distortions of the shear wavefronts can be observed on most cycles. They are due to interferences between the incident shear wave and reflections of the shear wave at the boundaries of the inclusion.

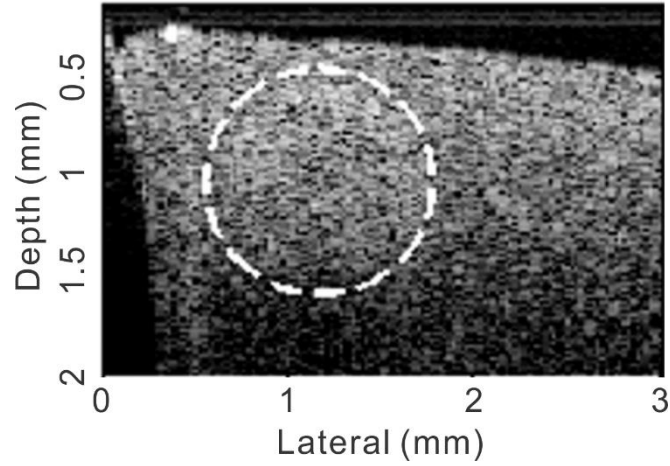


Figure 5-18 B-mode image of a heterogeneous phantom made from a 1%-agar background and 2%-agar inclusion. The white dash line delineates the inclusion.

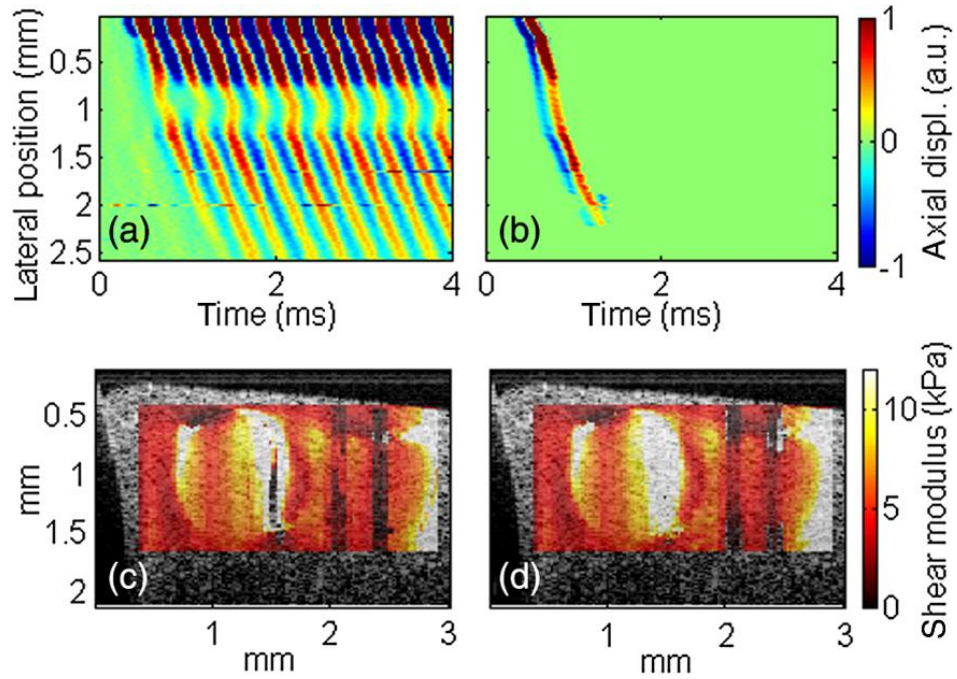


Figure 5-19 Results using a 3 kHz, 8-ms long, excitation on a 0.5%-agar phantom containing a 1%-agar inclusion.

(a and b) Spatio-temporal representation of the normalized axial displacement field without (a) and with (b) time-gating. (c and d) Shear modulus map (color scale) superimposed on the B-mode image (gray scale) reconstructed without (c) and with (d) time-gating.

Multi-wave superposition due to reflections can significantly affect the reconstruction, as shown in Figure 5-19(c): the corresponding shear modulus map exhibits strong

artefacts in the inclusion (unexpected soft region inside the inclusion and soft stripe near the right edge) as well as downstream of the inclusion (soft stripes on the right side of the region of interest). The median shear modulus of the expected inclusion region and the background estimated from this map are respectively 6.86 ± 4.26 kPa and 4.86 ± 1.53 kPa.

The effects of reflected shear waves can be reduced using a time-gating method. Time-gating selects only the earliest incident shear wavefront that is less likely to be affected by reflections occurring at later times (i.e., “near-ballistic propagation” Figure 5-19(b)). The corresponding shear modulus map is shown in Figure 5-19(d). Only minor artefacts have been suppressed, and the primary ones remain. This suggests that the first wavefront has too large of a period (0.33 ms) to avoid interfering with reflected waves. The median shear modulus of the expected inclusion region and the background estimated from this map are respectively 7.20 ± 5.11 kPa and 4.51 ± 1.30 kPa.

Figure 5-20 summarizes the results obtained on the heterogeneous phantom using the pulse compression method. Figure 5-20(a) shows displacements detected at a given depth resulting from chirp excitation. Note that only the first 6 ms of the 8-ms long signal are displayed here. Similar to the single-frequency excitation, interferences between the incident wave and reflected waves can be observed on the later cycles of the chirp. Figure 5-20(b) shows the displacement field after pulse compression. The initial chirp has been compressed to a main broadband pulse of about 0.21 ms width. Again, side lobes and distortion appear on the later cycles as a consequence of shear wave reflections at the boundaries of the inclusion. However, time-gating can be applied to isolate the earliest wavefront (Figure 5-20(c)). The corresponding shear modulus map is displayed in Figure 5-20(d) with the exact same color scale as that of Figure 5-19(c) and (d). Artefacts within the inclusion have been eliminated, allowing clear identification of the inclusion as a stiffer region than the background with high elastic contrast. The median shear modulus of the inclusion and the background are respectively 14.81 ± 5.12 kPa and 5.00 ± 0.79 kPa.

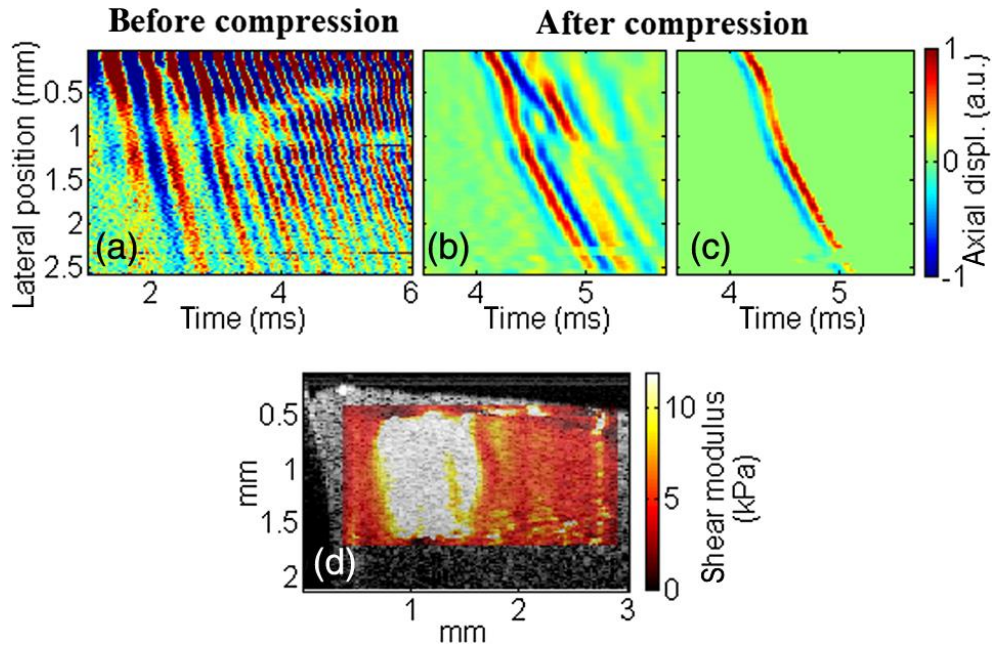


Figure 5-20 Heterogeneous phantom consisting of a 1%-agar background and a 2%-agar inclusion.

(a) Spatial-temporal representation of the raw normalized displacement field. (b) and (c) spatial-temporal representation of the displacement field after compression, without (b) and with (c) time-gating. (d) Shear modulus map reconstructed from the compressed, time-gated displacement field.

Pulse compression of ultrasonically induced shear wave

Acoustic radiation force induced SW-OCE adopts the benefit of remote wave generation in soft tissue, similar to several elastography techniques. Minimizing the ultrasound pressure is essential in ophthalmology for safety reasons. For this purpose, the pulse compression approach is proposed in ARF-SW-OCE. It utilizes coded ultrasound emissions to generate shear waves where the energy is spread over a long emission, and then numerically compressed into a short, localized, high-energy pulse.

The experiment arrangement is similar to that described in Chapter 5.3.2. The single element HIFU transducer is used to apply radiation force within the sample, but with a coded excitation waveform, as illustrated in Figure 5-21(a), the transducer was driven using a coded excitation in which a 7.5-MHz sine wave is modulated in amplitude by a binary “chirp”, i.e. a linear frequency-swept square wave (frequency range

[1 – 7] kHz, duration 3 ms, duty cycle 50%). Peak-to-peak voltages between 20 and 60 V_{pp} were applied, resulting in ultrasound peak pressures between 1 and 3 MPa. The results of the coded excitation were compared to those of a “conventional” 200- μ s pulse (central frequency 7.5 MHz) at equivalent peak pressures.

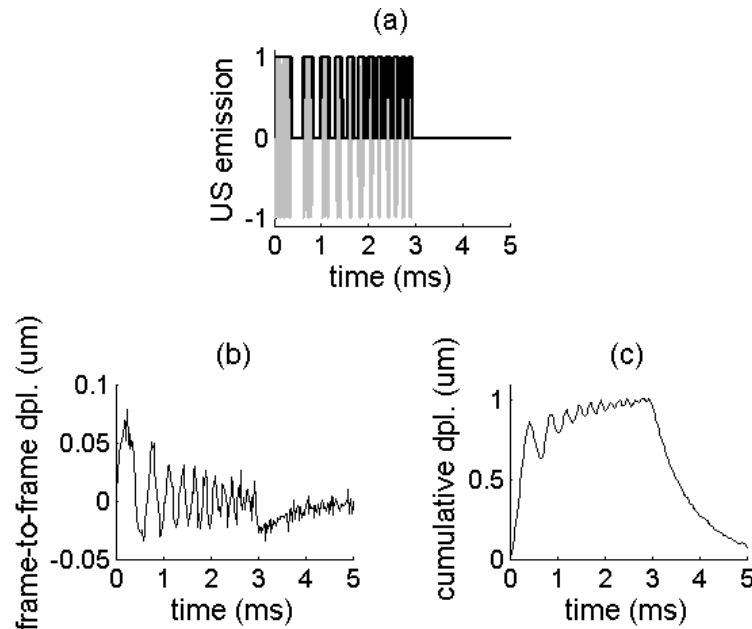


Figure 5-21 Axial displacements in a 10% gelatine phantom

- (a) Coded US emission consisting of a 7.5-MHz sine wave (grey line) modulated in amplitude by a linear frequency-swept square wave (black bold line, frequency from 1 to 7 kHz, duration 3 ms, duty cycle 50%, ultrasound peak pressure 3 MPa). (b) Frame-to-frame displacements sampled at 45 kHz. (c) Corresponding cumulative displacements.

The coded excitation driving the US transducer is shown in Figure 5-21(a). The resulting displacements detected in a 10%-gelatine phantom are a linear frequency-swept signal, as shown in Figure 5-21(b), with low frequencies (~ 1 kHz) occurring at early times and higher frequencies occurring at later times. For this example, the US peak pressure was 3 MPa ($MI = 1.10$). These displacements are frame-to-frame displacements, i.e. displacements occurring between two consecutive frames. Thus, they tend to represent the temporal derivative of the real displacement of the sample. The real displacement can be retrieved by integrating over time these frame-to-frame displacements. Because there is not enough dead time between each “on”-cycle of the

coded excitation for the sample to relax from the acoustic radiation force, the real displacement consists of a linear frequency-swept, low-amplitude oscillation superimposed on low-frequency, large amplitude motion (see Figure 5-21(c)).

Figure 5-22 shows snapshots of shear wave propagation resulting from the coded excitation in a 10%-gelatine phantom, before and after applying pulse compression. Raw displacements (Figure 5-22(a)) are a linear frequency-swept- wave. Figure 3b shows the displacements obtained after applying the pulse compression algorithm to raw displacements (as explained in the previous section). The post compression displacement consists of a short, spatially-localized pulse (main lobe occurring at $t \sim 2$ ms). The secondary lobes seen at later times ($t > 4$ ms) are imperfections of the pulse compression algorithm.

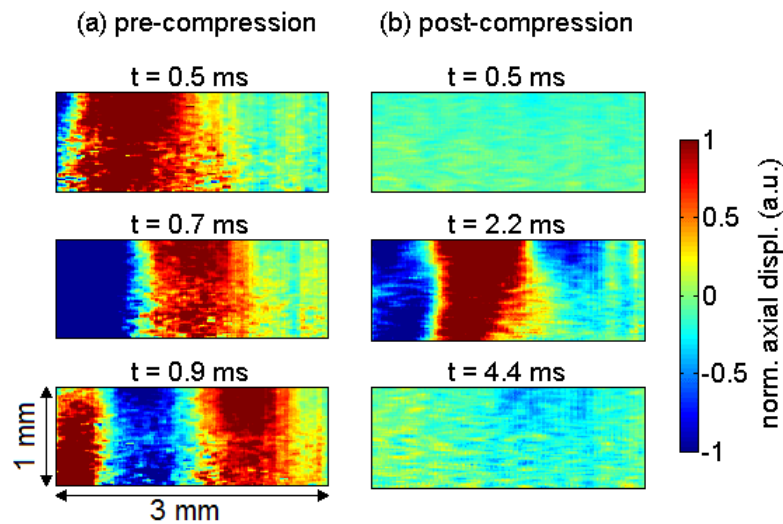


Figure 5-22 Snapshots of shear wave propagation induced in a 10%-gelatine phantom using a coded excitation at an US peak pressure of 3 MPa.

The shear source is located on the left edge of the imaging plane. The shear wave propagates from left to right. (a) Raw detected displacements. (b) Displacements obtained after pulse compression.

Figure 5-23 and Figure 5-24 compare the displacements resulting from different excitations at respectively 3 MPa and 1.5 MPa ($MI = 1.10$ and 0.55 , respectively). In these two figures, the temporal profile is displayed in the top row and the spectrum is displayed in the bottom row. The left column (Figure 4a and Figure 5a) is the result of

a 200- μ s pulse. The centre column (Figure 5-23b and Figure 5-24b) shows the raw displacements obtained from coded excitation before pulse compression. The right column (Figure 5-23c and Figure 5-24c) shows displacements obtained after applying pulse compression. For each case, the SNR was computed from the power spectrum. The displacements resulting from coded excitation have the same bandwidth as the US driving signal (1 to 7 kHz). The 200- μ s pulse generates a shear wave with a frequency range of [1 – 5] kHz and a SNR of 12.3 dB and 4.8 dB at US peak pressures of 3 MPa and 1.5 MPa respectively. A gain of ~ 30 dB is obtained using pulse compression, as seen in these figures.

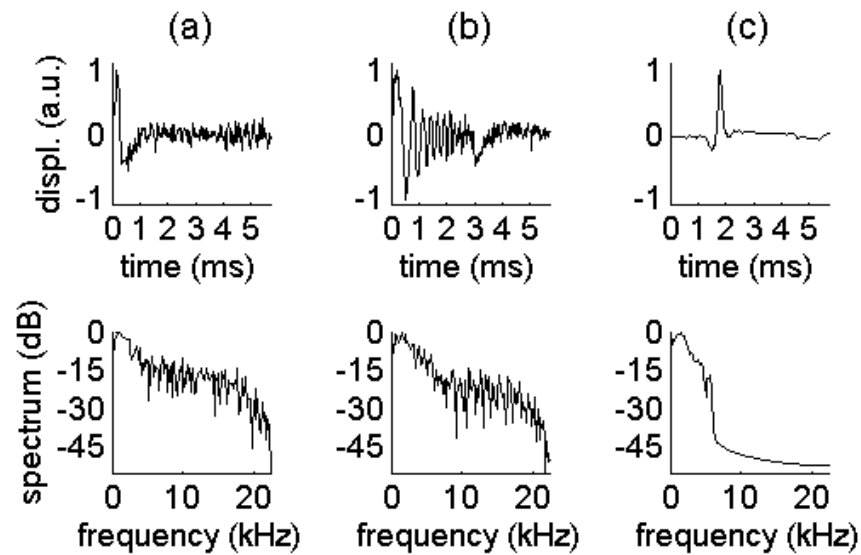


Figure 5-23 Temporal profile (top row) and spectrum (bottom row) of the displacements obtained in a gelatine phantom for an US peak pressure of 3 MPa (a) Conventional 200- μ s pulse, SNR = 12.3 dB. (b) Coded excitation before pulse compression, SNR = 16.3 dB. (c) Coded excitation after pulse compression, SNR = 43.0 dB.

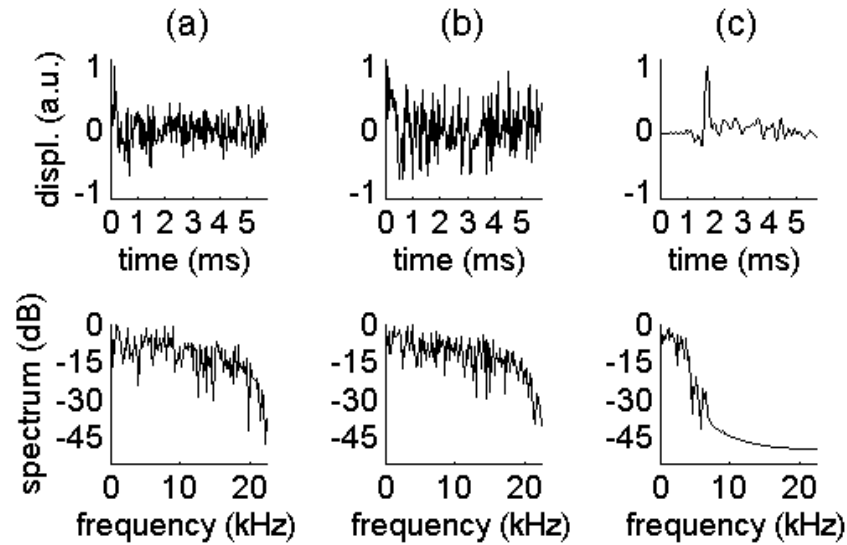


Figure 5-24 Temporal profile (top row) and spectrum (bottom row) of the displacements obtained in a gelatine phantom for an US peak pressure of 1.5 MPa

(a) Conventional 200- μ s pulse, SNR = 4.8 dB. (b) Coded excitation before pulse compression, SNR = 4.9 dB. (c) Coded excitation after pulse compression, SNR = 34.8 dB.

The performance of pulse compression in terms of the quality of the reconstructed shear wave velocity map is compared on a heterogeneous phantom. Phantom was made using two different gelatine concentrations: 5% gelatine for the left part, 10% for the right part. Both parts also contained different optical scatterer concentrations so that they could be identified on the B-mode from the intensity of the backscattered light (see Figure 5-25(a), 1.5% latex for the left part and 1% latex for the right part). Figure 5-25 (b) to (e) are stiffness maps: the shear wave speed is displayed in colour wherever the normalized correlation coefficient of the time-of-flight estimate is greater than 0.9. The dash line delineates the boundary between both parts of the phantom, as determined from the B-mode image and presented as a visual indicator (dashed line) on the stiffness maps. A mask based on OCT signal intensity and the shear wave time-of-flight correlation coefficient was applied to the wave speed maps, so that regions with low OCT signal or pixels with poor quality in time-of-flight estimate were shown as black.

At an US peak pressure of 3 MPa (MI = 1.10), both conventional pulse (Figure 5-25(b))

and coded excitation (Figure 5-25(c)) provide a sufficiently high-SNR shear wave to estimate the shear wave speed at every location of the imaging plane. However, the pulse compression approach (Figure 5-25(c)) better delineates both parts of the phantom: the demarcation between soft and stiff parts closely matches the dashed line. Indeed, greater SNR for the shear wave produces more accurate shear wave speed estimates.

At an US peak pressure of 1.5 MPa (MI = 0.55), the conventional pulse fails to reconstruct the shear wave speed at the bottom of the imaging plane whereas the pulse compression approach recovers the speed in the entire imaging area. Because of light attenuation, the deepest regions have the lowest sensitivity and are thus more likely to exhibit poor SNR. Furthermore, the 1.5-MPa conventional pulse yields artefacts at the left edge of the imaging plane (relatively high speed values are obtained in the soft part of the phantom). Such artefacts are reduced using the pulse compression approach.

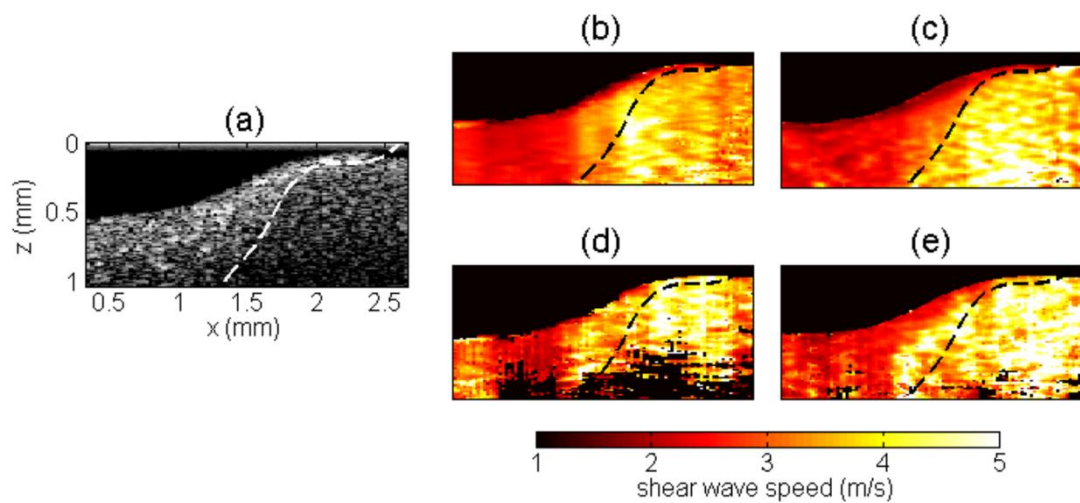


Figure 5-25 Reconstruction of stiffness maps in a heterogeneous phantom.

Shear wave source was located at the right edge of the imaging plane. (a) B-mode image of the phantom which is made of two parts of different gelatine concentrations (5%-gelatine for the left part, 10%-gelatine for the right part). The dash line delineates the boundary between the two parts. (b – e) Shear wave speed maps obtained using either a conventional 200-μs pulse (b and d) or a coded excitation (c and e), at US peak pressure of 3 MPa (b and c) or 1.5 MPa (d and e).

A more quantitative comparison is displayed in Figure 5-26, which shows a box plot

for each speed map shown in Figure 5-25 for both soft and stiff parts of the phantom. The dashed line corresponds to the expected mean values extracted from the literature: according to [155], a 5%- and 10%-gelatine phantom are expected to exhibit a shear wave speed of respectively 2 m/s and 4 m/s, respectively. At equivalent US peak pressures, the pulse compression approach provides median values that are closer to expected values. The values within the 25th and 75th percentiles are also more concentrated around the median values with the pulse compression approach. All experimental values are slightly higher than the expected value for the 5%-gelatine part. This might be caused by imperfections in phantom fabrication.

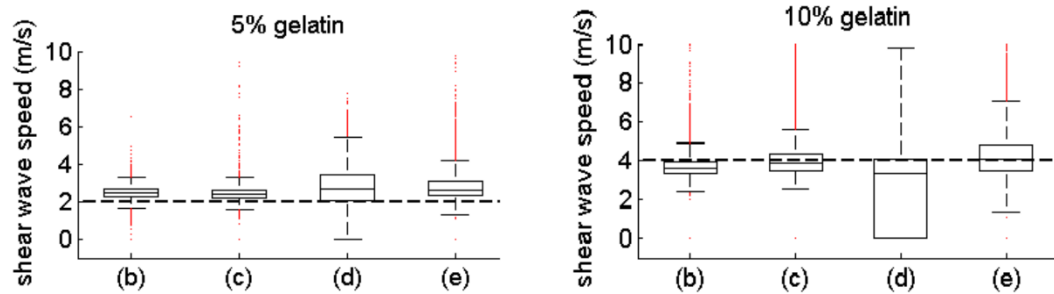


Figure 5-26 Box plot of the shear wave speed values in respectively the left part (left) and right part (right) of the phantom.

The central line in each box represents the median value, the box edges represent the 25th and 75th percentiles, the whiskers represent the extent of the data not considered as outliers, and the red dots represent outliers. The horizontal black dash line represent the expected values extracted from the literature [22]. The letters on the x-axis refer to the corresponding speed maps shown in Figure 6 and indicate different excitations: (b) 200- μ s pulse at 3 MPa, (c) coded excitation at 3 MPa, (d) 200- μ s pulse at 1.5 MPa, (e) coded excitation at 1.5 MPa.

Discussions

In this study, the digital pulse compression algorithm is implemented with OCT based shear wave elastography technique. The chirp shear wave propagation were detected and used to obtain spatial-temporal compression of the initial propagating chirp into a broadband propagating pulse.

The pulse compression technique has been demonstrated to significantly improve the signal-to-noise ratio of detected displacements: a 12.8 dB increase has been obtained in a homogeneous agar phantom. Increasing the signal-to-noise ratio will still be valuable for in vivo applications and particularly for ocular tissues. For instance, the cornea is both a stiff and fragile tissue that cannot undergo large displacements.

The reconstruction of shear modulus map in heterogeneous samples is simplified by the pulse compression. The incident shear wave can indeed be reflected by the boundaries of elastic heterogeneities. Pulse compression enables time-gating on a localized (spatial and temporal) signal to isolate the incident wave from reflected waves. For instance, in the heterogeneous phantom presented in this study, the shear modulus of the inclusion estimated from the non-localized excitation (Figure 5-20) strongly underestimated (7.20 kPa) and has a high spatial relative variance (71% of the shear modulus), whereas that estimated from the pulse compression approach (Figure 7) is much more accurate (14.81 kPa) and has a lower spatial relative variance (34% of the shear modulus). The shear modulus contrast between the inclusion and the background is much higher using the pulse compression method (50%) than using the single-frequency excitation (23%).

Pulse compression approach is also applicable to ARF-SW-OCE, providing an opportunity to reduce ARF power needed to launch shear waves detectable by the PhS-OCT technique. Using the pulse compression approach, an SNR gain of ~30 dB is obtained, compared to a conventional pulse at equivalent Mechanical Index (MI). At low MI, the enhanced SNR enables reconstruction of the speed map over a larger imaging area. This paves the way for shear wave elastography using acoustic radiation force with low MI. This is particularly important for ophthalmic applications, where the MI is limited to 0.23 (compared to 1.90 for most other organs). Greater SNR also provides better accuracy in the estimated shear wave speed.

Coded excitations can shape the spectral content of the shear wave. Being able to generate broadband shear waves with precise bandwidth control could help assess the potential dispersive behaviour of the shear wave. Dispersion can be induced by tissue viscosity or particular propagation modes. For the case of the cornea and other thin-

layered tissues, strong boundary conditions occur at the walls, forcing the shear wave into a guided propagation mode (Lamb-like waves) that affect its propagation speed as a function of frequency (i.e., dispersion). Several studies have investigated these effects [126, 128, 156] and could benefit from broad bandwidth shear waves.

5.3.4. Pulsed laser induced shear wave OCE

High energy nanosecond pulsed laser is an ideal source for generating shear waves for SW-OCE. The maximum frequency of pulsed laser induced shear waves in tissue-mimicking phantoms can go up to 25 kHz, which is too fast for other SWI modalities to be captured and tracked, but will provide highly localized propagation information. In comparison with ultrasound, pulsed laser is less demanding in contact conditions, without the need of coupling medium. As the energy source is laser, it is easy to control the focal region, i.e. the excitation location by focusing the pulsed laser into OCT imaging range. Preliminary experiments of detecting pulsed laser induced shear waves in tissue-mimicking phantoms are carried out to explore the feasibility to combine this photo-acoustic technique to shear wave OCE.

Wave generation with diode laser

As an initial trial, a diode laser source (iFLEX-2000-660-35-T, Qioptiq GmbH, Germany) is utilized, featuring 660 nm wavelength, 35 mW output power. To create the dynamic excitation, the output of this laser source is modulated by a 3 kHz square wave, which is generated by the analogue output card in the OCT system.

The optical path arrangements are illustrated in Figure 5-27. With a low numerical aperture lens, the excitation laser is focused onto the sample surface, a reflection mirror is used to avoid physical interference of excitation laser components and OCT components. To simulate a higher absorption of tissue, trace of Indian ink is added into the agar phantom. For this reason, the attenuation of OCT beam is also elevated, leaving limited OCT signal intensity on shallow surface.

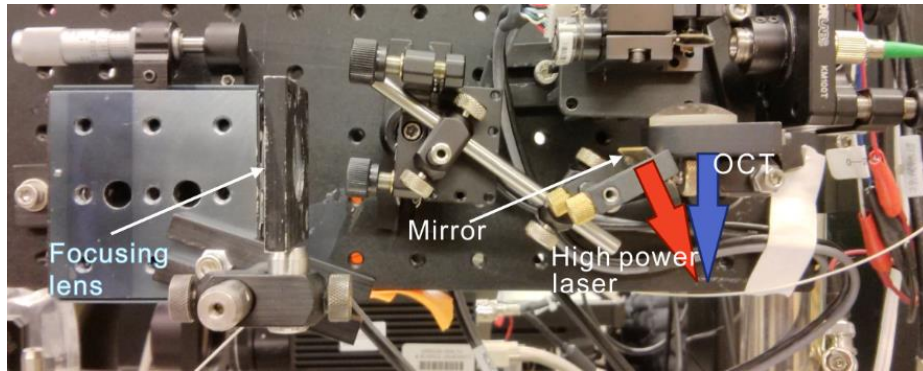


Figure 5-27 Optical path for confocal diode laser excitation

A result of shear wave imaging frames are displayed in Figure 5-28, indicating the propagation of one wavefront (generated by one pulse of the diode laser). As the laser energy is very low from the diode laser (up to $35\mu\text{J}$ per pulse), the wave is very weak. The SNR of the detected waves is not sufficient for elastogram reconstruction, but the propagation of surface wave mode is observable.

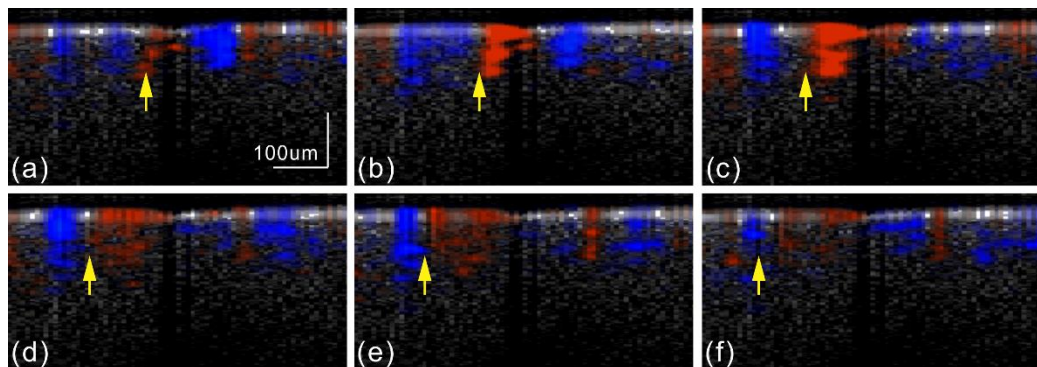


Figure 5-28 Shear wave imaging results with diode laser induced shear waves

An analysis of the wave propagation is carried out on the surface. A wave propagation path is selected near to the excitation laser focal point, and a spatial-temporal wave plot on this selected path is presented in Figure 5-29(a), showing four cycles of waves generated by the diode laser pulses. The slope of the wave plot pattern indicates the propagation velocity, as depicted in Figure 5-29(b), based on the 3 kHz waves, a linear fitting is performed on the phase delay of each wave trace, and the shear wave velocity is calculated from the slope and lateral locations of wave traces.

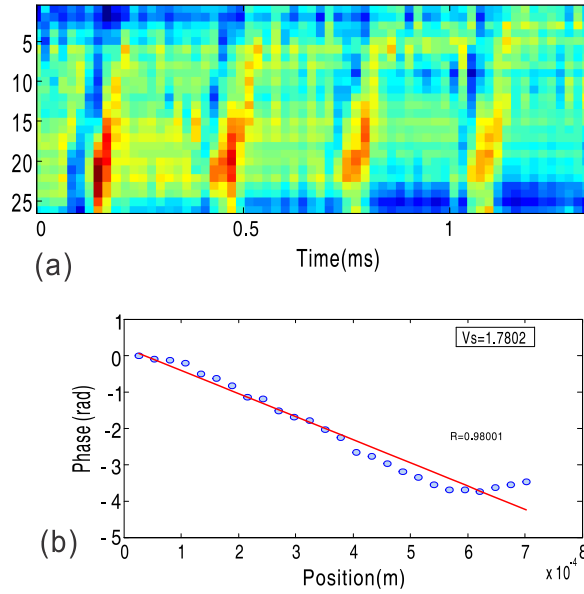


Figure 5-29 (a) spatial-temporal wave plot on selected wave path and (b) phase delay fitting for calculating wave velocity

The initial experiment using a relative low instantaneous power diode laser as a stimulation source is a feasibility test of laser induced SW-OCE. Benefiting from the high sensitivity of motion detection of PhS-OCT, even very low energy ($35\mu\text{J}$) can be detected in OCT shear wave imaging, thereafter provide the measurements of elastic modulus.

High energy pulsed laser

From the above experiment using a low-energy, pulse diode laser, the conclusion can be made that with a low absorption and low pulse energy, the mechanical wave energy is not enough for SW-OCE application, the wavelength and power needs to be considered to provide optimum shear wave amplitude.

A 532 nm Nd:YAG Q-switch laser (SureLight SL I-20, Continuum Lasers, CA, USA) is utilized as the high energy pulse laser source. In the preliminary study that aimed to demonstrate the feasibility of using pulsed lasers to induce the shear wave within the sample, we developed an epi-illumination setup where the pulsed laser and OCT sample beam were arranged in a confocal configuration (Figure 5-30). The synchronization signal was used to trigger the SWI and OCT system.

The repetition rate of the pulsed laser was 20 Hz with typical pulse duration of 5 nanoseconds. In order to minimize the thermal damage, the pulse energy is limited to less than 20 mJ. With the above configurations, a SWI M-B scan can be completed in 6.5 seconds. A tissue-mimicking phantom was manufactured to simulate the scattering and absorption of the pulsed laser in human skin.

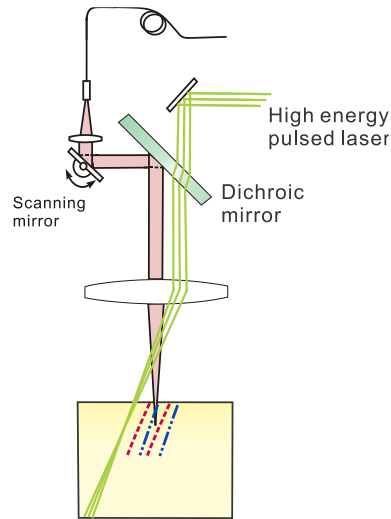


Figure 5-30 Epi-illumination setup for pulsed laser generation of shear waves

Results and discussions

Figure 5-31(a) is a pulsed laser induced shear wave pulse captured by SWI-OCT. The maximum frequency of the shear wave goes up to 25 kHz, and the SWI-OCT delivered a good imaging quality of high frequency shear waves, which can be used to map shear wave velocity. Although the high frequency shear waves attenuates too fast to reach the OCT imaging boundary, the pulse laser focal point can be re-positioned to cover full OCT range.

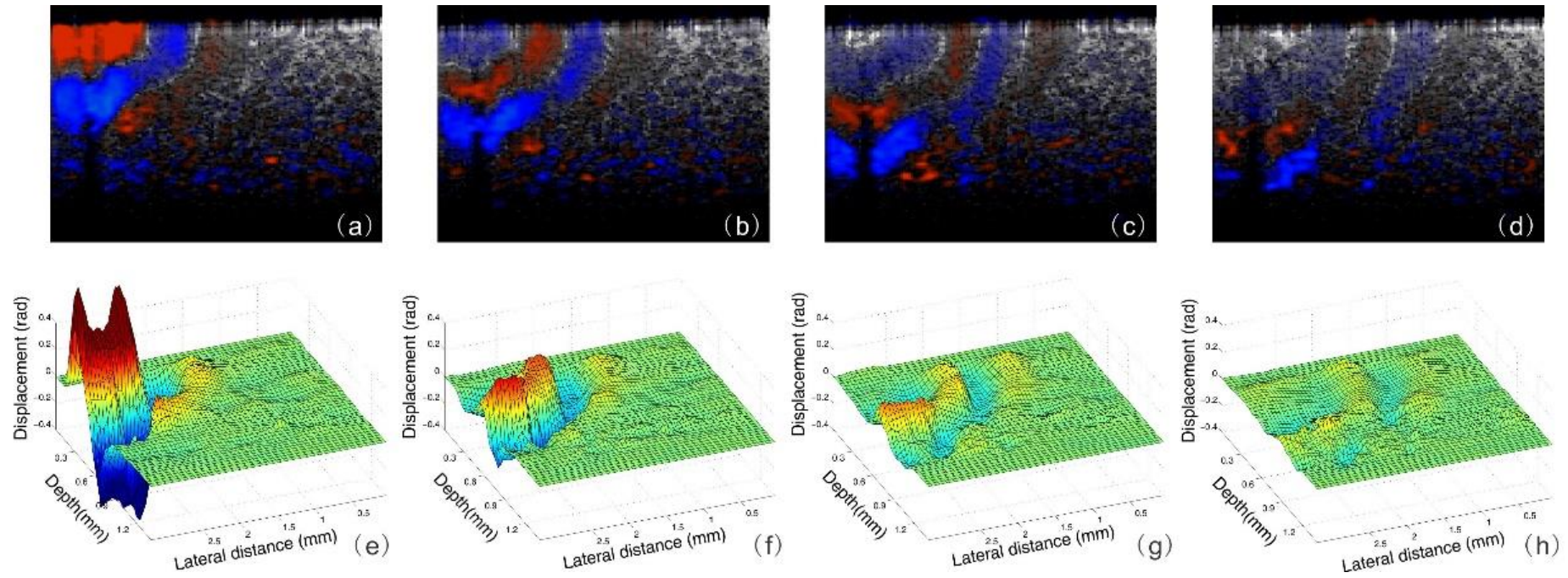


Figure 5-31 High energy pulsed laser induced shear waves captured by SWI-OCT in a skin-mimicking phantom.

(a-d) shear waves overlapped on phantom structural image at 4 adjacent SWI frames. (e-h) Shear wave propagation images after noise-suppression.

5.4. Elastography experiments on animal model

This section explores the potential of SW-OCE method in clinical applications such as dermatology and ophthalmology. We firstly apply the SW-OCE method to Thiel cadavers at different age and gender. This technique is then used on mouse cornea under *in vivo* situation. However, it is desirable that the elastography as a biomedical property of the tissue to be mapped, to provided direct visualisation of the tissue stiffness for ease of biomedical diagnosis.

5.4.1. OCE experiments on Thiel mouse skin

Experimental arrangements

To bring the SW-OCE technique a step closer to *in vivo* clinical applications, *in situ* experiments are carried out on Thiel-embalmed mouse cadavers[30], as well as fresh mouse cadaver skins. The experimental arrangements and procedures follows the technique aforementioned in Chapter 5.3.1, that 3 kHz shear waves were launched with a piezoelectric actuator as an external excitation. The shear wave velocity was estimated from the shear wave imaging results and used to recover regional shear modulus map.

The experiment specimen are 6 Thiel mice, embalmed time 12 months, age at embalming are 6 months, three for each gender. In the experiments, the mouse cadaver is placed on a petri dish, the shaker tip is gently attached to the skin surface on the back.

Results

Some typical shear wave imaging results on this skin site is given in [Figure 5-32](#). In (a-e), five frames of the displacement field are presented, where red and blue color

represents the motion towards and away from OCT imaging probe. The corresponding B-frame structural image is given in Figure 5-32(f), the dermis, subcutaneous fat layers are clearly displayed in this image. The propagation of mechanically induced shear waves can be observed in the SWI frames.

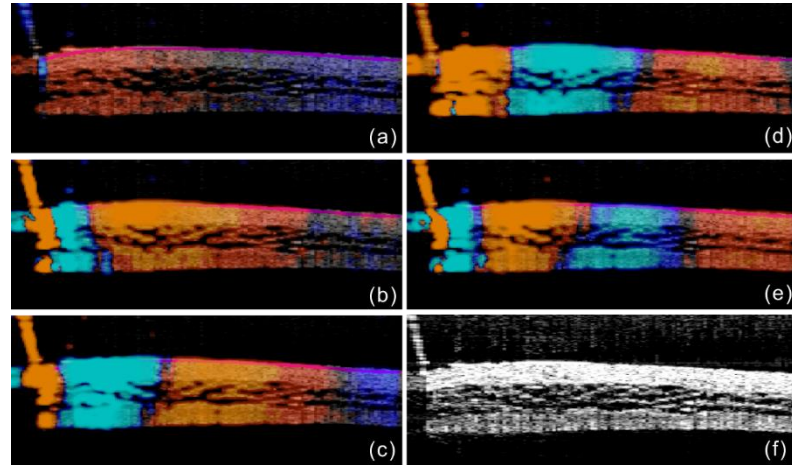


Figure 5-32 Typical shear wave imaging results on Thiel mouse cadaver

(a-e) displacement field snapshots at $t=6T_s$, $12T_s$, $18T_s$, $24T_s$ and $30T_s$, respectively. (Sampling period $T_s = 23.5 \mu s$) (f) Structural image

Using the time-of-flight method, the shear wave velocity map is calculated, and then shear modulus maps are reconstructed accordingly, as shown in Figure 5-33. To compensate the guiding effect of sample geometry, the shear wave imaging data were re-sampled and interpolated in a manually defined region following the skin geometry. These elastograms are only provided in dermis layer, since the substrate layers such as subcutaneous fat could not present enough intensity of OCT signal, thus the displacement estimation is unreliable.

The elastogram on the skin of three female mice are given in Figure 5-33(a1-a3). The shear modulus mean value of a central region of the elastogram ($0.16 \text{ mm} \times 1.5 \text{ mm}$) were calculated and displayed in Figure 5-34(F1-F3), together with standard deviation value. Figure 5-33(b1-b3) and Figure 5-34(M1-M3) are the results on male mice skin. No distinct heterogeneity is visualized on these skin elastograms, and the shear modulus values in the same gender implied no significant difference. Comparing different gender, the skin from male mice are indicating significantly higher values

than the female mice. The OCT images have also provided a distinguishable difference in skin structure: the dermis layer thickness in female mice are significantly smaller than male mice

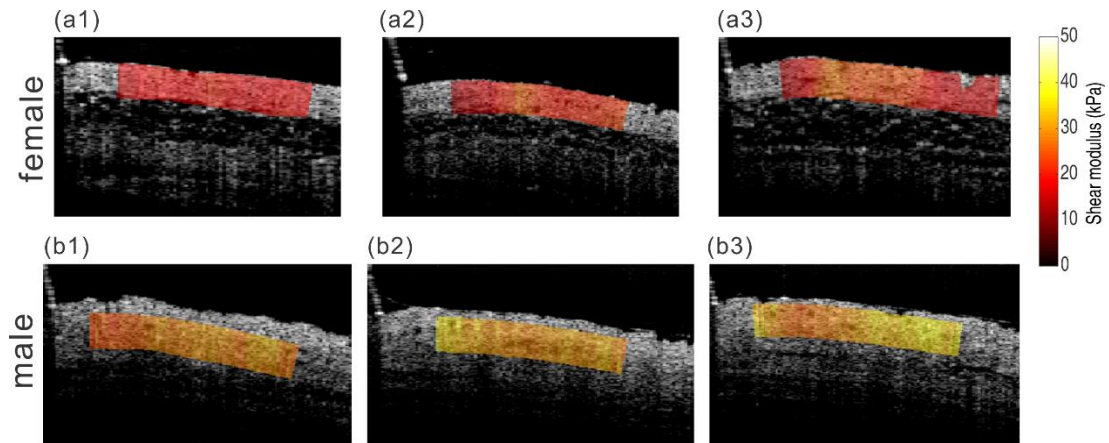


Figure 5-33 SW-OCE results on Thiel mouse skin, shear modulus map overlapped on structural image

(a1-a3) three female mouse skin shear modulus map (b1-b3) male mouse skin shear modulus map

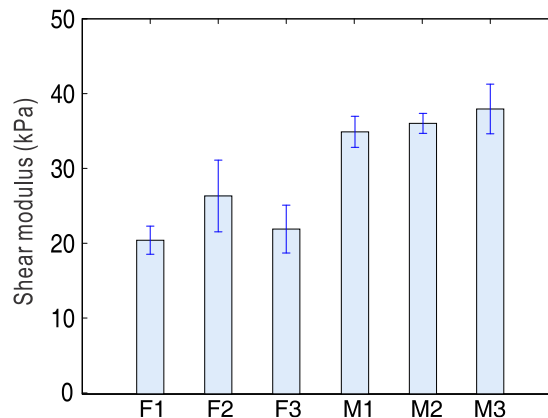


Figure 5-34 Averaged shear modulus results from 6 Thiel mouse cadaver, F1-F3 and M1-M3 are the female and male mouse, respectively

The same SW-OCE procedures are also carried out on the skin of fresh mice cadavers. Two mice with the same age as the Thiel embalmed mice are killed, and the SW-OCE measurements were carried out within half an hour of death. The OCE results of female and male mice skin are displayed in Figure 5-35(a) and Figure 5-35(b), respectively. Measurements are repeated on slightly different skin sites on the mouse back. The

averaged shear modulus and SD values of repeated measurements are given in Figure 5-36. All the measured shear modulus values are noticeably lower than the Thiel mice. Both gender shows averaged shear modulus values of <12 kPa, about 3 times lower than the Thiel embalmed mice skins. The trend of lower shear modulus in female skin than male skin remains the same, as depicted in Figure 5-36.

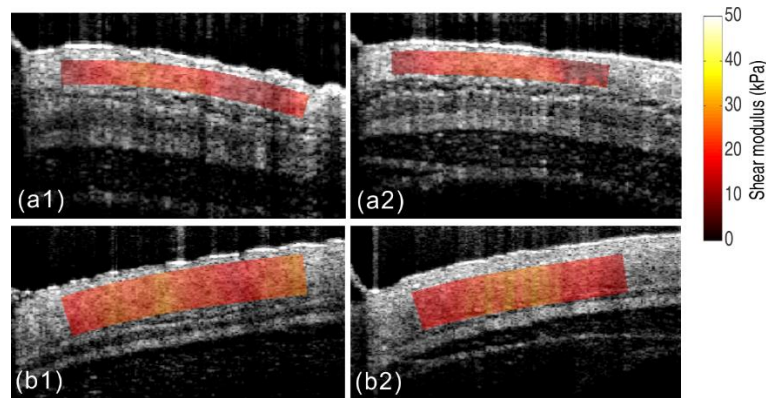


Figure 5-35 SW-OCE results on fresh mouse skin, shear modulus map overlapped on structural image. (a1, a2) female mouse (a3, a4) male mouse

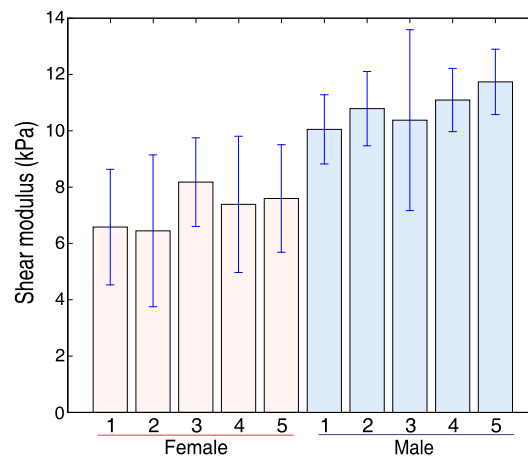


Figure 5-36 Averaged shear modulus from repeated measurements on fresh mouse cadaver

Discussions

In this study, mouse skin elastic property characterization were performed using SW-OCE. The shear wave propagation were analyzed and shear modulus mapping were obtained in a range of Thiel mouse cadaver skin. Results revealed significant

difference in shear modulus and structure in compliance with gender, and images on fresh mouse skin are also compared. Thiel embalming technique is also proved to present the ability to furthest preserve the mechanical property of biological tissue. The experiment results suggest that SW-OCE is an effective technique for quantitative estimation of skin tissue biomechanical status.

5.4.2. Shear wave OCE on cornea

Experimental setup

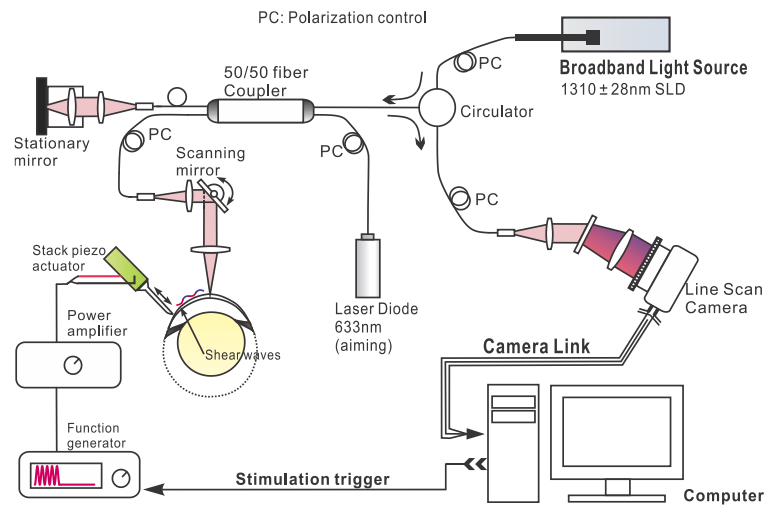


Figure 5-37 Experimental setup for shear wave OCE on mouse cornea

Figure 5-37 illustrates the experimental setup that combines OCT shear wave imaging and a mechanical actuator for wave generation. Shear waves are induced in the cornea using a piezoelectric actuator (AE0505, Thorlabs, New Jersey, USA) driven by a function generator (Tektronix, Oregon, USA) amplified by a power amplifier (AE Techon, Indiana, USA). Typical voltages of ~80 V peak-to-peak were applied to induce micron-scale displacements of the actuator. A polished stainless steel tip was glued to the piezoelectric actuator and placed in contact with the sample. The tip has a width of 1.7 mm and thus generate quasi-planar waves. Accurate positioning of the tip was performed using precision translation stages and monitored with real-time OCT B-mode images. The tip was placed so that it touches the sample without deforming it.

PhS-OCT system was operated in M-B scan mode, with M-scan size of 256 A-lines, recorded at a same location at line rate of 47 kHz. M-scans are repeated at lateral locations to cover a lateral imaging range of up to 7 mm (B-scan), synchronously with repeated mechanical stimulation for each M-scan. M-B scan contains 128 M-scans, and the acquisition time is within 1 second.

The experiments were carried on anesthetized mice. For single frequency excitation on in vivo mice cornea, six-cycle long, 5-kHz monochromatic mechanical tone bursts were applied. Two types of animals were investigated: wild type (C57BL/6) and BFSP-2 (CP49) knock-out homozygote mice. The knock-out mice lack a fibrillar protein leading to a softer intraocular lens and softer cornea[157, 158]. Mice were anesthetized with 2% isoflurane in 0.2L/min O₂ with 0.8L/min air flow. The cornea was exposed upward facing the OCT imaging beam. Saline solution was applied periodically and topically to maintain corneal hydration. All experiments were approved by a local ethics committee in University of Washington during the author's visiting study.

Broadband, frequency-modulated excitations were used in the investigation on donor human corneas. Human corneal buttons were obtained from an eye bank (SightLife, Seattle, WA, USA) and stored in Optisol solution (Chiron Ophthalmics, Irvine, CA, USA). Experiments were performed within 48h post-mortem. The corneal button was mounted on an artificial anterior chamber and placed upward facing the OCT beam. The intraocular pressure (IOP) was monitored using a digital manometer and varied (from 10 to 40 mmHg) by injecting saline solution into the artificial chamber. For this set of experiments, the piezoelectric actuator was driven with a 3-ms long, linear-swept-frequency signal (i.e. chirp) with frequencies ranging from 1 to 7 kHz. The digital pulse compression algorithm was introduced in Section 4.4.3.

Results

Figure 5-38 shows snapshots of a shear wave propagating in the cornea of an anesthetized mouse. Axial displacements with a 200-nm peak-to-peak magnitude are generated from the left of the imaging range and propagate transversally from left to

right.

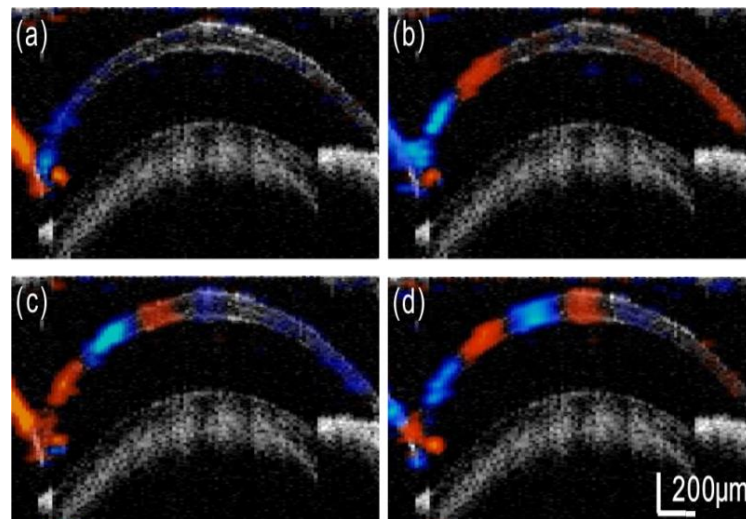


Figure 5-38 Snapshots of shear wave propagation in an in vivo mouse cornea sampled at different time points. Axial displacement amplitude is colour coded: red indicates the motion away from the OCT imaging probe.

Figure 5-39 shows a comparison between a group of knock-out mice (N=4) and wild-type mice (N=3). Figure 5-39(a) and (b) are examples of shear wave speed maps obtained on, respectively, a knock-out and a wild-type mouse. As expected, the cornea of the knock-out mouse appears softer than that of the wild-type mouse.

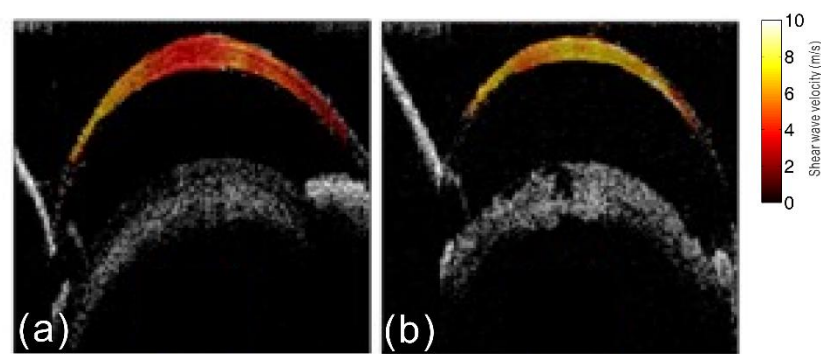


Figure 5-39 Shear wave speed map on mice cornea (a) knock-out mouse (b) wild-type, colour scale represents the shear wave speed and is superimposed on B-mode OCT image.

Figure 5-40 shows a significant difference in the shear wave speed (averaged over the entire cornea) between both groups: 3.92 ± 0.35 m/s and 5.04 ± 0.51 m/s for,

respectively, the knock-out and the wild-type mice (median value \pm inter-individual variance).

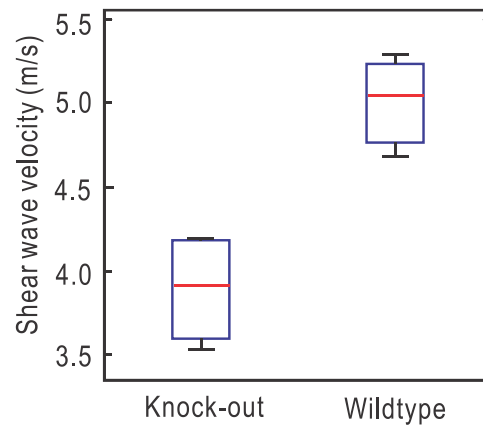


Figure 5-40 Quantitative comparison of the shear wave speed between a group of knock-out (N=4) and a group of wild-type (N=3) mice.

Previously in Section 5.3.3, the advantages of using shear wave pulse compression in tissue-mimicking phantoms have been demonstrated. It is proved that: 1) the SNR of the detected shear wave was significantly enhanced; and 2) the pulse compression reduced reconstruction artefacts by providing a better spatial-temporal resolution than single frequency excitations. Here, this approach is applied to excised human corneas.

Figure 5-41 illustrates the results obtained using pulse compression in an excised human cornea (31 years-old female donor) with IOP = 15 mmHg. The 3-ms long chirp signal is compressed into a short pulse lasting less than 500 μ s. In that example, the pulse compression yields a 7 dB gain in SNR.

Shear wave speed maps were reconstructed at different IOP levels using the pulse compression approach. Figure 5-42(a) shows shear wave speed maps of the central 3 mm of the cornea at three different IOP levels. Figure 5-42(b) shows a significant variation of the corneal shear wave speed (averaged over the entire imaging region) with the IOP.

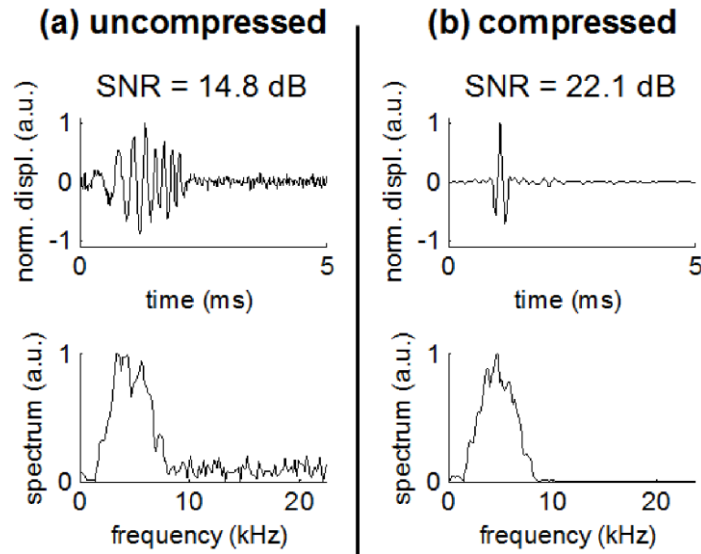


Figure 5-41 Results of frequency-modulated excitation on an excised human cornea (31 years old female donor). Temporal profile (top row) and spectrum (bottom row) of the displacements at one location respectively before (a) and after (b) pulse compression.

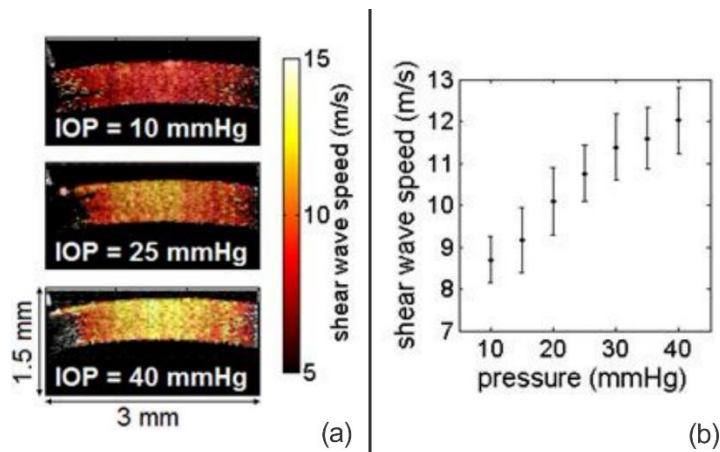


Figure 5-42 Effect of the IOP of the corneal shear wave speed assessed on an excised human cornea (31 years old female donor).

(a) Shear wave speed maps (colour scale) of the central part of the cornea at different intraocular pressure levels superimposed on the B-mode image (grayscale). (b) Shear wave speed averaged over the central part of the cornea as a function of the intraocular pressure.

Discussion and conclusions

Some preliminary study on the cornea of anesthetized mice is performed, demonstrating the ability of PhS-OCT to perform in vivo shear wave elastography.

Shear wave speed maps were reconstructed for two types of mice (knockout and wild-type) and showed a significant difference between both groups. In *in vivo* conditions, the IOP is not monitored. However, the low intra-group variability suggests that the inter-individual variance of the IOP is low between animals of the same group. Therefore, the shear wave speed difference observed between both groups is most likely directly related to corneal stiffness changes induced by the knock-out.

On an *ex vivo* human cornea, a set of experiments were performed using frequency-modulated rather than monochromatic excitations. Pulse compression consists in digitally compressing the frequency-modulated displacement field into a short, localized pulse while increasing the SNR. In addition, it was proved in the previous chapter on tissue-mimicking phantoms that retrieving a temporally-compressed pulse can help isolate the incident shear wave front from later occurring reflections, hence reducing reconstruction artefacts in heterogeneous media. Here, pulse compression technique is applied to the chirp excised human cornea and reconstructed shear wave speed maps at different IOP levels, showing significant corneal stiffening with the IOP increase.

In addition, the pulse compression approach provides broadband shear waves with single-shot excitations. Therefore, spectroscopic analysis could be performed to assess dispersion (frequency-dependence of the propagation speed) and attenuation[119]. It could provide valuable information, particularly for the cornea, where the thin-layer geometry can constrain shear wave propagation to guided modes that are highly dispersive[128]. In such propagation modes, the shear group velocity differs from that in a bulk medium and measuring the dispersion curve might be necessary to quantitatively retrieve the shear modulus.

5.5. Conclusions

In summary, the capability of SW-OCE for imaging the shear modulus is demonstrated. Shear wave OCE measurement were carried out with contact mechanically generated shear wave, acoustic radiation impulse shear wave, and laser pulse induced shear waves. The measured shear modulus values have reached good agreement with conventional compression test.

The pulse compression technique has been demonstrated to significantly improve the signal-to-noise ratio of detected displacements: a 12.8 dB increase has been obtained in a homogeneous agar phantom, and 7.3 dB in *in vivo* mouse cornea. Increasing the signal-to-noise ratio will be valuable for *in vivo* applications and particularly for ocular tissues.

OCE results are given for Thiel mouse skin and fresh *in situ* mouse skin, as well as *in vivo* mouse cornea. The ability for detecting dermis localized shear modulus has been demonstrated, significant difference in shear modulus have been observed between two genders, and between fresh skin and Thiel skin. In the cornea experiments, shear wave speed maps were reconstructed for two types of mice (knockout and wild-type) and showed a significant difference between both groups. On the *ex vivo* human cornea, a set of experiments were performed using frequency-modulated excitations, and reconstructed shear wave speed maps at different IOP levels, showing significant corneal stiffening with the IOP increase. It is hoped that this approach will lay the foundation for future *in vivo* studies of the mechanical properties of tissue microstructures, especially for clinical applications in ophthalmology (cornea and crystalline lens) and dermatology (epidermis and dermis).

6.CONCLUSIONS AND FUTURE WORK

The work presented in the above chapters is summarized in this chapter. Initially this project aimed to develop a novel elastography technique that combines transient shear waves and optical coherence tomography, for the fast and quantitative elasticity mapping of different tissue, which can aid medical diagnosis and treatment planning of skin disease and ophthalmic disorders. A review of the available literature shaped the investigation and helped identify the research directions for new researchers in this field.

Particular attention was paid to the development of OCT shear wave imaging technique, along with the optimization of SWI data. The investigations that followed therefore was focused on utilizing the shear wave dynamic propagation data for quantitative OCE image reconstruction. This chapter draws important conclusions about the relevance of the material presented and its influence on the possible direction of any further work.

6.1. Conclusions

This is the first report that uses OCT to directly visualise shear wave propagation with ultra-high frame rate and the first study to provide localised shear modulus maps from analysing shear wave propagation with a resolution comparable to OCT.

6.1.1. Transient mechanical waves in biological tissue

Nearly all elastography are based on the observation of tissue response to mechanical stimuli. Transient elastography, which mostly deals with shear wave, surface wave and Lamb wave, benefits from the quantitative nature, capable of providing lateral comparisons and is more convenient for setting up accurate and objective diagnosis. The usage of shear wave, surface wave and Lamb wave in biomedical area is still relatively new.

Bulk shear waves are considered the most promising wave mode to provide localised elastic property. Although within the imaging range of OCT, shear wave mode and surface wave mode are usually superposed, high frequency components of the detected waves are eligible to provide localised elasticity information, with subtle overestimation of shear modulus.

Driven by the lack of relevant research of high-frequency shear wave in soft tissue, finite element models are designed and simulations are performed to study the shear wave behaviour in biological tissue. Contact mechanical generation and pulsed laser induced transient waves are simulated, and the wave propagation behaviour are observed, demonstrating the ability of shear waves for showing localized shear modulus. Furthermore, the dispersion behaviour of laser induced surface wave is also studied. The conclusion can be made that even though the transient waves presents Rayleigh wave mode, the high frequency components can still be considered as shear waves, since the wavelength of high frequency waves is small, and their velocity is dominated by local mechanical property. SW-OCE method, as one transient

elastography method, has the potential to quantitatively measure the localized shear modulus.

6.1.2. Shear wave imaging technique

The PhS-OCT system is able to provide structural imaging of up to 9 μm axial resolution and 5.1 μm lateral resolution, and dynamic range of 100 dB. The proposed scanning protocol provides the motion detection of nanometre scale sensitivity and an ultra-high frame rate of up to 92 kfps. This provides a novel solution to capture the propagation of transient waves inside target OCT samples, with both high spatial resolution and high imaging frame rate, which is necessary for obtaining the elastography result with dynamic OCE.

2D-SRNCP algorithm is proved to be an effective phase-unwrapping method for SWI images, which helps to improve the SWI data quality, and enables the utilisation of large displacement amplitudes, which was further extends the applicability of OCT-SWI.

With the proposed OCT-SWI technique, a wave artefact is found to arise in the detection of mechanical waves with PhS-OCT. This motion artefact was then proved to be a combined product of sample surface motion and refractive index difference between sample and air, which cannot be neglected when imaging the displacement within tissue. With *a priori* sample refractive index, this artefact can be compensated. The proposed compensation method was tested in a series of experiments, and the effectiveness is validated.

A technique for improving the signal-to-noise ratio in SWI results using coded wave excitation is also proposed. The outcome of this chapter is a technique to obtain high quality SWI images for OCE construction.

6.1.3. SW-OCE towards clinical application

The first stage results presented in Section 5.3 covered a wide range of SW-OCE tests on tissue-mimicking phantoms, starting with contact mechanical stimulation, to the ultrasonically induced, ARFI SW-OCE. Experimental results and the expectations based on previous studies have demonstrated the quantitative imaging of shear modulus.

Investigations were conducted to develop pulse compression technique with contact shear wave stimulation and ARFI shear wave. Improvements to the signal-to-noise ratio of detected displacements are demonstrated: a 12.8 dB increase has been obtained in a homogeneous agar phantom, and 7.3 dB in *in vivo* mouse cornea. The SNR improvements will also be favorable for *in vivo* applications and particularly for ocular tissues.

SW-OCE technique is considered as a technique for examining Thiel mouse skin and fresh *in situ* mouse skin, as well as *in vivo* mouse cornea. The ability for detecting dermis localised shear modulus has been demonstrated, significant difference in shear modulus have been observed between two genders, and between fresh skin and Thiel skin. In the cornea experiments, shear wave speed maps were constructed for two types of mice (knockout and wild-type) and showed a significant difference between two gender groups. On the *ex vivo* human cornea, a set of experiments were performed using frequency-modulated excitations, and reconstructed shear wave speed maps at different IOP levels, showing significant corneal stiffening with IOP increase.

Currently, *in vivo* studies of the mechanical properties of tissue microstructures still remains a technological development stage and needs to be validated clinically. It is hoped that SW-OCE will benefit clinical practice in ophthalmology and dermatology with further development and trials.

6.2. Recommendations for future work

OCT shear wave imaging

This thesis will contribute to the academic world by bringing the ability of SWI with abundant imaging speed and resolution. However, it is still of great significance to elevate the imaging speed for the purpose of high resolution OCE. Since the resolution and accuracy of shear wave imaging is dependent on shear wave wavelength, elevated shear wave frequency is favourable for obtaining OCE results of higher resolution: in order to capture the shear waves with tens of microns wavelength in soft tissue, the SWI device need to be operated at hundreds of kfps or even at mega-frame per second. In here, several methods to elevate the SWI frame rate are presented:

- 1) Use parallel hardware for improving imaging speed. Parallel hardware is the most straight-forward method for improving OCT imaging speed[159]. This method will multiply the imaging speed, which will certainly lead to a very high cost.
- 2) Adopting the same scanning protocol of this study, but with faster A-scan rate, which achieves higher equivalent frame rate cost-effectively. Nevertheless, this technique still maintains drawbacks that require repeated, synchronized excitations of shear waves. As a consequence, attentions must be made to the disadvantages of long acquisition time and potentially exceeding the safety limit of mechanical/acoustical/optical energy load that induced into tissue.
- 3) Ultra-high speed SS-OCT[160] as well as high-speed resonant scanners has opened up the possibility of high-speed B-scan OCT-SWI. The state-of-art top speed SS-OCT with 20 million A-scan per second has been reported to achieve 14.6 kfps B-frame rate. It is foreseeable that ultra-high speed B-scan OCT-SWI will become feasible for SW-OCE purposes.

Shear modulus inversion

The model used here for image reconstruction assumed a constant propagation speed as a function of frequency with no propagation loss resulting from viscosity. Of course, both of these assumptions are not accurate for shear wave propagation in soft tissue over the kHz range. Both velocity dispersion and frequency dependent attenuation are significant. Future studies will explore frequency dependent propagation effects and

attempt to capture dispersion measurements as part of the shear wave imaging protocol.

Although elastic modulus maps in these well-controlled phantoms were well correlated with the physical characteristics of the gels used, there were systematic variations in reconstructed values due to limitations in the assumed wave propagation model. For example, an infinite medium is assumed in which there are no reflected waves[161]. By definition, elastic heterogeneities produce reflected waves which are not captured in the simple model. Also, diffraction from a finite source has not been modelled. Future studies will look at ways to capture these physical effects into a more sophisticated propagation model leading to more robust reconstructions in highly heterogeneous tissue. Biological tissues can exhibit such a complex, highly heterogeneous, structure. A first order approximation considers different tissue types as effective media with an effective shear modulus that reflects both the background and elastic heterogeneities smaller than the shear wavelength.

Tissue motion due to physiologic effects not correlated with induced displacements can limit the effectiveness of any dynamic elastography system. Many techniques have been proposed to minimize the influence of motion artefacts on dynamic displacement measurements, e.g. [162]. Given the high temporal sampling rate of the shear wave imaging system presented here, motion compensation algorithms should be possible. Future studies will also be directed toward robust algorithms minimizing the effects of potential motion artefacts on images of the shear wave velocity.

Shear wave generation

Finally, there are additional limitations on the method presented in this thesis to launch shear waves. Given the high sensitivity of the PhS-OCT detection system, shear wave generation using a non-destructive radiation source may be a feasible approach to a full variations of non-contact implementation. Focused UV radiation could serve as a photoacoustic source, which will extend the possibility of non-contact shear wave imaging elastography with our method.

Following the work introduced here, further experimental studies and clinical trials

may be necessary for final successful applications of these methods, and to improve this novel elastography diagnostic technique for widespread biomedical applications.

REFERENCES

1. Fung, Y.C., *Biomechanics: Mechanical Properties Of Living Tissues*. 2nd Ed. ed. 1993, New York, NY: Springer Verlag.
2. Wojcinski, S., et al., *Multicenter study of ultrasound real-time tissue elastography in 779 cases for the assessment of breast lesions: improved diagnostic performance by combining the BI-RADS®-US classification system with sonoelastography*. *Ultraschall in der Medizin* (Stuttgart, Germany: 1980), 2010. **31**(5): p. 484-491.
3. Kim, B.-S., et al., *Cyclic mechanical strain regulates the development of engineered smooth muscle tissue*. *Nature biotechnology*, 1999. **17**(10): p. 979-983.
4. Alberts, B., et al., *Essential cell biology*. 2013: Garland Science.
5. Bickers, D.R., et al., *The burden of skin diseases: 2004: A joint project of the American Academy of Dermatology Association and the Society for Investigative Dermatology*. *Journal of the American Academy of Dermatology*, 2006. **55**(3): p. 490-500.
6. Sanders, J.E., et al., *An explant model for the investigation of skin adaptation to mechanical stress*. *Biomedical Engineering, IEEE Transactions on*, 2002. **49**(12): p. 1626-1631.
7. Wang, Q. and V. Hayward, *In vivo biomechanics of the fingerpad skin under local tangential traction*. *Journal of biomechanics*, 2007. **40**(4): p. 851-860.
8. Diridollou, S., et al., *An In Vivo Method for Measuring the Mechanical*

- Properties of the Skin Using Ultrasound*. Ultrasound in medicine & biology, 1998. **24**(2): p. 215-224.
9. Diridollou, S., et al., *Sex-and site-dependent variations in the thickness and mechanical properties of human skin in vivo*. International journal of cosmetic science, 2000. **22**(6): p. 421-435.
 10. Diridollou, S., et al., *In vivo model of the mechanical properties of the human skin under suction*. Skin Research and technology, 2000. **6**(4): p. 214-221.
 11. Barel, A.O., W. Courage, and P. Clarys, *Suction chamber method for measurement of skin mechanics: the new digital version of the cutometer*. Handbook of Noninvasive Methods and the Skin, 2006: p. 583-591.
 12. Childers, M.A., et al., *Laser surgery of port wine stains using local vacuum pressure: changes in skin morphology and optical properties (Part I)*. Lasers in surgery and medicine, 2007. **39**(2): p. 108-117.
 13. Zhang, X., et al., *Quantitative assessment of scleroderma by surface wave technique*. Medical engineering & physics, 2011. **33**(1): p. 31-37.
 14. Gennisson, J.L., et al., *Assessment of elastic parameters of human skin using dynamic elastography*. Ultrasonics, Ferroelectrics and Frequency Control, IEEE Transactions on, 2004. **51**(8): p. 980-989.
 15. Liang, X. and S.A. Boppart, *Biomechanical Properties of In Vivo Human Skin From Dynamic Optical Coherence Elastography*. Ieee Transactions on Biomedical Engineering, 2010. **57**(4): p. 953-959.
 16. Kennedy, B.F., et al., *In vivo three-dimensional optical coherence elastography*. Optics Express, 2011. **19**(7): p. 6623-6634.
 17. McLaughlin, J. and D. Renzi, *Shear wave speed recovery in transient elastography and supersonic imaging using propagating fronts*. Inverse Problems, 2006. **22**(2): p. 681.
 18. Dupps Jr, W.J. and C. Roberts, *Effect of acute biomechanical changes on corneal curvature after photokeratectomy*. Journal of refractive surgery (Thorofare, NJ: 1995), 2000. **17**(6): p. 658-669.
 19. Roberts, C., *The cornea is not a piece of plastic*. Journal of Refractive Surgery, 2000. **16**(4): p. 407-413.
 20. Luce, D.A., *Determining in vivo biomechanical properties of the cornea with an ocular response analyzer*. Journal of Cataract & Refractive Surgery, 2005. **31**(1): p. 156-162.
 21. Juhasz, T., et al., *Corneal refractive surgery with femtosecond lasers*. Selected Topics in Quantum Electronics, IEEE Journal of, 1999. **5**(4): p. 902-910.

22. Dupps Jr, W.J. and S.E. Wilson, *Biomechanics and wound healing in the cornea*. Experimental eye research, 2006. **83**(4): p. 709-720.
23. Geraghty, B., et al., *Age-related variations in the biomechanical properties of human sclera*. Journal of the mechanical behavior of biomedical materials, 2012. **16**: p. 181-191.
24. Jones, I., M. Warner, and J. Stevens, *Mathematical modelling of the elastic properties of retina: a determination of Young's modulus*. Eye, 1992. **6**(6): p. 556-559.
25. Boyce, B., et al., *Stress-controlled viscoelastic tensile response of bovine cornea*. Journal of biomechanics, 2007. **40**(11): p. 2367-2376.
26. Elsheikh, A. and K. Anderson, *Comparative study of corneal strip extensometry and inflation tests*. Journal of the Royal Society Interface, 2005. **2**(3): p. 177-185.
27. Asejczyk-Widlicka, M. and B. Pierscionek, *The elasticity and rigidity of the outer coats of the eye*. British Journal of Ophthalmology, 2008. **92**(10): p. 1415-1418.
28. Hennighausen, H., et al., *Anterior-posterior strain variation in normally hydrated and swollen rabbit cornea*. Investigative ophthalmology & visual science, 1998. **39**(2): p. 253-262.
29. Pallikaris, I.G., et al., *Ocular rigidity in living human eyes*. Investigative ophthalmology & visual science, 2005. **46**(2): p. 409-414.
30. Wolff, K.D., et al., *Thiel embalming technique: a valuable method for microvascular exercise and teaching of flap raising*. Microsurgery, 2008. **28**(4): p. 273-278.
31. Thiel, W., *The preservation of the whole corpse with natural color*. Annals of anatomy Anatomischer Anzeiger: official organ of the Anatomische Gesellschaft, 1992. **174**(3): p. 185-195.
32. Normand, V., et al., *New insight into agarose gel mechanical properties*. Biomacromolecules, 2000. **1**(4): p. 730-738.
33. Hollman, K.W., et al., *Strain imaging of corneal tissue with an ultrasound elasticity microscope*. Cornea, 2002. **21**(1): p. 68-73.
34. Dupps Jr, W.J., et al., *Surface wave elastometry of the cornea in porcine and human donor eyes*. Journal of refractive surgery (Thorofare, NJ: 1995), 2007. **23**(1): p. 66.
35. Tanter, M., et al., *High-Resolution Quantitative Imaging of Cornea Elasticity Using Supersonic Shear Imaging*. Medical Imaging, IEEE Transactions on, 2009. **28**(12): p. 1881-1893.

36. Nguyen, T.-M., et al., *Monitoring of cornea elastic properties changes during UV-A/riboflavin-induced corneal collagen cross-linking using supersonic shear wave imaging: a pilot study*. Investigative ophthalmology & visual science, 2012. **53**(9): p. 5948-5954.
37. Garra, B.S., et al., *Elastography of breast lesions: initial clinical results*. Radiology, 1997. **202**(1): p. 79-86.
38. Zhi, H., et al., *Comparison of ultrasound elastography, mammography, and sonography in the diagnosis of solid breast lesions*. Journal of ultrasound in medicine, 2007. **26**(6): p. 807-815.
39. Scacchi, M., et al., *Elastosonographic evaluation of thyroid nodules in acromegaly*. European journal of endocrinology, 2009. **161**(4): p. 607-613.
40. Miyagawa, T., et al., *Real-time elastography for the diagnosis of prostate cancer: evaluation of elastographic moving images*. Japanese journal of clinical oncology, 2009. **39**(6): p. 394-398.
41. Venkatesh, S.K., et al., *Magnetic resonance elastography of liver tumors-preliminary results*. AJR. American journal of roentgenology, 2008. **190**(6): p. 1534.
42. Greenleaf, J.F., M. Fatemi, and M. Insana, *Selected methods for imaging elastic properties of biological tissues*. Annual review of biomedical engineering, 2003. **5**(1): p. 57-78.
43. Cespedes, I., et al., *Elastography: Elasticity Imaging Using Ultrasound with Application to Muscle and Breast In Vivo*. Ultrasonic imaging, 1993. **15**(2): p. 73-88.
44. Bercoff, J., et al., *In vivo breast tumor detection using transient elastography*. Ultrasound in medicine & biology, 2003. **29**(10): p. 1387-1396.
45. Trahey, G.E., et al., *Acoustic radiation force impulse imaging of the mechanical properties of arteries: In vivo and ex vivo results*. Ultrasound in medicine & biology, 2004. **30**(9): p. 1163-1171.
46. Wilson, L., D. Robinson, and M. Dadd, *Elastography-the movement begins*. Physics in medicine and biology, 2000. **45**(6): p. 1409.
47. Sinkus, R., et al., *Imaging anisotropic and viscous properties of breast tissue by magnetic resonance-elastography*. Magnetic resonance in medicine, 2005. **53**(2): p. 372-387.
48. Ophir, J., et al., *Elastography: imaging the elastic properties of soft tissues with ultrasound*. Journal of Medical Ultrasonics, 2002. **29**(4): p. 155-171.
49. Srinivasan, S., et al., *Analysis of an adaptive strain estimation technique in elastography*. Ultrasonic imaging, 2002. **24**(2): p. 109-118.

50. Ophir, J., et al., *Elastography: Ultrasonic estimation and imaging of the elastic properties of tissues*. Proceedings of the Institution of Mechanical Engineers, Part H: Journal of Engineering in Medicine, 1999. **213**(3): p. 203-233.
51. Nightingale, K.R., et al., *On the feasibility of remote palpation using acoustic radiation force*. The Journal of the Acoustical Society of America, 2001. **110**: p. 625.
52. Fahey, B., et al., *In vivo visualization of abdominal malignancies with acoustic radiation force elastography*. Physics in medicine and biology, 2008. **53**(1): p. 279.
53. Iyo, A.Y., *Acoustic radiation force impulse imaging: a literature review*. Journal of Diagnostic Medical Sonography, 2009.
54. Sarvazyan, A.P., et al., *Shear wave elasticity imaging: a new ultrasonic technology of medical diagnostics*. Ultrasound in medicine & biology, 1998. **24**(9): p. 1419-1435.
55. Palmeri, M.L., et al., *Acoustic radiation force impulse (ARFI) imaging of the gastrointestinal tract*. Ultrasonic imaging, 2005. **27**(2): p. 75-88.
56. Sharma, A.C., et al. *Acoustic radiation force impulse imaging of in vivo breast masses*. in *Ultrasonics Symposium, 2004 IEEE*. 2004. IEEE.
57. Hsu, S.J., et al. *In vivo acoustic radiation force impulse imaging of cardiac ablations*. in *Ultrasonics Symposium, 2005 IEEE*. 2005. IEEE.
58. Fahey, B., et al., *Liver ablation guidance with acoustic radiation force impulse imaging: challenges and opportunities*. Physics in medicine and biology, 2006. **51**(15): p. 3785.
59. Venkatesh, S.K., et al., *MR elastography of liver tumors: preliminary results*. AJR Am J Roentgenol, 2008. **190**(6): p. 1534-40.
60. Plewes, D., et al., *Visualizing tissue compliance with MR imaging*. Journal of Magnetic Resonance Imaging, 1995. **5**(6): p. 733-738.
61. Fowlkes, J., et al., *Magnetic-resonance imaging techniques for detection of elasticity variation*. Medical physics, 1995. **22**(11): p. 1771-1778.
62. Fercher, A., K. Mengedocht, and W. Werner, *Eye-length measurement by interferometry with partially coherent light*. Optics letters, 1988. **13**(3): p. 186-188.
63. Flournoy, P., R. McClure, and G. Wyntjes, *White-light interferometric thickness gauge*. Applied optics, 1972. **11**(9): p. 1907-1915.
64. Youngquist, R.C., S. Carr, and D.E. Davies, *Optical coherence-domain reflectometry: a new optical evaluation technique*. Optics Letters, 1987. **12**(3):

- p. 158-160.
65. Personick, S., *Photon Probe—An Optical-Fiber Time-Domain Reflectometer*. Bell System Technical Journal, 1977. **56**(3): p. 355-366.
 66. Huang, D., et al., *Optical coherence tomography*. Science, 1991. **254**(5035): p. 1178-1181.
 67. Schmitt, J., M. Yadlowsky, and R. Bonner, *Subsurface imaging of living skin with optical coherence microscopy*. Dermatology, 1995. **191**(2): p. 93-98.
 68. Tearney, G.J., et al., *Catheter-based optical imaging of a human coronary artery*. Circulation, 1996. **94**(11): p. 3013-3013.
 69. Tearney, G., et al., *Optical biopsy in human gastrointestinal tissue using optical coherence tomography*. The American journal of gastroenterology, 1997. **92**(10): p. 1800-1804.
 70. Tearney, G., et al., *Optical biopsy in human urologic tissue using optical coherence tomography*. The Journal of urology, 1997. **157**(5): p. 1915-1919.
 71. Boppart, S.A., M.E. Brezinski, and J.G. Fujimoto, *Optical coherence tomography imaging in developmental biology*, in *Developmental Biology Protocols*. 2000, Springer. p. 217-233.
 72. Drexler, W. and J.G. Fujimoto, *Optical coherence tomography: technology and applications*. 2008: Springer.
 73. Huber, R., M. Wojtkowski, and J. Fujimoto, *Fourier Domain Mode Locking (FDML): A new laser operating regime and applications for optical coherence tomography*. Optics Express, 2006. **14**(8): p. 3225-3237.
 74. Yun, S.-H., et al., *High-speed wavelength-swept semiconductor laser with a polygon-scanner-based wavelength filter*. Optics letters, 2003. **28**(20): p. 1981-1983.
 75. Huber, R., D.C. Adler, and J.G. Fujimoto, *Buffered Fourier domain mode locking: unidirectional swept laser sources for optical coherence tomography imaging at 370,000 lines/s*. Optics letters, 2006. **31**(20): p. 2975-2977.
 76. Ralston, T.S., et al., *Interferometric synthetic aperture microscopy*. Nature Physics, 2007. **3**(2): p. 129-134.
 77. Fercher, A.F., et al., *Optical coherence tomography-principles and applications*. Reports on progress in physics, 2003. **66**(2): p. 239.
 78. Kennedy, B.F., K.M. Kennedy, and D.D. Sampson, *A review of optical coherence elastography: fundamentals, techniques and prospects*. 2014.
 79. Chen, Z., et al., *Noninvasive imaging of in vivo blood flow velocity using*

- optical Doppler tomography*. Optics letters, 1997. **22**(14): p. 1119-1121.
80. Zhao, Y., et al., *Real-time phase-resolved functional optical coherence tomography by use of optical Hilbert transformation*. Optics Letters, 2002. **27**(2): p. 98-100.
 81. Zhao, Y., et al., *Doppler standard deviation imaging for clinical monitoring of in vivo human skin blood flow*. Optics Letters, 2000. **25**(18): p. 1358-1360.
 82. Schmitt, J.M., *OCT elastography: imaging microscopic deformation and strain of tissue*. Optics Express, 1998. **3**(6): p. 199-211.
 83. Kennedy, B.F., et al., *Strain estimation in phase-sensitive optical coherence elastography*. Biomedical optics express, 2012. **3**(8): p. 1865-1879.
 84. Wang, R.K., S. Kirkpatrick, and M. Hinds, *Phase-sensitive optical coherence elastography for mapping tissue microstrains in real time*. Applied Physics Letters, 2007. **90**(16): p. 164105.
 85. Chau, A.H., et al., *Mechanical analysis of atherosclerotic plaques based on optical coherence tomography*. Annals of biomedical engineering, 2004. **32**(11): p. 1494-1503.
 86. Chan, R., et al., *OCT-based arterial elastography: robust estimation exploiting tissue biomechanics*. Optics Express, 2004. **12**(19): p. 4558-4572.
 87. Hendriks, F., et al., *The relative contributions of different skin layers to the mechanical behavior of human skin in vivo using suction experiments*. Medical engineering & physics, 2006. **28**(3): p. 259-266.
 88. Ko, H.-J., et al., *Optical coherence elastography of engineered and developing tissue*. Tissue engineering, 2006. **12**(1): p. 63-73.
 89. Rogowska, J., et al., *Optical coherence tomographic elastography technique for measuring deformation and strain of atherosclerotic tissues*. Heart, 2004. **90**(5): p. 556-562.
 90. Wang, R.K., S. Kirkpatrick, and M. Hinds, *Phase-sensitive optical coherence elastography for mapping tissue microstrains in real time*. Applied Physics Letters, 2007. **90**(16): p. 164105-3.
 91. Kennedy, K.M., et al., *Analysis of mechanical contrast in optical coherence elastography*. Journal of biomedical optics, 2013. **18**(12): p. 121508-121508.
 92. Muthupillai, R., et al., *Magnetic Resonance Elastography by Direct Visualization of Propagating Acoustic Strain Waves*. Science, 1995. **269**(5232): p. 1854-1857.
 93. Van Houten, E., et al., *Elasticity reconstruction from experimental MR displacement data: initial experience with an overlapping subzone finite*

- element inversion process*. Medical Physics, 2000. **27**: p. 101.
94. Sandrin, L., et al., *Shear modulus imaging with 2-D transient elastography*. Ultrasonics, Ferroelectrics and Frequency Control, IEEE Transactions on, 2002. **49**(4): p. 426-435.
 95. Liang, X., Oldenburg, A. L., Crecea, V., et al., "Optical micro-scale mapping of dynamic biomechanical tissue properties" Optics Express 2008 **16**, p.11052-11065
 96. Adie, S.G., et al., *Audio frequency in vivo optical coherence elastography*. Physics in medicine and biology, 2009. **54**(10): p. 3129.
 97. Kennedy, B.F., et al., *In vivo dynamic optical coherence elastography using a ring actuator*. Optics Express, 2009. **17**(24): p. 21762-21772.
 98. Doyley, M., *Model-based elastography: a survey of approaches to the inverse elasticity problem*. Physics in medicine and biology, 2012. **57**(3): p. R35.
 99. Khalil, A.S., et al., *Tissue elasticity estimation with optical coherence elastography: toward mechanical characterization of in vivo soft tissue*. Annals of biomedical engineering, 2005. **33**(11): p. 1631-1639.
 100. Khalil, A.S., B.E. Bouma, and M.R.K. Mofrad, *A combined FEM/genetic algorithm for vascular soft tissue elasticity estimation*. Cardiovascular Engineering, 2006. **6**(3): p. 93-102.
 101. Sun, C., B. Standish, and V.X. Yang, *Optical coherence elastography: current status and future applications*. J Biomed Opt, 2011. **16**(4): p. 043001.
 102. Li, C., et al., *Determining elastic properties of skin by measuring surface waves from an impulse mechanical stimulus using phase-sensitive optical coherence tomography*. Journal of The Royal Society Interface, 2012. **9**(70): p. 831-841.
 103. Li, C., et al., *Evaluating elastic properties of heterogeneous soft tissue by surface acoustic waves detected by phase-sensitive optical coherence tomography*. Journal of Biomedical Optics, 2012. **17**(5): p. 0570021-05700210.
 104. Li, C., et al., *Quantitative elastography provided by surface acoustic waves measured by phase-sensitive optical coherence tomography*. Opt. Lett., 2012. **37**(4): p. 722-724.
 105. Li, C., et al., *Noncontact all-optical measurement of corneal elasticity*. Optics letters, 2012. **37**(10): p. 1625-1627.
 106. Wang, S., et al., *A focused air-pulse system for optical-coherence-tomography-based measurements of tissue elasticity*. Laser Physics Letters, 2013. **10**(7): p. 075605.
 107. Crecea, V., et al., *Magnetomotive nanoparticle transducers for optical*

- rheology of viscoelastic materials*. Optics express, 2009. **17**(25): p. 23114-23122.
108. Bloch, S. and A. Hales, *New techniques for the determination of surface wave phase velocities*. Bulletin of the Seismological Society of America, 1968. **58**(3): p. 1021-1034.
 109. Abbiss, C., *Shear wave measurements of the elasticity of the ground*. Geotechnique, 1981. **31**(1): p. 91-104.
 110. Su, Z., L. Ye, and Y. Lu, *Guided Lamb waves for identification of damage in composite structures: A review*. Journal of sound and vibration, 2006. **295**(3): p. 753-780.
 111. Ophir, J., et al., *Elastography: A quantitative method for imaging the elasticity of biological tissues*. Ultrasonic Imaging, 1991. **13**(2): p. 111-134.
 112. Wang, H.-C., et al., *Laser ultrasonic surface wave dispersion technique for non-destructive evaluation of human dental enamel*. Optics express, 2009. **17**(18): p. 15592-15607.
 113. Welch, A.J. and M.J. Van Gemert, *Overview of Optical and Thermal Laser-tissue Interaction and Nomenclature*. 2011: Springer.
 114. Lamb, H., *On waves in an elastic plate*. Proceedings of the Royal Society of London. Series A, 1917. **93**(648): p. 114-128.
 115. Krautkrämer, J. and H. Krautkrämer, *Ultrasonic testing of materials*. 1990.
 116. Achenbach, J.D., *Wave propagation in elastic solids*. 1975, Amsterdam: North Holland Pub.
 117. Bercoff, J., M. Tanter, and M. Fink, *Supersonic shear imaging: a new technique for soft tissue elasticity mapping*. Ultrasonics, Ferroelectrics and Frequency Control, IEEE Transactions on, 2004. **51**(4): p. 396-409.
 118. Virieux, J., *P-SV wave propagation in heterogeneous media: Velocity-stress finite-difference method*. Geophysics, 1986. **51**(4): p. 889-901.
 119. Deffieux, T., et al., *Shear wave spectroscopy for in vivo quantification of human soft tissues visco-elasticity*. IEEE transactions on medical imaging, 2009. **28**(3): p. 313.
 120. Nordez, A. and F. Hug, *Muscle shear elastic modulus measured using supersonic shear imaging is highly related to muscle activity level*. Journal of Applied Physiology, 2010. **108**(5): p. 1389-1394.
 121. Chen, S., et al., *Shearwave dispersion ultrasound vibrometry (SDUV) for measuring tissue elasticity and viscosity*. Ultrasonics, Ferroelectrics and Frequency Control, IEEE Transactions on, 2009. **56**(1): p. 55-62.

122. Neubrand, A. and P. Hess, *Laser generation and detection of surface acoustic waves: Elastic properties of surface layers*. Journal of applied physics, 1992. **71**(1): p. 227-238.
123. Schneider, D. and T. Schwarz, *A photoacoustic method for characterising thin films*. Surface and Coatings Technology, 1997. **91**(1): p. 136-146.
124. Zhang, X., et al., *Noninvasive ultrasound image guided surface wave method for measuring the wave speed and estimating the elasticity of lungs: A feasibility study*. Ultrasonics, 2011. **51**(3): p. 289-295.
125. Zhang, X., B. Qiang, and J. Greenleaf, *Comparison of the surface wave method and the indentation method for measuring the elasticity of gelatin phantoms of different concentrations*. Ultrasonics, 2011. **51**(2): p. 157-164.
126. Couade, M., et al., *Quantitative assessment of arterial wall biomechanical properties using shear wave imaging*. Ultrasound in medicine & biology, 2010. **36**(10): p. 1662-1676.
127. Royer, D. and E. Dieulesaint, *Elastic Waves in Solids II: Generation, Acousto-Optic Interaction, Applications*. Vol. 2. 2000: Springer Verlag.
128. Nguyen, T.-M., et al., *Assessment of viscous and elastic properties of sub-wavelength layered soft tissues using shear wave spectroscopy: theoretical framework and in vitro experimental validation*. Ultrasonics, Ferroelectrics and Frequency Control, IEEE Transactions on, 2011. **58**(11): p. 2305-2315.
129. Aid, K. and P. Richards, *Quantitative seismology: Theory and methods*. San Francisco, 1980.
130. Li, C., et al., *A comparison of laser ultrasound measurements and finite element simulations for evaluating the elastic properties of tissue mimicking phantoms*. Optics & Laser Technology, 2012. **44**(4): p. 866-871.
131. Saleh, B.E.A. and M.C. Teich, *Fundamentals of photonics*. 1991: Wiley.
132. Siegman, A.E., *Lasers University Science Books*. Mill Valley, CA, 1986. **37**.
133. Drexler, W., et al., *In vivo ultrahigh-resolution optical coherence tomography*. Optics letters, 1999. **24**(17): p. 1221-1223.
134. Drexler, W., et al., *Ultrahigh-resolution ophthalmic optical coherence tomography*. Nature medicine, 2001. **7**(4): p. 502-507.
135. Hitzenberger, C.K., et al., *Dispersion effects in partial coherence interferometry: implications for intraocular ranging*. Journal of Biomedical Optics, 1999. **4**(1): p. 144-151.
136. Golubovic, B., et al., *Optical frequency-domain reflectometry using rapid wavelength tuning of a Cr 4+: forsterite laser*. Optics Letters, 1997. **22**(22): p.

- 1704-1706.
137. Choma, M.A., et al., *Sensitivity advantage of swept source and Fourier domain optical coherence tomography*. Optics Express, 2003. **11**(18): p. 2183-2189.
 138. Zhao, Y., et al., *Real-time phase-resolved functional optical coherence tomography by use of optical Hilbert transformation*. Opt. Lett., 2002. **27**(2): p. 98-100.
 139. Itoh, K., *Analysis of the phase unwrapping algorithm*. Applied Optics, 1982. **21**(14): p. 2470-2470.
 140. Ghiglia, D.C. and M.D. Pritt, *Two-dimensional phase unwrapping: theory, algorithms, and software*. 1998: Wiley New York:.
 141. Pritt, M.D., *Phase unwrapping by means of multigrid techniques for interferometric SAR*. Geoscience and Remote Sensing, IEEE Transactions on, 1996. **34**(3): p. 728-738.
 142. Costantini, M., *A novel phase unwrapping method based on network programming*. Geoscience and Remote Sensing, IEEE Transactions on, 1998. **36**(3): p. 813-821.
 143. Zhang, S., X. Li, and S.-T. Yau, *Multilevel quality-guided phase unwrapping algorithm for real-time three-dimensional shape reconstruction*. Applied optics, 2007. **46**(1): p. 50-57.
 144. Herr áez, M.A., et al., *Fast two-dimensional phase-unwrapping algorithm based on sorting by reliability following a noncontinuous path*. Applied Optics, 2002. **41**(35): p. 7437-7444.
 145. Setchell, R.E., *Refractive index of sapphire at 532 nm under shock compression and release*. Journal of applied physics, 2002. **91**(5): p. 2833-2841.
 146. Royston, T., H. Mansy, and R. Sandler, *Excitation and propagation of surface waves on a viscoelastic half-space with application to medical diagnosis*. The Journal of the Acoustical Society of America, 1999. **106**: p. 3678.
 147. Zabolotskaya, E.A., Y.A. Ilinskii, and M.F. Hamilton, *Nonlinear surface waves in soft, weakly compressible elastic media*. The Journal of the Acoustical Society of America, 2007. **121**: p. 1873.
 148. Catheline, S., et al., *Diffraction field of a low frequency vibrator in soft tissues using transient elastography*. Ultrasonics, Ferroelectrics and Frequency Control, IEEE Transactions on, 1999. **46**(4): p. 1013-1019.
 149. Ortiz, S., et al., *Optical distortion correction in optical coherence tomography for quantitative ocular anterior segment by three-dimensional imaging*. Optics express, 2010. **18**(3): p. 2782-2796.

150. Cook, C.E., *Pulse compression-key to more efficient radar transmission*. Proceedings of the IRE, 1960. **48**(3): p. 310-316.
151. Kroszczynski, J.J., *Pulse compression by means of linear-period modulation*. Proceedings of the IEEE, 1969. **57**(7): p. 1260-1266.
152. O'Donnell, M., *Coded excitation system for improving the penetration of real-time phased-array imaging systems*. Ultrasonics, Ferroelectrics and Frequency Control, IEEE Transactions on, 1992. **39**(3): p. 341-351.
153. Manduca, A., et al., *Spatio-temporal directional filtering for improved inversion of MR elastography images*. Medical image analysis, 2003. **7**(4): p. 465-473.
154. Hamhaber, U., et al., *Comparison of quantitative shear wave MR-elastography with mechanical compression tests*. Magnetic Resonance in Medicine, 2003. **49**(1): p. 71-77.
155. Hall, T.J., et al., *Phantom materials for elastography*. Ultrasonics, Ferroelectrics and Frequency Control, IEEE Transactions on, 1997. **44**(6): p. 1355-1365.
156. Nenadic, I.Z., et al., *Phase velocities and attenuations of shear, Lamb, and Rayleigh waves in plate-like tissues submerged in a fluid (L)*. The Journal of the Acoustical Society of America, 2011. **130**(6): p. 3549-3552.
157. Merdes, A., F. Gounari, and S.D. Georgatos, *The 47-kD lens-specific protein phakinin is a tailless intermediate filament protein and an assembly partner of filensin*. The Journal of cell biology, 1993. **123**(6): p. 1507-1516.
158. Simirskii, V.N., et al., *Inbred FVB/N mice are mutant at the cp49/Bfsp2 locus and lack beaded filament proteins in the lens*. Investigative ophthalmology & visual science, 2006. **47**(11): p. 4931-4934.
159. An, L., et al., *High speed spectral domain optical coherence tomography for retinal imaging at 500,000 A-lines per second*. Biomedical optics express, 2011. **2**(10): p. 2770.
160. Wieser, W., et al., *Multi-megahertz OCT: High quality 3D imaging at 20 million A-scans and 4.5 GVoxels per second*. Optics express, 2010. **18**(14): p. 14685-14704.
161. Yamakoshi, Y., J. Sato, and T. Sato, *Ultrasonic imaging of internal vibration of soft tissue under forced vibration*. Ultrasonics, Ferroelectrics and Frequency Control, IEEE Transactions on, 1990. **37**(2): p. 45-53.
162. Fahey, B.J., S.J. Hsu, and G.E. Trahey, *A novel motion compensation algorithm for acoustic radiation force elastography*. Ultrasonics, Ferroelectrics and Frequency Control, IEEE Transactions on, 2008. **55**(5): p. 1095-1111.

